It Takes Two To Tango

Advancing Flow Field and Emission Rate Estimation from Space: Insights from the TANGO mission

Koen Reerink

Delft University of Technology

TU Delft

SRON
Netherlands Institute for Space Research

It Takes Two To Tango

Advancing Flow Field and Emission Rate Estimation from Space: Insights from the TANGO mission

by

Koen Reerink

to obtain the degree of Master of Science
at the Delft University of Technology,
to be defended publicly on Wednesday August 28, 2024 at 10:00 AM.

Student number:	5585201	
Project duration:	December 1, 2023 – August 28, 2024	
Thesis supervisors:	Dr. Abel-John Buchner,	TU Delft
	Dr. ir. Manu Goudar	SRON
	Dr. Tobias Borsdorff	SRON

Cover: TANGO-Carbon Orbit and Image Visualization by SRON (Modified)

Preface

This thesis, a journey that spanned nine months of research and learning, marks the culmination of my Master's degree in Mechanical Engineering. The focus of this work is on atmospheric flow and emission rate estimation methods—an area I initially approached with limited knowledge. However, through dedication and support, I believe I have grown from a novice to a more informed and capable person in these fields.

First and foremost, I would like to express my deepest gratitude to my TU Delft supervisor, John. Your guidance and advice have been invaluable throughout this process. Reflecting on our numerous thesis meetings, I recall how often I would enter with uncertainty about my results and methodology, only to leave with a renewed sense of direction and a clear path forward. Your scientific insight and critical thinking have profoundly influenced my development, and for that, I offer my sincere thanks.

I am also deeply thankful to SRON Netherlands Institute for Space Research, where I had the privilege to be part of a distinguished scientific community. I extend my heartfelt appreciation to my SRON supervisors, Manu and Tobias, for the opportunity to contribute to SRON's work. From the outset, you welcomed me with open arms, providing the support and resources I needed to overcome challenges, whether they were conceptual hurdles or coding issues. Our weekly meetings were a cornerstone of my growth as a researcher, offering constructive feedback that significantly shaped this thesis. I am truly grateful for the chance to work at SRON and for your unwavering guidance.

And last but not least, I wanted to thank all my fellow interns and colleagues at SRON for the great laughs and scientific discussions we had. They will be missed. I wish you all the best in the future of your careers and may our paths cross again.

Finally, I would like to extend my deepest appreciation to my family and loved ones, whose unwavering support and encouragement have made this journey possible.

Koen Reerink
Delft, August 2024

Abstract

The TANGO mission represents a significant leap forward in the global monitoring of greenhouse gas emission plumes, particularly CO2 and NO2. Comprising two satellites, TANGO-Carbon and TANGO-Nitro, the mission is designed to operate from 2027 to 2031, offering unprecedented capabilities through stereo (temporally separated) and high spatial resolution emission plume images. These capabilities create a unique framework that facilitates the development of novel estimation methods for emission rates of greenhouse gas emitters. Conventional methods for estimating emission rates of CO2 and NO2 rely on combining gas concentration measurements with wind velocity fields derived from meteorological data, often introducing substantial uncertainties due to the inherent inaccuracies in wind velocity estimation. To address this challenge, this research explores alternative methods enabled by TANGO's innovative framework, which allows for the direct measurement of emission plume velocity from concentration data. By eliminating the dependency on uncertain meteorological inputs, these methods promise to reduce the uncertainty in emission rate estimates.

Through detailed simulations and analyses, this research demonstrates that the TANGO mission can effectively establish a framework for directly measuring emission plume velocities. By simulating the data products of the TANGO satellites using Large-Eddy Simulations and applying advanced methods such as traditional Correlation Image Velocimetry (CIV) and Computer Vision Correlation Image Velocimetry (CVision-CIV), wind velocity fields were successfully estimated from plume imagery. These estimates were found to be of promising precision across a range of conditions, including varying wind velocities, emission rates of greenhouse gasses, and levels of measurement noise in the simulations. Results revealed that the CVision-CIV method outperforms the traditional CIV method, especially in scenarios with low signal-to-noise ratios. Wind velocity fields directly estimated from plume imagery were implemented in the Cross-sectional Flux Method to estimate CO2 emission rates. The emission rate estimates indicate that direct plume velocity measurements provide a more accurate estimate of emission source rates than conventional methods, which rely on indirect wind velocity estimates from meteorological data. The use of wind velocity fields obtained through the CVision-CIV method resulted in CO2 emission rate estimates with ±20% accuracy in most scenarios, particularly under optimal SNR conditions. Additionally, the study highlights the impact of mission parameters such as image resolution and measurement noise on the accuracy of wind velocity estimations. It was found that higher image resolution and longer time intervals between measurements enhance the precision of wind velocity field estimates by reducing the relative effects of measurement noise.

In summary, this research demonstrates that direct estimation of wind velocities from emission plume imagery, as enabled by the TANGO mission's advanced capabilities, can accurately be performed and significantly enhance the accuracy of emission rate estimates. The improved wind velocity estimation methods proposed in this thesis offer a promising advancement in remote sensing techniques for greenhouse gas monitoring.

Contents

Preface i

Summary ii

Nomenclature ix

1 Introduction 1
- 1.1 The Mission: Monitoring and Reducing Greenhouse Gas Emissions 1
  - 1.1.1 Anthropogenic Emissions 1
  - 1.1.2 Estimating Emission rates 1
  - 1.1.3 Twin Anthropogenic Greenhouse Gas Observers 2
  - 1.1.4 Problem Statement 3
- 1.2 Emission Rate Estimation Methods 3
  - 1.2.1 Inversion Methods 4
  - 1.2.2 Mass Balance Methods 5
  - 1.2.3 Computer Vision Methods 5
- 1.3 Combination of CO2 and NO2 Emissions 6
- 1.4 Wind Velocity 7
  - 1.4.1 Correlation Image Velocimetry 8
  - 1.4.2 Computer Vision CIV 11
- 1.5 Summary and Discussion 12

2 Research Outline 14
- 2.1 Research Question 1: *How can the TANGO mission facilitate a framework for directly measuring the velocity of emission plumes from concentrations of CO2 and NO2?* . . 14
- 2.2 Research Question 2: *Can the direct measurement of the velocity of emissions plumes contribute to a more accurate estimation of emission source rates?* 15
- 2.3 Research Question 3: *How can the mission or measurement parameters be optimized to enhance the accuracy of the estimation of emission source rates?* 15

3 Methods and Results 17
- 3.1 Plume Simulation 17
- 3.2 Correlation Image Velocimetry 21
  - 3.2.1 The CIV Algorithm 21
  - 3.2.2 Wind Velocity Estimation Results 26
- 3.3 CVision-CIV 33
  - 3.3.1 UnLiteFLowNet-PIV and Extension 34
  - 3.3.2 Wind Velocity Estimation Results 36
- 3.4 Estimating CO2 Emission Rate 42
  - 3.4.1 Cross-sectional Flux Method 43
  - 3.4.2 Emission Estimation Results 45

4 Conclusion and Discussion 50
- 4.1 Wind Field Estimation 50
- 4.2 Emission Rate Estimation 52
- 4.3 Mission and Measurement Optimization 54

References 56

A MircoHH Initial Specifications 63

B NOX:NO2 Conversion 66

C CIV Algorithm Performance Tables 67
- C.1 Scenario: Variable Δt 67
- C.2 Scenario: Constant Δt 68

D CVision-CIV Performance Tables 69
- D.1 Scenario: Variable Δt 69
- D.2 Scenario: Constant Δt 70

E SNR Quantification 71

List of Figures

1.1 Depiction of the Twin Anthropogenic Greenhouse Gas Observers mission. The image displays the two CubeSats called TANGO-Carbon and TANGO-Nitro in the same orbit spaced by Δt. Source: SRON (2023) 3

3.1 Simulated CO2 and NO2-converted-to-CO2 emissions plumes with a wind velocity of 6 m/s, emission rate of 25 MT/y and l_1 measurement noise. 19
3.2 Flowchart representing the process that converts CO2 plume imagery into NO2 plume imagery which is used to create NO2-converted-to-CO2 plume imagery. 20
3.3 Data structure of DB_{TANGO}, comprised of CO2 and NO2-converted-to-CO2 plumes and wind velocity fields for a variety of wind velocities, emission rates, measurement noise levels and Δt's. 20
3.4 CO2 and NO2-converted-to-CO2 plume imagery (left column) from which two IW are extracted, indicated by the red squares. These IW are displayed in the right column. The CO2 and NO2-converted-to-CO2 plumes have a Δt of 100 s, 25MT/y emission rate and are noiseless. 22
3.5 The CCM of the IW displayed in Figure 3.4. The red dot indicates the location of the peak of the CCM. The magenta dot indicates the center of the CCM. The white vector from the center to the peak indicated the estimated displacement vector. 23
3.6 Plot (a) displays a sample CCM selected for one of the 50 arbitrary pixel locations from the image pair in Figure 3.4 for which the CCM was computed. The colored rectangles indicate the different peak neighborhoods used in the peak fitting procedure. Plot (b) displays the peak location estimated by the Gaussian fitting procedure for different peak neighborhood sizes. 24
3.7 Plot (a) illustrates the expected qualitative effects of SNR (orange line) and displacement gradients (blue line) on the quality of peak fitting (SSR) as the IWS increases. The green line represents the combined expected qualitative impact of SNR and displacement gradients on peak fitting quality. Plot (b) shows the observed trend (which holds for all pixel locations) in peak fitting quality (SSR) as the IWS increases for an arbitrarily selected pixel location from the image pair shown in Figure 3.4. 24
3.8 Imagery of two simulated CO2 plumes for an emission rate of 10 (plot (a)) and 25 MT/y (plot (d)) are displayed. Plots (b) and (e) display the results on percentile thresholding and plots (c) and (f) display the effects of constant thresholding, where for plots (b),(c),(e), and (f), pixel locations not in l_p have value 0 (blue color), while pixel locations in l_p are have value 1 (yellow color). 26
3.9 The first CO2 plume image in the image pair is displayed in plot (a). The resulting wind velocity field estimated by the CIV Algorithm is displayed in plot (b). For reference, the true wind velocity field filtered for pixel locations in l_p and the difference between the estimated and true wind velocity fields are displayed in plots (c) and (d) respectively. The plume characteristics included a true wind velocity of 6 m/s, an emission rate of 25 MT/y, a l_0 measurement noise level and a Δt of 50 seconds. 27
3.10 Accuracy plot of the wind velocity field estimated by the CIV Algorithm displayed in Figure 3.9. For perfect estimation, all points in the scatter plot lie on the red diagonal line. The scatter plot is color-coded with the horizontal distance from the emission source. 27
3.11 Plot (a) and (d) display the average RMSE and ME, respectively, for a Δt of 100 s, a wind velocity of 3 m/s and varying emission rates (ER) and measurement noise levels. Plot (b) and (e) display the average RMSE and ME for a Δt of 50 s, a wind velocity of 6 m/s and varying emission rates (ER) and measurement noise levels. Plot (c) and (f) display the average RMSE and ME for a Δt of 30 s, a wind velocity of 10 m/s and varying emission rates (ER) and measurement noise levels. All plots are complemented by a single standard deviation error-bar of the average RMSE and ME values. 30

3.12 Plot (a) and (d) display the average RMSE and ME, respectively, for a Δt of 20 s, a wind velocity of 3 m/s and varying emission rates (ER) and measurement noise levels. Plot (b) and (e) display the average RMSE and ME for a Δt of 20 s, a wind velocity of 6 m/s and varying emission rates (ER) and measurement noise levels. Plot (c) and (f) display the average RMSE and ME for a Δt of 20 s, a wind velocity of 10 m/s and varying emission rates (ER) and measurement noise levels. All plots are complemented by a single standard deviation error-bar of the average RMSE and ME values. 32

3.13 Architecture CVision-CIVnet and CVision-CIVnetcst. 36

3.14 The first CO2 plume image in the image pair is displayed in plot (a). The resulting wind velocity field estimated by CVision-CIVnet is displayed in plot (b). For reference, the true wind velocity field filtered for pixel locations in l_p and the difference between the estimated and true wind velocity fields are displayed in plots (c) and (d) respectively. The plume characteristics included a true wind velocity of 6 m/s, an emission rate of 25 MT/y, a l_0 measurement noise level and a Δt of 50 seconds. 37

3.15 Accuracy plot of the wind velocity field estimated by CVision-CIVnet displayed in Figure 3.14. For perfect estimation, all points in the scatter plot lie on the red diagonal line. The scatter plot is color-coded with the horizontal distance from the emission source. 38

3.16 Plot (a) and (d) display the average RMSE and ME, respectively, for a Δt of 100 s, a wind velocity of 3 m/s and varying emission rates (ER) and measurement noise levels. Plot (b) and (e) display the average RMSE and ME for a Δt of 50 s, a wind velocity of 6 m/s and varying emission rates (ER) and measurement noise levels. Plot (c) and (f) display the average RMSE and ME for a Δt of 30 s, a wind velocity of 10 m/s and varying emission rates (ER) and measurement noise levels. All plots are complemented by a single standard deviation error-bar of the average RMSE and ME values. 39

3.17 Plot (a) and (d) display the average RMSE and ME, respectively, for a Δt of 100 s, a wind velocity of 3 m/s and varying emission rates (ER) and measurement noise levels. Plot (b) and (e) display the average RMSE and ME for a Δt of 50 s, a wind velocity of 6 m/s and varying emission rates (ER) and measurement noise levels. Plot (c) and (f) display the average RMSE and ME for a Δt of 30 s, a wind velocity of 10 m/s and varying emission rates (ER) and measurement noise levels. All plots are complemented by a single standard deviation error-bar of the average RMSE and ME values. 41

3.18 Plot (a) displays a comparison of the mean wind velocity, $\bar{u}_i^p$, and plot (b) displays a comparison of the estimate CO2 flux, Q_i^p. Both comparisons are made between wind velocities estimated by the CIV Algortihms, CVision-CIVnet and the true wind velocity field displayed in Figure 3.9 and Figure 3.14 respectively. The image pair in Figure 3.9 and Figure 3.14 were characterized with a true wind velocity of 6 m/s, a Δt of 50 seconds, an emission rate of 25 MT/y and l_0 measurement noise level. 43

3.19 Accuracy plot of CO2 emission rates estimated using true wind velocity fields for noiseless image pairs in DB_{TANGO} with varying wind velocities and emission rates. The red line indicates perfect estimation while the black line displays an estimated linear regression on the estimated-to-true emission rate mapping. . 45

3.20 Plots (a), (b), and (c) show the average error of ER^{CIV} and $ER^{CVision}$ for a Δt of 100 s and a wind velocity of 3 m/s, corresponding to measurement noise levels l_0, l_1, and l_2, respectively. Plots (d), (e), and (f) show the average error of ER^{CIV} and $ER^{CVision}$ for a Δt of 50 s and a wind velocity of 6 m/s, corresponding to measurement noise levels l_0, l_1, and l_2, respectively. Plots (g), (h), and (i) show the average error of ER^{CIV} and $ER^{CVision}$ for a Δt of 30 s and a wind velocity of 10 m/s, corresponding to measurement noise levels l_0, l_1, and l_2, respectively. All plots are complemented by a single standard deviation error-bar of the average errors of ER^{CIV} and $ER^{CVision}$. 46

3.21 Plots (a), (b), and (c) show the average error of ER^{CIV} and $ER^{CVisioncst}$ for a Δt of 20 s and a wind velocity of 3 m/s, corresponding to measurement noise levels l_0, l_1, and l_2, respectively. Plots (d), (e), and (f) show the average error of ER^{CIV} and $ER^{CVisioncst}$ for a Δt of 20 s and a wind velocity of 6 m/s, corresponding to measurement noise levels l_0, l_1, and l_2, respectively. Plots (g), (h), and (i) show the average error of ER^{CIV} and $ER^{CVisioncst}$ for a Δt of 20 s and a wind velocity of 10 m/s, corresponding to measurement noise levels l_0, l_1, and l_2, respectively. All plots are complemented by a single standard deviation error-bar of the average errors of ER^{CIV} and $ER^{CVisioncst}$. 48

B.1 Simulated NOX/NO2 mass ratios plotted against the distance form the source in km. 66

List of Tables

C.1 Average RMSE's of the CIV Algorithm for a variable Δt and varying wind velocities, emission rate (ER) and measurement noise levels. Average RMSEs are displayed in m/s. 67
C.2 Average ME's of the CIV Algorithm for a variable Δt and varying wind velocities, emission rate (ER), and measurement noise levels. Average MEs are displayed in m/s. 68
C.3 Average RMSEs of the CIV Algorithm for a constant Δt of 20s and varying wind velocities, emission rate (ER), and measurement noise levels. Average RMSEs are displayed in m/s. 68
C.4 Average MEs of the CIV Algorithm for a constant Δt of 20s and varying wind velocities, emission rate (ER) and measurement noise levels. Average MEs are displayed in m/s. 68

D.1 Average RMSE's of CVision-CIVnet for a variable Δt and varying wind velocities, ER and measurement noise levels. Average MEs are displayed in m/s. 69
D.2 Average ME's of CVision-CIVnet for a variable Δt and varying wind velocities, ER and measurement noise levels. Average MEs are displayed in m/s. 70
D.3 Average RMSEs of CVision-CIVnetcst for a constant Δt of 20s and varying wind velocities, ER, and measurement noise levels. Average RMSEs are displayed in m/s. 70
D.4 Average MEs of CVision-CIVnetcst for a constant Δt of 20s and varying wind velocities, ER and measurement noise levels. Average MEs are displayed in m/s. 70

E.1 Quantification of Signal-to-Noise-Ratio's of CO2 plume with varying wind velocities, emission rates and measurement noise levels. The Signal-to-Noise-Ratio is computed using Equation E.1. 71
E.2 Quantification of Signal-to-Noise-Ratio's of NO2-converted-to-CO2 plume with varying wind velocities, emission rates and measurement noise levels. The Signal-to-Noise-Ratio is computed using Equation E.1. 72

Nomenclature

Abbreviations

Abbreviation	Definition
AI	Artificial Intelligence
CCM	Cross-Correlation Map
CFM	Cross-sectional Flux Method
CIV	Correlation Image Velocimetry
CNN	Convolutional Neural Network
CS	Control Surface
CVision	Computer Vision
ER	Emission Rate
ESA	European Space Agency
FMC	Forward Motion Compensation
GHG	Greenhouse Gas
IP	Image Pair
IW	Interrogation Window
IWS	Interrogation Window Size
LES	Large Eddy Simulations
MBM	Mass Balance Method
ME	Mean Error
PIV	Particle Image Velocimetry
PPM	Parts Per Million
RMSE	Root Mean Squared Error
SNR	Signal-to-Noise Ratio
SRON	Stichting Ruimte Onderzoek Nederland
SSR	Sum of Squared Residuals
TANGO	Twin Anthropogenic Greenhouse Gas Observer
UN-FCCC	United Nations Framework Convention on Climate Change

1

Introduction

1.1. The Mission: Monitoring and Reducing Greenhouse Gas Emissions

1.1.1. Anthropogenic Emissions

The combustion of fossil fuels has resulted in increased atmospheric CO2 levels, contributing to global climate change (Quadrelli and Peterson (2007)). In recognition of the dangers and possible irreversible consequences of climate change, there exists a heightened global commitment to restricting CO2 emissions and greenhouse gas (GHG) emissions in general. A primary goal of the United Nations Framework Convention on Climate Change (UN-FCCC) Paris Agreement is to reduce these emissions. Consequently, there is a growing interest in identifying sectors responsible for large CO2 emissions and accurately quantifying their environmental impact.

Power generation in the form of electricity comprises over 40% of the total anthropogenic emissions of CO2 (World Nuclear Association (2024)). Despite the growing competitiveness of renewable energy costs, new inefficient power plants continue to be constructed, adding substantial uncertainty to the future trajectory of anthropogenic CO2 emissions. To effectively address this issue and enhance CO2 emission management, there is a pressing need for improved quantification methods at various spatial scales, ranging from national to facility level. This is particularly crucial in emerging economies where emission reporting systems are often lacking, contributing to the global uncertainty in the quantification of anthropogenic CO2 emissions (Wilkes et al. (2017)). DeCola and Secretariat (2017) and Ciais et al. (2015) have indicated that quantifying anthropogenic emissions at the individual facility level is imperative for enhancing emissions monitoring in order to support the regulation of carbon trading/pricing systems proposed by several present international treaties (Perdan and Azapagic (2011)).Currently, significant discrepancies exist in the total anthropogenic emission estimates for point sources (Hogue et al. (2016)). The reduction of the uncertainty of point source emission rate estimates will play an important role in monitoring and reducing GHG emissions (Turnbull et al. (2016)).

1.1.2. Estimating Emission rates

Unfortunately, CO2 and GHG emission rates can not be accurately and practically measured directly, but instead need to be inferred from emission characteristics that can be measured directly (Nassar et al. (2017)). These emission characteristics include but are not limited to spatial, concentration, and temporal differences between measurements of an emission plume originating from a power plant, entire industrial facility, or urban region. Emission characteristics can be obtained through measurements of the emission plume, measurements which can originate from in situ measurement techniques or remote sensing techniques from space.

In situ measurements for emission rate estimation are challenging to obtain due to limited access, the complex nature of emission sources within facilities and spatial and temporal variability in emissions. These factors, including restricted access to power plant sites, the variety of emission sources, and the high costs and technical demands of monitoring, pose significant obstacles to obtaining accurate in situ measurements. Additionally, obtaining measurements in situ is not easily scalable to the entire power plant industry or general GHG emitters. Due to these limitations, in situ measuring is typically used for emissions estimation on smaller scales or unique case studies (Jeong et al. (2005), Lushi and Stockie (2010), Brantley et al. (2014), Foster-Wittig et al. (2015), Brantley et al. (2015), and Hosseini and Stockie (2016)).

A second way of obtaining the required emission characteristics relies on remote sensing techniques from space, which display less variability compared to in situ measurements since measurements from space are inherently smoothed due to their relatively low spatial resolution (Bovensmann et al. (2010)). Moreover, once such measurement infrastructure is in place, it is easily scalable and applicable to power plants and similar GHG emission sources around the world independent of national protocols of emission rate reporting (Cusworth et al. (2021)). Using these remote sensing techniques, emission plumes can be extracted and studied to estimate the emission rates. Streets et al. (2013) have indicated the importance and difficulty of estimating emission rates and how remote sensing techniques with high resolution and agility are key to reducing uncertainties in emission rate estimates. Therefore, when estimating emission rates from individual point sources, researchers are motivated to utilize remote sensing techniques. Preferably, these methods should offer increased resolution compared to current remote sensing infrastructure and the ability to repeatedly image different point sources.

Before any emission rates are estimated, emitters must be precisely localized from measurements obtained by remote sensing techniques. Presently, there exist three techniques of reliably detecting emissions plumes from remote sensing techniques: either algorithms based on statistical methods (Kuhlmann et al. (2021)) or based on traditional image processing algorithms (Walt et al. (2014)) or algorithms implementing machine learning (Finch et al. (2022)). The effectiveness of each method greatly depends on the setting in which it is applied, since there exists disparity in the detectability of emissions. This discrepancy arises from two main factors (Barratt (2013), Kuhlmann et al. (2021)). Firstly, certain pollutants, like CO2, are naturally present in the atmosphere. Consequently, when measuring emission concentrations for these pollutants, a significant background concentration is observed in the absence of anthropogenic emissions. This background concentration differs and this discrepancy can substantially affect image contrast, thereby influencing the detectability of emissions. Secondly, emitted pollutants can undergo diverse interactions with the atmosphere. These interactions range from various forms of atmospheric transport to reactions with naturally occurring compounds in the atmosphere. They have the potential to greatly limit or completely hinder the detectability of emissions affected by them.

1.1.3. Twin Anthropogenic Greenhouse Gas Observers

Obtaining emission measurement from remote sensing methods often relies on coarse spatial resolutions (Streets et al. (2013), Nassar et al. (2017)), making it challenging to locate individual emission sources accurately. The aggregated data from such techniques may not capture the subtle variability and intensity of emissions from specific industrial facilities, urban areas or natural sources. This limitation stems from the generally low spatial resolution, which hampers the observation of fine-scale patterns and localized peaks in observed emissions. Therefore, detailed measurements of individual emissions point sources are especially important to eliminate the large discrepancies between true and estimated anthropogenic GHG emission rates (Hogue et al. (2016)). Therefore, there is a critical need for higher resolution remote sensing methods.

To satisfy this need, the Twin Anthropogenic Greenhouse Gas Observers (TANGO) mission emerges as a pioneering satellite initiative set to make significant contributions to global environmental monitoring. Designed to address the need for accurate measurements of anthropogenic GHG emissions, TANGO represents a new approach in the realm of Earth observation (Landgraf et al. (2020)). TANGO comprises two satellites, TANGO-Carbon and TANGO-Nitro, flying in close formation with a minimal time difference of $\Delta t < 60$ seconds. TANGO's mobility enables it to aim directly at known emission sources every three to four days, providing precise and frequent measurements. Additionally, its unique design allows TANGO to provide independent and precise measurements of emissions from industrial facilities at a spatial resolution as high as 300 m x 300 m. This spatial resolution is comparatively higher than the resolution of its predecessors (7 km x 3.5 km TROPOMI Copernicus Open Access Hub (2024), 1.29 km x 2.25 km OCO-2 eoPortal (2024)) which had similar objectives of measuring anthropogenic GHG emissions.

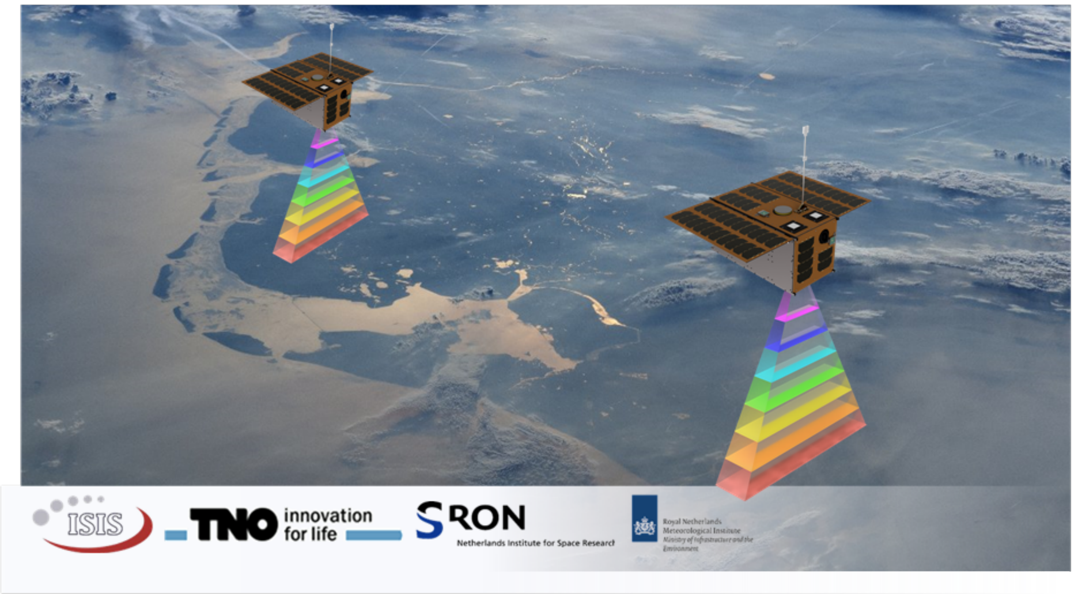

Figure 1.1: Depiction of the Twin Anthropogenic Greenhouse Gas Observers mission. The image displays the two CubeSats called TANGO-Carbon and TANGO-Nitro in the same orbit spaced by Δt.
Source: SRON (2023)

Due to its capabilities, the TANGO satellite mission is positioned as a crucial step toward realizing the goals set by the Paris Agreement. TANGO's data will complement major European satellite missions, enhancing the detection capabilities of the European Space Agency (ESA) Sentinel 5 mission. This relatively small mission allows for swift realization, with data becoming available after its planned launch in 2027 (SRON (2024)). This early availability provides an additional year of data collection, contributing to the UN-FCC Global Stock Take scheduled for 2028 and supporting the fulfillment of Paris Agreement goals.

1.1.4. Problem Statement

The TANGO mission enables a significant advancement in the monitoring of GHG emissions. The mission, comprising two satellites, TANGO-Carbon and TANGO-Nitro, is designed to measure NO2, CO2, and CH4 gases globally and independently from 2027 to 2031. The capabilities of TANGO which comprise stereo imaging and high spatial resolution, establish a unique framework that enables the application of new estimation methods for individual emission rates.

In conventional emission rate estimation methods for CO2, a combination of gas concentration measurements with wind velocity fields estimated from meteorological data is used. Yet, these established methods introduce substantial uncertainties in emission rate estimates through the relatively uncertain wind velocity field estimates. To address this challenge, this thesis aims to investigate alternative methods, enabled by the unique framework created by TANGO, that directly measure the velocity of the emission plume from concentration measurements. These alternative methods would eliminate the dependency on uncertain and sparsely available meteorological data altogether.

Once these alternative methods have been implemented, the level of uncertainty achievable using alternative methods will be obtained and studied. Therefore, this thesis will also aim to investigate the factors influencing the accuracy of emission rate estimation utilizing direct plume velocity measurements and identify the optimal design for mission parameters, measurement strategies, and analysis techniques.

1.2. Emission Rate Estimation Methods

Unfortunately, emission rates cannot be measured directly. Instead, emission rates can only be inferred from plume characteristics once plumes have been detected. In the case of emissions in our atmosphere, which are transported by diffusion and advection, there currently exist several methods to estimate emission rates: inverse methods, mass balance methods, and the novel computer vision approach.

1.2.1. Inversion Methods

Inversion methods involve the iterative adjustment of emission parameters until modeled concentration distributions closely match measured concentration distributions. These methods leverage atmospheric dispersion models to simulate the transport and dispersion of pollutants, considering complex factors such as wind velocity patterns and atmospheric stability.

Roberts (1923) and Sutton (1931) were the first to study atmospheric dispersion problems subject to several different assumptions, boundary conditions, and parameters. Their studies introduced a new diffusion coefficient, aiming for constancy over varying spatial scales, building upon the concept of eddies with a novel consideration for its size variation based on the characteristic length scale of diffusing. Additionally, the main finding suggests that turbulent scattering of suspended matter or temperature diffusion in the atmosphere can be likened to heat diffusion in solids, with a variable eddy-diffusion coefficient. Their new analytical and exact solutions have proven to be invaluable in today's world with use cases varying from modeling dispersals of smell (Smith (1993)) to volcanic eruptions (Turner and Hurst (2001)). For more detailed information with regards to different types of atmospheric dispersion models, the reader is referred to Holmes and Morawska (2006).

Solutions provided by Roberts and Sutton and their present extensions have proved to be very useful. However, they do not only enable atmospheric dispersion problems to be modeled given the characteristics of the emission source and atmosphere; they also provide the framework to inversely estimate these characteristics which might be inherently unknown or hard to determine. The emission rate is one of them and can be determined inversely using solutions to atmospheric dispersion models. These inverse methods use information about and related to emissions sources as inputs for estimating the emission rate to a relatively high degree of accuracy. Often these inputs prove relatively easy to obtain.

Emission rate estimation methods which rely on inverse methods have greatly been used in literature, where the inverse Gaussian plume model has been predominately applied (Hutchinson et al. (2017)) due to its relative simplicity and fast computation. This model is mainly governed by the atmospheric turbulence coefficients σ_y and σ_z, defined as the standard deviation related to mixing due to wind in orthogonal directions to the main direction of advection experienced by the emission source. The eventual derivation of σ_y and σ_z is highly dependent on the use case of the atmospheric dispersion model and its underlying assumptions (Pasquill (1961) and Stockie (2011)). The equation of the Gaussian plume model is defined in Equation 1.1.

$$C(x, y, z, Q) = \frac{Q}{2\overline{u}\sigma_y\sigma_z\pi} \exp^{\left(-\frac{y^2}{2\sigma_y^2}\right)} \left[\exp\left(-\frac{(z-H)^2}{2\sigma_z^2}\right) + \exp\left(-\frac{(z+H)^2}{2\sigma_z^2}\right)\right] \tag{1.1}$$

where C is a concentration at position x,y,z and Q is the emission rate. Parameter $\bar{u}$ represents the uniform wind speed in the x direction and σ_y and σ_z represent the atmospheric turbulence coefficients. H represents the height at which the emissions are released. For the complete derivation, the reader is referred to Stockie (2011).

Krings et al. (2011) were the first to use this technique for emission rate estimation of individual point sources which resulted in promising results. Their research was quickly extended using different atmospheric turbulence coefficients and applied to estimate emission rates of several different facilities and sectors, including individual power plants (Jeong et al. (2005), Lushi and Stockie (2010), Hosseini and Stockie (2016), Nassar et al. (2017), Zheng et al. (2019), Hu and Shi (2021), Li et al. (2024)).

Typically, inversion methods are relatively trivial to apply to estimate emission rates if coupled with simple atmospheric dispersion models. However, their applicative ease originates from the same characteristic that creates their main limitations; namely, their underlying assumptions prove to be mere approximations in most cases. Assuming a constant and uniform wind velocity, for example, is one of those assumptions that proves to be unrealistic when applied to real-world scenarios because of the dynamic and heterogeneous nature of atmospheric processes. The atmosphere is characterized by a wide range of spatial and temporal variations in temperature, pressure, humidity, and other factors, leading to complex and variable wind patterns. Additionally, factors such as topography, land use, and atmospheric phenomena introduce further complexity and non-uniformity into wind patterns. Varon et al. (2018) have indicated that such unrealistic assumptions can cause large deviations between true and estimated emission rates. Relying on more complicated atmospheric dispersion models which depend on fewer assumptions has been shown to increase the accuracy of emissions estimates, however, their increase in complexity limits their applications.

1.2.2. Mass Balance Methods

In Mass Balance Methods (MBM), the estimation of emission rates involves applying the divergence theorem. This theorem results from the mass balance principle, which determines how the mass within a control volume changes (White et al. (1976), Pichler (1986)). It achieves this by considering the integrated mass flux through the walls of a control volume or boundaries of a control surface. The control volume is often defined as a box shape capturing the area of the facility of interest, whereas the control surface could be taken at any point within the plume perpendicular to the direction of the wind. This technique does not depend on approximations or assumptions to the same degree as inverse methods; apart from external wind measurements, it solely depends on the measurements taken of the control volume or at the control surface. These required measurements often originate from remote sensing methods from space.

White et al. (1976) were the first to apply the principle of mass balance to quantify atmospheric fluxes. Their approach relied on determining the emission flux through several control surfaces using remote sensing measurements of atmospheric concentrations and local wind measurements. The horizontal mass flux F of a compound of interest across a control surface (CS) can be described as follows:

$$F = \oiint_{CS} u_n(x,z)\,[C(x,z) - C_0(x,z)]\; dS \tag{1.2}$$

where x is the distance downwind of the plume, and y and z are the crosswind and vertical coordinates, respectively. Here, $u_n(x,z)$ represents the component of the wind speed normal to the control surface. $C(x,z)$ is the concentration of interest, and $C_0(x,z)$ is the average background concentration, both derived from remote sensing measurements.

Following the publication of their proof of concept by White et al. (1976), numerous studies and applications have utilized the principle of mass balance to estimate emissions from urban areas (Trainer et al. (1995), Beirle et al. (2011), Cambaliza et al. (2014), Kuhlmann et al. (2020)), oil fields (Karion et al. (2013), Gordon et al. (2015), Baray et al. (2018), Yang et al. (2018), Fried et al. (2020)), wild fires (Goudar et al. (2023)) and individual power plants (Ryerson et al. (1998), Kuhlmann et al. (2021), Kim et al. (2023), Wong et al. (2024)). These studies all used remote sensing methods as their source of measurements.

MBMs are known for their relatively simple application since they only depend on the concentration distribution and wind velocity field. Additionally, unrealistic assumptions used in inversion methods are no longer present in MBMs. However, they also have their fair share of limitations that restrict the number of use cases due to flow regimes that dominate the atmospheric flow. For example, Varon et al. (2018) have shown that the results of the majority of MBMs collapse when atmospheric flow is dominated by diffusion instead of advection.

1.2.3. Computer Vision Methods

The two estimation methods that were discussed in the previous two sections solely relied on concentration measurements and wind velocity data. However, as Jongaramrungruang et al. (2019) have indicated, information with respect to the morphology of present or current emission plumes can also be used up to a certain extent to estimate emission rates of individual power plants with increased accuracy.

These deductions and findings motivated researchers to apply the pattern and shape recognition capabilities of Computer Vision (CVision) to the problem of emission rate estimation of individual power plants. CVision is an interdisciplinary field at the intersection of Computer Science and Artificial Intelligence (AI) which focuses on creating machine learning networks with the ability to understand and interpret visual data. Their capability to extract features, such as patterns, edges, or textures, enables them to create a meaningful interpretation of an image. These capabilities originate from the hierarchical structure present in the majority of CVision machine learning networks which are comprised of several fully connected convolutional layers. This structural design facilitates the detection and extraction of intricate visual features across vast datasets. Due to their versatile capabilities, these machine learning networks are used in several disciplines (Szeliski (2022)) including multiple environmental science-related problems based on remote sensing techniques (Pan et al. (2020), Kumar et al. (2020), Wang et al. (2020)).

Jongaramrungruang et al. (2022) were the first to apply CVision directly to the problem of emission rate estimation. In doing so, they constructed MethaNet, a convolutional neural network (CNN) consisting of ten layers, five of which were convolutional layers capable of localizing and quantifying CH4 emissions source rates of individual power plants, using simulated remote sensing data as input. MethaNet improved the accuracy of emission rate estimates significantly compared to methods that require information with respect to the local wind velocities. Additionally, MethaNet is also capable of estimating emission rates at locations where wind information is unavailable.

Since the introduction of MethaNet, Joyce et al. (2022) and Radman et al. (2023) have extended the research into the identification and quantification of CH4 emissions based on Sentinel-2 and PRISMA hyperspectral satellite imagery, respectively, instead of artificially simulated data. Furthermore, Radman et al. (2023) studied deep learning architectures extended by multiple convolutional layers created for emissions detection and quantification, resulting in an architecture called S2MetNet which is capable of outperforming MethaNet. Additionally, Jahan et al. (2023) have applied similar CVision techniques to detect and quantify emissions originating from leakage in the oil and gas industry. Their proposed CNN, which was comprised of five convolutional layers in a hierarchical structure, was capable of detecting and quantifying leaks reliably and more accurately compared to methods dependent on wind information. These studies have shown promising results in the field of emission rate estimation, however, their applications are limited since the training procedures of their CVision networks are quite niche and not applicable to general settings and pollutants.

1.3. Combination of CO2 and NO2 Emissions

One challenge in the estimation of emissions, particularly for CO2, lies in accurately detecting emission plumes amidst the background concentrations present in the atmosphere. The surrounding atmospheric conditions, influenced by various pollutants, can impact the detectability of emitted GHG plumes (Kuhlmann et al. (2021)). Pollutants with minimal background concentrations offer clearer detection of increased emissions (Kuhlmann et al. (2021)).

Processes predominantly emitting GHGs are characterized by a mix of emissions. For instance, emission plumes from sources like cities, power plants, or wildfires often contain a combination of CO2 and NO2 emissions (Hakkarainen et al. (2021)). Both CO2 and NO2 disperse similarly in the atmosphere due to their similar coefficients of diffusion and molecular weights (Massman (1998)), with slight variations in dispersion due to factors like the decay rate of NO2 at different elevations and exposures to sunlight (Hakkarainen et al. (2021)). However, these variations are considered insignificant compared to the accuracy of CO2 concentration measurements (Bovensmann et al. (2010)).

As a result, researchers leverage the temporal and spatial correlation between these CO2 and NO2 emissions. CO2 concentration measurements face challenges in detecting plumes due to increased background concentrations and reflective properties of CO2. In contrast, NO2 concentration measurements are less hindered, as NO2 has a short atmospheric lifespan and negligible background concentrations (Seinfeld and Pandis (2016)). This characteristic makes NO2 concentrations less affected by long-range transport, allowing for more robust interpretation in a local setting (Goldberg et al. (2019)). Given the high correlation between CO2 and NO2 emissions, information from NO2 emissions aids in enhancing the detection and quantification of CO2 emissions.

Numerous studies have capitalized on the spatial and temporal correlation of CO2 and NO2 emissions to improve CO2 emission rate estimates. For instance, Kuhlmann et al. (2021) accurately constrained the shape of CO2 emission plumes from power plants by using information derived from the corresponding NO2 emission plume measurements. They applied a MBM to the CO2 plume and explored the use of known ratios between CO2 and NO2 concentrations (Reuter et al. (2014)) to infer the true shape of the CO2 emission plume solely based on NO2 plume information. Similarly, Yang et al. (2023) investigated CO2 and NO2 emission plumes from urban areas, utilizing NO2-derived CO2 concentration distributions through empirical relationships to estimate emission rates with a MBM.

1.4. Wind Velocity

As previously mentioned, the integration of wind velocity fields plays an important role in both inversion methods and MBMs for estimating emission rates. In inversion methods, wind velocity is a critical input for atmospheric dispersion models, refining the accuracy of simulations and facilitating the iterative adjustment of emission parameters based on observed concentrations. Similarly, in MBMs, wind velocity fields are essential for tracking the downwind transport of emissions and calculating emission rates based on the principle of conservation of mass. The only technique that does not depend on wind velocity data are estimation methods using CVision. However, these CVision applications are constrained by the necessity for extensive labeled datasets of flow consisting of high-contrast imagery, limiting its practical implementation and scope (Jongaramrungruang et al. (2022)). Due to these limitations, it is imperative to improve the accuracy of emission rate estimation methods that do not entirely rely on CVision. The accuracy of their estimates could be significantly improved by access to accurate knowledge of wind dynamics.

True local wind velocity fields can be estimated in several ways. On the one hand, one can rely on published meteorological data such as the Merra-2 database to estimate local atmospheric conditions. However, estimating atmospheric conditions based on meteorological data has an inherent degree of uncertainty. The uncertainty in meteorological data related to wind velocities stems from various factors such as temporal variability, driven by weather phenomena such as gusts or fronts. Height dependency also contributes to uncertainty as wind profiles vary with height above the ground, requiring extrapolation methods that may not always accurately account for complex atmospheric conditions. These extrapolation methods further compound uncertainty, as it often relies on assumptions about the spatial or vertical distribution of wind that may not be universally applicable.

This inherent uncertainty of wind velocity fields estimated by meteorological data can significantly affect the accuracy of emission rate estimates (Benjamin et al. (2016)). However, the uncertainty with respect to estimating emission rets needs to be reduced in order to eliminate the discrepancies in total emissions monitoring (Hogue et al. (2016), Turnbull et al. (2016)). Therefore, it proves beneficial to strive for wind velocity field estimates which prove to be more accurate and responsive compared to wind velocity field estimates based on meteorological data.

An alternative to using meteorological data would be to rely on local wind velocities that are estimated from observed atmospheric conditions, such as satellite imagery. Dvorak (1975) was the first to utilize images of storms to estimate the wind velocity of these storms and their surroundings. This method relied on the tracking of features within storms based on computed correlations between temporally spaced images of the same storm, in order to infer the wind velocity on local scales. Presently, this technique has been extended and shown to deliver promising results with respect to wind velocity estimates (Nezhad et al. (2021)). These exact techniques are solely applicable to satellite imagery of storms over large parts of the oceans, however, research into this topic has indicated that it is possible to track features in the atmosphere to estimate the local wind velocities. However, tracking features within emission plumes for wind velocity estimation presents distinct challenges compared to tracking features in clouds. Plumes display variability in altitude, leading to variations in wind speed and direction at different levels of the atmosphere. Currently, two methods show promise in the literature for tracking features in emission plumes to estimate local wind velocities: traditional Correlation Image Velocimetry and Computer Vision Correlation Image Velocimetry.

1.4.1. Correlation Image Velocimetry

The most common type of velocimetry, the class of techniques used to determine and quantify fluid flow, is characterized by visualizing fluid flow, often by seeding the fluid with reflective particles or some colorful medium and observing the flow velocity field. This technique dates back several centuries (Gharib et al. (2002)) and has since been studied extensively. The development of high-speed and high-resolution digital cameras and advanced lasers greatly accelerated the field of optimal flow visualization. Barker and Fourney (1977), Dudderar and Simpkins (1977) and Grousson and Mallick (1977) were the first to independently demonstrate the use of laser illumination and reflection to infer flow velocity fields. They all relied on double-exposure imagery of small windows within the flow where prominent laser speckles were present. In the research that followed, it became clear that the presence of reflective particles mainly contributed to the accurate inference of flow instead of the presence of laser speckles. As a result, Pickering and Halliwell (1984) and Adrian (1984) proposed the concept of imaging flows that were primarily seeded with highly reflective particles and using imagery of laser reflections, given the temporal difference and pixel size, to estimate the flow velocity field. As such, the technique of Particle Image Velocimetry (PIV) was born. The technique of PIV was quickly extended by Tokumaru and Dimotakis (1995) who tracked and matched patterns between imagery of un-seeded flows in order to estimate the velocity field. Since their approach no longer depended on the tracking of seeded particles, this extension was called Correlation Image Velocimetry (CIV).

PIV, as presently defined by Abdulwahab et al. (2020), is a technique that relies on spotting the motion of seeded tracer particles present within the fluid through correlations. PIV is known for its wide variety of possible applications ranging from laminar to high-speed turbulent flows. While CIV, as defined by Fincham and Spedding (1997) is a technique that relies on the matching of well-defined optical patterns present in the flow between a pair of images. These patterns can already be present or introduced in the flow. CIV is often preferred over PIV when seeding flow with particles is not feasible or desirable.

Among both techniques, PIV has predominately been applied in literature (Schröder and Willert (2008), Gonzalo et al. (2014), Abdulwahab et al. (2020)). It is often used on small-scale flow fields where detailed flow velocity fields such as eddies or vortex shedding need to be exposed. However, it has also been applied on larger scales estimating wind speeds and direction within the atmosphere (Hagura and Koizumi (1990), Wilkerson et al. (2012), Domínguez et al. (2013)). CIV on the other hand has been applied less extensively in literature. Due to the effects of turbulent mixing and diffusivity within the atmosphere, direct pattern matching between features that change over time within the flow becomes hard. In contrast to PIV which uses seeded particles that are constant in size and reflectivity, features used in CIV are a function of time and thus subject to change due to the temporal difference between images. However, when diffusivity does not dominate the atmospheric flow regime, CIV could prove effective in estimating wind velocity (Tokumaru and Dimotakis (1995) and Fincham and Delerce (2000)). Unfortunately, this application of CIV has been studied less extensively compared to its PIV counterpart.

CIV, and PIV for that matter, rely on tracking and matching optical patterns present in the flow. Clear imagery of these patterns that change over time is essential to enable the tracking and matching thereof. If one can observe similar patterns in multiple successive images, it becomes possible to study their resemblance in these images and estimate the local linear displacement vector of these patterns. This is achieved by selecting sub-regions within two different images, called interrogation windows (IW), and subjecting them to statistical analysis to infer the local linear displacement vector.

This statistical analysis can be defined as follows: from two successive images which are separated by a certain time difference Δt, two IWs can be extracted, $I \in \mathbb{R}^{NxN}$ and $I' \in \mathbb{R}^{MxM}$, which are essentially 2D intensity fields centered around an arbitrarily selected pixel. I is extracted from the first image and I' is extracted from the second image where I' is larger in size than I (N < M). Now for a possible shift (x,y) in pixels, that is a shift in the location of the center of I and I′, one can apply Equation 1.3 in combination with Equation 1.4, 1.5 and 1.6 to determine the normalized cross-correlation between the two extracted IWs. Note that this pixel shift represents a possible displacement between the centers of I and I′ which could have taken place in the Δt that spaces I and I′.

$$cc_{II'}(x,y) = \frac{CC_{II'}(x,y)}{\sqrt{\sigma_I(x,y) * \sigma_{I'}(x,y)}} \tag{1.3}$$

$$CC_{II'}(x,y) = \sum_{i=0}^{N}\sum_{j=0}^{N}[I(i,j) - \mu_I][I'(i+x, j+y) - \mu_{I'}(x,y)] \tag{1.4}$$

$$\sigma_I(x,y) = \sum_{i=0}^{N}\sum_{j=0}^{N}[I(i,j) - \mu_I]^2 \tag{1.5}$$

$$\sigma_{I'}(x,y) = \sum_{i=0}^{M}\sum_{j=0}^{M}[I'(i,j) - \mu_{I'}(x,y)]^2 \tag{1.6}$$

The value μ_I is the average of I and is computed only once while μ_I(x,y) is the average of I′ centered at position (x,y). The value of $c_{II'}(x,y)$ is an indication of the degree of similarity between both IWs; if $c_{II'}(x,y)$ is 1, I and I′ are perfectly correlated and thus completely similar, if $c_{II'}(x,y)$ is 0, I and I′ are completely uncorrelated and share no similarities what so ever.

By performing this operation across a range of shifts ($-N \leq x \leq N$, $-N \leq y \leq N$), a two-dimensional cross-correlation map (CCM) is generated. Essentially, I is systematically shifted within I′ without overlapping its edges. At shift positions where the patterns within I and I′ align, the sum of the pixel intensity products will be notably higher compared to other positions, resulting in an elevated cross-correlation value at these coordinates. Fundamentally, the cross-correlation function statistically quantifies the level of similarity between the two samples for a given shift. One can extract the coordinates of the peak within the CCM to determine the pixel shift which corresponds with the most probable linear displacement vector between I and I′ (Raffel et al. (2018)). Once this linear displacement vector is known, one can use the pixel size and the Δt between windows I and I′ to determine the most probable velocity vector of the flow that caused the displacement. To obtain a flow velocity field from a pair of images, one selects a uniformly distributed pixel distribution (parameters that can correspond to the specific use case) within the image domain. Then for every pixel within this pixel distribution, select a pair of IWs, I and I′, which are centered around this selected pixel. Next, the most probable linear displacement vector is selected by determining the location of the CCM peak by applying Equation 1.3, 1.4, 1.5 and 1.6 for all possible pixel shifts.

When applying Equation 1.3, 1.4, 1.5 and 1.6, one essentially tracks features within a flow over time by cross-correlating images. These features exist in the true flow and are measured through imagery. However, obtaining these images can be challenging, unreliable, or inaccurate. Measurement techniques inherently introduce some form of noise to images of the true flow. The quantification of the introduced noise with respect to the measured signal can be expressed as the Signal-to-Noise Ratio (SNR).

$$\text{SNR} = \frac{X_{obs} - X_{bgr}}{\sqrt{\sigma_{rand}^2 + \sigma_{sys}^2}}. \tag{1.7}$$

where $X_{obs}$and X_{bgr} represent the mean of the observation signal and background signal respectively. σ_{rand} and σ_{sys} represent the random and systemic errors observed in the signal respectively.

The SNR within imagery greatly affects the ability of features to be tracked and flow velocities to be estimated using methods such as CIV. Low SNR imagery is characterized by having low contrast within the flow. Therefore, observing clear features becomes difficult due to the increased effect of noise in the image. This increased noise propagates through statistical analysis performed on the image. And as a result, correlation peaks in the CCM become less distinct and more difficult to locate. In the worst case, spurious correlation peaks could arise, rendering the implementation of CIV impractical. Therefore, higher SNRs are preferred when applying CIV to estimate flow velocity fields. To achieve this, one can attempt to reduce the total noise introduced by sensing techniques. This can be achieved by employing more precise imaging equipment or reducing the total Δt between the pair of images, thereby minimizing the contribution of measurement noise (Raffel et al. (2018)). However, the total observed linear displacement, which is a function of Δt, still needs to be within the same order of magnitude as the pixel size of the image. If this is not the case, displacements become unobservable and features untrackable. Another way of increasing the SNR is by increasing the size of the IW to artificially decrease the SNR of the total IW (Raffel et al. (2018)).

In the context of CIV, the accuracy of flow velocity estimates is influenced by how well the cross-correlation procedure between interrogation windows can capture the statistical properties of the flow. While individual features in the flow are not explicitly tracked, the aggregate signal from all detectable features contributes to the CCM. Although features with a length scale smaller than half a pixel size may not be individually resolvable, they still contribute to the signal measured in each pixel and play a role in the cross-correlation procedure. The relationship between feature size, interrogation window size (IWS), and pixel size is crucial for accurate flow velocity estimates. If the IWS is too small relative to the feature size, it may reduce the effectiveness of the cross-correlation procedure between interrogation windows. Furthermore, the dominant flow regimes influence the reliability of the cross-correlation procedure over time. In highly turbulent atmospheric flows, for example, turbulent diffusion can rapidly decorrelate measurements between interrogation windows spaced by Δt, reducing the utility of the cross-correlation procedure.

Addressing these considerations requires careful attention to the size of the IW. While increasing the IWS to enhance the SNR and capture features of a certain size is desirable, it comes with challenges. With increasing IWS, the effects of displacement vector gradients become significant, leading to a broadening of the correlation peak observed in CCM and increased uncertainty in its location estimate (Raffel et al. (2018)). Thus, achieving an optimal balance between increasing the IWS to improve SNR and feature capture, while ensuring the IWS remains small enough to disregard the effects of displacement vector gradients, is crucial in CIV methodology.

The primary objective of this thesis is to investigate whether TANGO offers a framework capable of directly measuring wind velocities for use in emission rate estimation. Given its potential to provide stereo (temporally separated) imagery of plumes, the technique of CIV could be leveraged to derive a wind velocity field, facilitating the estimation of emission rates. However, several limitations and challenges associated with CIV in conjunction with the use of satellite imagery need to be addressed.

The SNR of images used in CIV is typically maintained at relatively high levels to minimize uncertainty in the estimated displacement vector. However, satellite imagery of certain pollutants, particularly CO2, often exhibits a relatively low SNR (Kuhlmann et al. (2020)) adversely affecting the clearness of the CCM peak. Moreover, the Δt between stereo images produced by TANGO is generally larger than the typical Δt values encountered in CIV or PIV literature (Abdulwahab et al. (2020)). As Δt increases, the clearness of the CCM peak decreases due to changes in the plume shape caused by local velocity variations. As a result, the accuracy of displacement estimation decreases. Additionally, the relationship between the resolution of satellite imagery, feature size, and the magnitude of observed displacements may not be favorable for CIV applications due to the capabilities of TANGO and variations in global emission plumes. Furthermore, it's important to acknowledge that the feature size within emission plumes varies temporally and spatially, significantly influencing this relationship. Given these factors—low SNR, varying feature sizes, satellite image resolution, and high Δt—it is imperative to accurately determine key CIV parameters such as the size of the IW. This is essential to ensure the validity of the flow velocity estimates in the context of TANGO-based wind velocity measurements for emission rate estimation.

1.4.2. Computer Vision CIV

Besides the traditional velocimetry methods, developments in the field of CVision and AI in general, have opened the door for its supplementary applications in the field of velocimetry. The first conceptual studies into the use of CVision to estimate velocity fields based on PIV data, date back to '90s (Teo et al. (1991), Cenedese et al. (1992), Hassan and Philip (1997), Grant and Pan (1997)). These studies all relied on relatively simple neural networks able to estimate linear displacement vectors by tracking particles within their input. From that time on, interest in CVision approaches has steadily increased, reflected in the number of studies published since (Yu et al. (2023)). As a result, there currently exist several CVision approaches capable of applying PIV, taking an image pair as input. These approaches take advantage of the current developments in the field of CVision and employ the use of CNNs to increase the performance of machine learning networks. Thus far, no methods relying on CVision have been proposed to implement CIV to estimate the flow velocity field. There have been several studies that used CVision approaches to estimate optical flow, with use cases that partly resemble use cases that use CIV (Dosovitskiy et al. (2015), Ilg et al. (2017), Manickathan et al. (2022)).

Presently, applying CVision to flow field estimation problems is often done by applying Deep Learning within neural networks characterized by having multiple layers some of which are convolutional (O'Shea and Nash (2015)). The input data often consists of some form of imagery of the visualized flow, which can be labeled or unlabeled. The labeling status of the input data is often dependent on its source and is of great importance to the way a network learns. A clear distinguishment can be made between the two different fundamental learning strategies, namely, networks can learn supervised or unsupervised (Hiran et al. (2021)).

Supervised learning is a learning paradigm where a model is trained on a labeled dataset, consisting of input-output pairs, to learn the mapping or relationship between inputs and corresponding outputs. The goal is for the model to generalize and make accurate predictions on new, unseen data based on the patterns learned during training. However, applying supervised learning to flow velocity field estimation requires the data to be labeled thus the corresponding data usually need to be simulated (Yu et al. (2023)).

This problem can be avoided by using unsupervised learning. In this learning paradigm, as the name already suggests, a network is tasked with finding patterns or structures in a dataset without explicit guidance through labeled input data. Zhang and Piggott (2020) applied this principle to flow velocity field estimation, using an innovative loss function. This unsupervised approach enjoys several benefits over its supervised counterpart, one of which is that it allows the use of unlabeled real-world data which is presently abundantly available in the field of atmospheric condition estimation. However, using an unsupervised learning approach in combination with real-world atmospheric data, to the best of our knowledge, has not been found in literature.

In contrast to these two fundamental training strategies, the concept of transfer learning from existing CVision applications holds significant promise and potential benefits. Transfer learning involves leveraging knowledge gained from training one model on a specific task and applying it to a related but different task. One key advantage of transfer learning is its ability to expedite the training process by starting from pre-trained models. By utilizing pre-trained models trained on large datasets, one can mitigate the need for extensive labeled data, which is often a bottleneck in traditional supervised learning approaches.

As outlined in Section 1.1.4, this thesis aims to explore whether TANGO provides a viable framework for directly assessing wind velocities to aid in estimating emission rates. TANGO's unique capability to capture stereo imagery of plumes suggests that employing CVision-CIV techniques could yield a wind velocity field, thereby assisting in emission rate estimations. However, it is crucial to address various limitations and challenges inherent in integrating CVision-CIV with satellite imagery.

Existing CVision machine learning networks utilized for estimating velocity fields typically operate on data with relatively high SNR. Consequently, it remains uncertain how such networks perform when confronted with the comparatively lower SNR prevalent in typical satellite imagery, particularly those capturing CO2 emissions. Additionally, the necessity of a large labeled dataset for training machine learning networks, coupled with the significant computational time required for training, poses significant hurdles. Nonetheless, these challenges could potentially be mitigated through the application of transfer learning techniques.

1.5. Summary and Discussion

Anthropogenic emissions, primarily from fossil fuel combustion, contribute significantly to rising atmospheric CO2 levels, fueling global climate change. The UN-FCCC Paris Agreement targets emissions reduction, with a focus on the power generation sector responsible for over 40% of anthropogenic CO2 emissions. Improved quantification methods are crucial, especially in emerging economies with inadequate reporting systems, contributing to global CO2 emissions uncertainty. Individual facility-level emission rate quantification becomes essential for monitoring emission reductions and supporting international carbon trading/pricing systems and general GHG reduction policies. Discrepancies in anthropogenic emission estimates underscore the need for reduced uncertainty in effective GHG management. DeCola and Secretariat (2017) and Ciais et al. (2015) highlight the importance of quantifying emissions at the individual facility level.

GHG emission rates are inferred from measurable emission characteristics, with in situ measurements suitable for smaller scales and unique case studies. Remote sensing techniques, utilizing satellite imagery, offer a scalable alternative for GHG emission measurements. Streets et al. (2013) emphasize the importance of remote sensing techniques in reducing uncertainties in estimating individual point source emission rates.

The TANGO mission addresses the challenge of obtaining accurate emissions measurements by introducing higher resolution detection methods. Comprising two mobile satellites the mission aims to provide precise and frequent measurements by targeting known emission sources every three to four days. This approach allows TANGO to independently monitor major anthropogenic GHG emissions with a spatial resolution as fine as 300 m x 300 m. The TANGO mission introduces significant advancements in monitoring anthropogenic GHG emissions, specifically CO2, NO2, and CH4 gases, globally and independently from 2027 to 2031. The unique capabilities of TANGO, including stereo imaging and high spatial resolution, provide a framework for exploring new estimation methods for emission rates. Due to the high spatial resolution, emission sources become easier to detect. Additionally, stereo imagery of plumes creates opportunities concerning new emission rate estimation methods. The fact that these stereo images comprise different concentration measurements (CO2 and NO2) does not hinder these new opportunities since there exist several promising methods that enable CO2 concentration measurements to be extracted from NO2 concentration measurements.

Present literature on estimation methods of emission rates predominately relies on concentration measurements in combination with wind velocity data from meteorological observations. Inversion methods iteratively adjust emission parameters to match modeled and observed atmospheric concentrations using atmospheric dispersion models. Sutton (1931) and Roberts (1923)) solutions form the basis for modern models, allowing for both dispersion modeling and inverse estimation of emission characteristics. Unfortunately, unrealistic assumptions may lead to deviations in estimated emission rates, especially with simple dispersion models. MBMs estimate emission rates by relying on measurements within a control volume or at control surfaces obtained through remote sensing methods. While MBMs eliminate unrealistic assumptions present in inversion methods, their application collapses under diffusion-dominated atmospheric flow regimes. The CVision approach involves utilizing Deep Learning and CNNs to estimate the velocity field of the flow. This estimation, incorporated into models, allows for emission rate estimation with promising results, however, their applications are limited.

These different estimation methods have shown to be useful in the estimation of emission rates, however, the uncertainty of their estimates is greatly influenced by their reliance on wind velocity fields originating from meteorological data. Hogue et al. (2016) have indicated that decreasing the uncertainty of emission rates is crucial. Eliminating the reliance on uncertain meteorological data could drastically decrease the uncertainty of emission rate estimates. This research aims to investigate methods enabled by TANGO's capabilities of directly measuring plume velocity from concentration measurements, eliminating the dependence on uncertain meteorological wind velocity data. The research problem centers on understanding the factors influencing the accuracy of emission rate estimates utilizing direct plume velocity measurements and identifying optimal mission parameters, measurement strategies, and analysis techniques.

There has been extensive research into the field of flow estimation, leading to the identification of two methods that could be used to estimate wind velocities from two similar concentration measurements of the same plume taken with a certain temporal difference:

- One method, CIV, relies on cross-correlating images of flow dominated by advection. While TANGO's stereo imagery capabilities hold promise for deriving wind velocity fields using CIV, challenges arise due to the low SNR in satellite imagery, large time intervals between stereo images, and varying feature sizes within emission plumes. Accurately determining key CIV parameters, such as the IWS, becomes crucial.
- The second method involves the use of AI, enabling the implementation of CVision-CIV. In this case, adapting machine learning networks to the low SNR of satellite imagery, along with the need for large labeled datasets and significant computational time for training, presents challenges. However, the potential of transfer learning techniques offers hope for addressing these hurdles and enhancing wind velocity estimation using TANGO's capabilities.

2

Research Outline

The TANGO mission marks a significant stride in reshaping the landscape of anthropogenic greenhouse gas emissions monitoring. Comprising two satellites, TANGO-Carbon and TANGO-Nitro, this mission is poised to independently measure global concentrations of CO2, NO2, and CH4 from 2027 to 2031. TANGO's unique features, such as its high spatial resolution and stereo imaging capabilities, create a framework that allows for the development of new techniques for estimating individual emission source rates.

In traditional approaches, the estimation of CO2 and NO2 emission source rates relies on a combination of gas concentration measurements and wind velocity fields estimated from meteorological data. However, the inherent uncertainties associated with meteorological data introduce substantial challenges in accurate emission rate predictions. To tackle this issue, this research endeavors to explore alternative methods facilitated by TANGO's unique framework. These methods aim to directly measure the velocity of emission plumes from concentration measurements, eliminating the dependency on uncertain meteorological data.

As this research unfolds, three key questions guide the investigations. The methodologies developed for each research question aim to provide comprehensive insights into the potential of TANGO's capabilities, the effectiveness of alternative methods, and the factors influencing uncertainty in emission rate estimates.

2.1. Research Question 1: How can the TANGO mission facilitate a framework for directly measuring the velocity of emission plumes from concentrations of CO2 and NO2?

Research Question 1 aims to investigate the capabilities of the TANGO mission in facilitating a framework for directly measuring the velocity of emission plumes based on concentrations of CO2 and NO2. This section outlines the methodology designed to address this question.

Simulation of TANGO Measurements

Due to the nature of the TANGO mission, it will be able to provide two images of the same emission plume, namely one image of the CO2 and one image of the NO2 concentrations within the plume. However, as mentioned in Section 1.3, information corresponding with the NO2 plume can be used to infer the complete CO2 plume using given ratios between CO2 and NO2 emissions in power plant emission plumes. As a result, it will be possible to extract two images from the same CO2 plume separated by some time difference which can be used to determine the CO2 emissions of the observed point source.

However, TANGO has yet to be launched, so to effectively answer the proposed research question, TANGO measurements must be simulated. Therefore, CO2 plumes from individual point sources will be simulated using Large Eddy Simulations (LES). These simulations take the global wind velocity, the image domain, and the emissions source rate as input. These inputs can be changed as their effect needs to be studied. From these CO2 plume simulations, two images from the same plume will be extracted which are separated by a certain Δt.

Thereafter, these two images can be used to directly measure the velocity of the emission plume.

Correlation Image Velocimetry
As discussed in Section 1.4, two promising methods in literature can be employed to track atmospheric features using satellite imagery. Firstly, the utilization of CIV involves processing two images of a simulated CO2 plume to derive a wind velocity field with a predetermined spatial resolution. However, challenges arise concerning the low SNR inherent to CO2 satellite imagery, the extended time intervals between stereo images, and the variability in feature sizes within emission plumes. A feasibility assessment of this algorithm will be conducted initially, followed by a discussion and motivation for the most optimal version.

CVision-CIV
Apart from CIV, Section 1.4 also mentioned the use of CVision to determine velocity fields. This technique has yet to be applied in atmospheric wind velocity estimation. However, while studies on CVision for velocity field determination show promise, challenges such as adapting machine learning networks to the relatively low SNR in satellite imagery, and addressing the need for extensive labeled datasets, remain to be addressed. To judge the effectiveness of a CVision-based approach within the framework that TANGO supplies, a CNN will be constructed that takes as input two images of CO2 plumes separated by a certain Δt, similarly to the CIV approach. The use of simulated plumes in supervised and unsupervised training in combination with transfer learning will provide insights into the performance of the CNN and its potential applicability to real TANGO measurements with unknown wind velocities.

2.2. Research Question 2: Can the direct measurement of the velocity of emissions plumes contribute to a more accurate estimation of emission source rates?

Research Question 2 focuses on assessing whether direct velocity measurements of emission plumes enhance the accuracy of emission rate estimations. Section 1.2 highlights studies relying on meteorological data for wind velocity in emission source rate estimation, despite its recognized inaccuracies. As an alternative, two methods leveraging direct wind velocity measurements from simulated satellite imagery have been developed in the methodology of Research Question 1. These methods will enable emissions source rate estimation to be performed without relying on uncertain meteorological data. The methodology is outlined as follows:

Quantification of Uncertainty in Direct Wind Velocity Measurements
To evaluate the suitability of direct wind velocity measurements for emission source rate estimation, a crucial step involves quantifying and comparing the uncertainties associated with these direct measurements against traditional meteorological data.

Propagation of Uncertainty into Emission Estimation Methods
This step investigates how the uncertainties of direct wind measurements influence emission estimation methods. Utilizing MBMs, emission source rates for simulated plumes will be estimated, enabling an assessment of the accuracy of these estimates. Additionally, the impact of unique characteristics in direct wind velocity measurements, such as spatial resolution, on emission source rate estimation will be examined.

2.3. Research Question 3: How can the mission or measurement parameters be optimized to enhance the accuracy of the estimation of emission source rates?

Research Question 3 aims to explore the optimization of mission measurement parameters to enhance the accuracy of emission rate estimations relying on wind velocity estimates obtained through CIV and CVision-CIV. This section outlines the methodology designed to address this question.

Uncertainty Analysis
The primary goal is to assess the effect of mission and measurement parameters on the uncertainty of direct mission measurements and emission source rate estimates. An iterative optimization process will be employed to identify the combinations of mission and measurement parameters that lead to enhanced accuracy in direct measurements and emission source

rate estimates. This iterative approach will allow for the refinement of parameter values based on the observed impact on uncertainty.

3

Methods and Results

3.1. Plume Simulation

To provide comprehensive answers to the research questions, it is necessary to simulate data similar to data generated by TANGO once operational in 2027. The real TANGO data will consist of high-resolution imagery of emission plumes worldwide. According to current specifications, the measurement instrument aboard TANGO will produce imagery with a resolution of 300m x 300m and a swath of 30km (Landgraf et al. (2020)). These images will capture CO2 and NO2 emission plumes separately. Since TANGO's launch is projected to be at least three years away, TANGO imagery is simulated for this study by numerically modeling turbulent atmospheric flow.

Several techniques and models can simulate turbulent atmospheric flow, including for example Direct Numerical Simulation and Large-Eddy Simulations (LES) (Piomelli (2014)). Due to the high Reynolds numbers typical of CO2 emission plumes (Re > 10000) and the computational cost of simulating atmospheric turbulence, LES was chosen for this study. LES offers significant advantages for simulating large Reynolds number flow regimes, particularly in atmospheric emission plumes where small-scale turbulence is less critical and complex geometries are not present. Unlike Direct Numerical Simulation, which resolves all turbulent scales and requires an extremely fine mesh, LES focuses on the larger turbulent structures and employs a subgrid scale model for the smaller, unresolved scales. This approach allows for a coarser mesh, which greatly reduces computational costs and makes it feasible to model large-scale atmospheric flows with current computing capabilities (Mason (1994), Piomelli (2014), Ardeshiri et al. (2020)). The open-source software MicroHH (Van Heerwaarden et al. (2017)) was chosen to perform these simulations. MicroHH's algorithm is based on governing equations related to the conservation of energy, momentum, and mass, incorporating boundary conditions. It can provide large 3D simulations of turbulent flow on length scales that match real-world observations containing compounds such as CO2 with specified characteristics, such as wind velocity, pressure gradients, diffusion coefficients, and grid resolution. This versatility makes it ideal for simulating emission plumes under various atmospheric and emissive conditions. Additionally, MicroHH can run on multiple processing cores in parallel, significantly reducing the running time required for simulations. For a detailed description of MicroHH's algorithm, the reader is referred to Van Heerwaarden et al. (2017) and the corresponding GitHub page, which includes the MicroHH license (MicroHH (2024)).

A simulation of emission plumes begins with defining input parameters and boundary conditions. MicroHH offers pre-defined cases of emission plumes from known power plants. For this study, the case corresponding to the Jänschwalde Power Plant Station in Germany was selected (MicroHH (2024)). The emission source is treated as a single scalar point source (Ražnjević et al. (2022)). For all simulations conducted in this thesis, the input parameters and boundary conditions remained constant, with the exception of wind speed in the horizontal direction and the emission rate. A comprehensive list of input parameters is provided in Appendix A.

The boundary conditions include no-slip and free-slip conditions at and away from the ground, respectively. Additionally, boundary conditions are imposed on the specific humidity flux and the surface heat flux both at and away from the ground. In the pre-defined Jänschwalde case, these parameters are time-dependent. However, for the simulations in this thesis, both the specific humidity flux and surface heat flux were kept constant over time to ensure that all simulations originated from similar conditions, enabling effective comparison of corresponding results.

For completeness, it is crucial to describe both the subgrid scale modeling and the discretization scheme utilized in the MicroHH LES solver. The solver employs the Smagorinsky-Lilly subgrid scale model (Lilly (1968)), which introduces a dynamic turbulence viscosity to account for the effects of unresolved small-scale turbulence. This model enhances the accuracy of LES by adjusting the turbulence model parameters dynamically throughout the simulation. MicroHH uses a staggered Arakawa C-grid configuration (Arakawa and Lamb (1977)). In this grid system, scalar quantities are located at the centers of the grid cells, while the velocity components are positioned at the corners and midpoints of the cell faces. The spatial discretization is executed using finite differences with second-order and fourth-order accuracy, ensuring consistency with the spatial resolution of the grid.

Each simulation was conducted to model the concentration distribution of a specified stable compound over a period of 16.5 hours. The simulations were performed on an orthogonal three-dimensional grid with dimensions 19.2 km×12.6 km×9.9 km in the x, y, and z directions respectively. In this coordinate system, the x direction aligns with the imposed wind velocity vector, the z direction is perpendicular to the ground, and the y direction is perpendicular to the wind velocity. This domain size is smaller than that of TANGO, as observable emission plumes do not extend to dimensions of 30 km. To enhance computational efficiency, the simulation grid is consequently reduced relative to TANGO's swath width, without compromising the overall representativeness of the results. Initially, the grid had a resolution of of 100 m × 100 m however if was reduced to a TANGO resolution of 300 m × 300 m using a Gaussian filter. . Snapshots of the concentration distribution were saved at 5-minute intervals.

To ensure that the concentration distribution was fully developed, only snapshots taken after 10 hours of simulation were selected for refinement. The refinement process takes a snapshot as the initial point and runs the simulation for 300 seconds, saving snapshots at 10-second intervals. The refined concentration distributions are transformed from a 3D concentration distribution to a 2D vertically integrated concentration distribution. The concentration values are then converted from CO2:air mixture ratios to parts per million (PPM) with respect to the total moles of air. These simulated concentration distributions are transformed into simulated emission plumes by adding the natural background concentration of the compound in the atmosphere. Finally, simulated measurement noise with level σ_{CO2} is added to the simulated emission plume using Equation 3.1 and Equation 3.2. A normal distribution ($\mathcal{N}$) is used for modeling the measurement noise of satellite imagery, as this noise is Gaussian (Landgraf et al. (2024)). The Gaussian noise propagates into the final concentration measurements in proportion to the magnitude of the measured concentration (Landgraf et al. (2024)).

$$\text{Noise}_{ij} \sim \mathcal{N}(0, \sigma_{CO2}) \tag{3.1}$$

$$\text{Noisy Image}_{ij} = \text{Image}_{ij} \cdot (\text{Noise}_{ij} + 1) \tag{3.2}$$

The final simulated product is a 2D image of emission plumes of a specific compound, with defined wind velocity, emission rate, and measurement noise level, at a 300m x 300m spatial and 10-second temporal resolution. For each simulated plume, the true 3D wind velocity field is extracted and vertically integrated, weighted by concentration, to create a 2D wind velocity field that matches the resolution and dimensions of the simulated plume. As a result, the true wind velocity is only defined in the 2D wind field at locations with nonzero concentration values. In the plume simulations, the wind velocity boundary condition is applied solely in the x direction (u), with no imposed component in the y direction (v). Consequently, the flow regime is dominated by u, although local turbulence induces nonzero values of v within the flow field. However, the contribution of v to the overall flow field is minimal, as its magnitude is, on average, more than 100 times smaller than that of u for all simulations. Therefore, the analysis of true and estimated wind velocity fields is focused exclusively on wind speeds in the x direction (u), disregarding the wind velocity component in the y direction (v).

This simulation process has been applied to create CO2 plumes at TANGO resolution using the output of MicroHH, with an added CO2 background concentration of 412 PPM to mimic the background CO2 concentration in the atmosphere (Pu et al. (2014)). The CO2 plumes are characterized by their wind velocity, emission rate, and simulated measurement noise. To match TANGO's data product, simulated NO2 plume imagery is also required, which originates from the same emission source as the CO2 plume. Additionally, the CO2 and NO2 plume images are spaced by a certain time difference, Δt, which accounts for the different overpass and imaging times of TANGO-Carbon and TANGO-Nitro. Conversion techniques proposed by Krol et al. (2024), motivated by the similar transport properties of and observed correlations between NO2 and CO2 emission plumes (Massman (1998), Hakkarainen et al. (2021)), enable noiseless CO2 plumes to be converted to NO2 plumes using CO2:NOX conversion ratios and NOX:NO2 conversion functions, a process displayed on the left side of Figure 3.2. CO2 concentration values are first converted into NOX concentration using the CO2:NOX conversion factor of 1/1.35 (Reuter et al. (2014), Kuhlmann et al. (2020)). Afterward, the CO2:NOX plume image is converted into a NO2 plume image using a decreasing exponential function that maps NOX concentration to NO2 concentration. This decreasing exponential function is the result of a fitted function to the NOX and NO2 plume simulations performed in Krol et al. (2024). It is a function of NOX concentration and distance from the emission source, enabling the function to accommodate for the natural decay rate of NOX in the Earth's atmosphere. It is applied to the NOX plume to create an NO2 plume which is augmented by artificial measurement noise with level σ_{NO2}. Figure 3.1 shows a CO2 plume and its corresponding NO2-converted-to-CO2 counterpart. The reader is referred to Appendix B for the precise NOX:NO2 function and the data representation used for fitting the function.

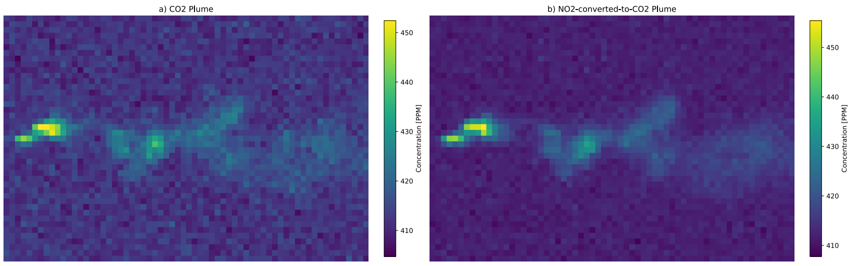

Figure 3.1: Simulated CO2 and NO2-converted-to-CO2 emissions plumes with a wind velocity of 6 m/s, emission rate of 25 MT/y and l_1 measurement noise.

The complete process, displayed in Figure 3.2, has been implemented to simulate NO2 plumes from noiseless simulated CO2 plumes originating from the same source. Thus, for every simulated CO2 plume, the corresponding NO2 plume is also determined and stored. These procedures have been used to create an extensive database, DB_{TANGO}, containing simulated CO2 and NO2 emission plumes which are spaced by a certain Δt and their corresponding velocity fields.

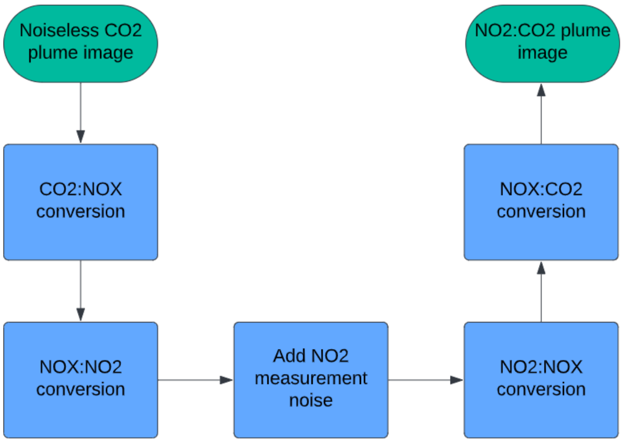

Figure 3.2: Flowchart representing the process that converts CO2 plume imagery into NO2 plume imagery which is used to create NO2-converted-to-CO2 plume imagery.

As discussed in Chapter 1, this thesis investigates the feasibility of estimating wind velocities and emission rates from TANGO's data product, which includes CO2 and NO2 plume imagery spaced by a certain Δt. Both proposed wind velocity estimation methods rely on image pairs of a plume spaced by Δt, where both images in the image pair capture the plume of the same compound. Consequently, TANGO's NO2 plume imagery must be converted back to CO2 plume imagery for use in these methods. The conversion method, which was initially used to simulate the NO2 plume image, is applied inversely to obtain these CO2 images, displayed on the right side of Figure 3.2. These NO2-converted-to-CO2 plumes are also stored in DB_{TANGO} for each entry.

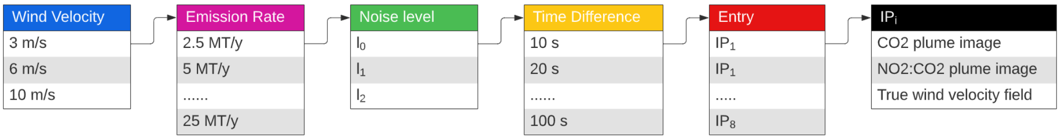

Figure 3.3: Data structure of DB_{TANGO}, comprised of CO2 and NO2-converted-to-CO2 plumes and wind velocity fields for a variety of wind velocities, emission rates, measurement noise levels and Δt's.

Figure 3.3 illustrates the structure of DB_{TANGO} and the various types of image pairs (IP_i) it contains. Each entry is categorized by wind velocity, emission rate, measurement noise level, and Δt. DB_{TANGO} includes three wind velocities ranging from 3 m/s to 10 m/s. Wind velocities below 3 m/s were excluded because these regimes are dominated by turbulent diffusion, which limits the accuracy of flow and emission rate estimation. Tracking features becomes difficult when mean displacements within the flow are overshadowed by the characteristic length scale of diffusion. Additionally, Varon et al. (2018) indicated that emission rate estimation methods are negatively affected when flows are dominated by diffusion rather than advection. Wind velocities above 10 m/s were also excluded, given their rarity in Earth's atmosphere (Ebuchi (1999) demonstrated that over 80% of observed winds have velocities lower than 10 m/s).

DB_{TANGO} comprises ten distinct emission rates ranging from 2.5 MT/y to 25 MT/y. Emission rates below 2.5 MT/y, the detection limit of TANGO-Carbon, were excluded. Similarly, emission rates above 25 MT/y were omitted due to the scarcity of power plants reaching or exceeding this emission rate (Guevara et al. (2023), Landgraf et al. (2024)). This thesis focuses on the use of simulated TANGO data to detect and image plumes corresponding to relatively small emission rates.

There are three different measurement noise levels in DB_{TANGO}: l_0=(0%, 0%), l_1=(0.5%, 0.25%), l_2=(1%, 0.5%), representing the simulated measurement noise level in the image pair. Even though TANGO's data-product will always be affected by some measurement noise, including the zero measurement noise case, l_0, is essential for clearly observing the contrast to the negative effects of nonzero measurement noise. Additionally, incorporating the zero noise cases allows for modeling biases to be easily detected without being dominated by the adverse effects of measurement noise. Each l_i consists of two elements: the measurement noise level added to the CO2 plume image, σ_{CO2}, and the measurement noise level added to the NO2 plume image before conversion to a CO2 image, σ_{NO2}. l_0 denotes the case where no measurement noise is added to either the CO2 or NO2 images. In this case, the NO2-converted-to-CO2 plume image and the original CO2 plume image are identical by definition of the conversion process shown in Figure 3.2. In contrast, for l_1 and l_2, this is not the case as the measurement noise added to the CO2 and NO2 plumes is independent. The measurement noise levels for the CO2 plume image are set at 0.5% and 1% to reflect the precision of TANGO-Carbon at the beginning and end of its operational life, respectively (Landgraf et al. (2024)). The same applies to the NO2 plume images for TANGO-Nitro but with measurement noise levels of 0.25% and 0.5%. This discrepancy in measurement noise levels of TANGO-Carbon and TANGO-Nitro is primarily attributed to the differing atmospheric conditions at the respective measurement wavelengths. TANGO-Carbon operates in the near-infrared (1.6 μm), while TANGO-Nitro utilizes the ultraviolet/visible (440 nm) spectrum. The shorter wavelength of TANGO-Nitro benefits from a higher incoming solar irradiance due to the solar spectrum's peak around 500-600 nm. Additionally, Rayleigh scattering (Bates (1984)) and aerosol scattering (Moosmüller et al. (2009)) are more pronounced in the ultraviolet/visible, leading to a brighter atmospheric signal. A stronger signal generally corresponds to a lower relative noise level. The retrieval process also influences measurement noise levels. Weaker absorption typically results in higher noise in the retrieved concentration measurements (Boersma et al. (2004), Saitoh et al. (2009)). While this favors the relative precision of CO2 retrieval over NO2 retrieval, the combined effects of higher solar irradiance, scattering, and lower inherent noise in the NO2 measurements ultimately lead to a lower overall noise level for NO2 concentration measurements (approximately half of measurement noise levels in CO2 concentrations measurements) compared to CO2 concentration measurements (Landgraf et al. (2024), Reuter et al. (2019), Kuhlmann et al. (2020)).

Finally, Δt varies from 10 s to 100 s in 10 s increments. Larger Δt values were excluded due to the limitations of the TANGO mission (Landgraf et al. (2024)). For each combination of wind velocity, emission rate, measurement noise level, and Δt, DB_{TANGO} includes 8 different image pairs and simulated wind velocity fields. Consequently, DB_{TANGO} comprises a total of 7,200 image pairs.

In DB_{TANGO}, variations in wind velocity, emission rate, and measurement noise level significantly impact the concentration values in both the CO2 plume and the NO2-converted-to-CO2 plume images. Increased wind velocity results in more dispersed emissions and lower peak concentrations, whereas lower wind velocities lead to more concentrated emissions. Higher emission rates correspond to elevated concentration values throughout the plume, while lower emission rates produce the opposite effect. The introduction of measurement noise affects concentration values across the entire plume, diminishing the clarity of the plume image.

These effects are quantified by the Signal-to-Noise Ratio (SNR), a single metric commonly used in signal analysis. The SNR represents the clarity and quality of a signal by comparing the level of the desired signal to the level of background noise. In the context of emission plume measurements, a higher SNR indicates that concentration variations are more distinct and easily detectable against the inherent variability of the measurement process. Essentially, a higher SNR signifies more reliable and accurate measurements, where the true signal stands out prominently from the measurement noise. As is discussed in subsequent sections, the SNR of imagery determines its usability in estimation methods relying on this imagery. A clear quantification of the different SNR values in DB_{TANGO} is presented in Appendix E, which will enable a comprehensive interpretation of results in subsequent sections.

3.2. Correlation Image Velocimetry

3.2.1. The CIV Algorithm

From DB_{TANGO}, an image pair comprising a CO2 plume image and a NO2-converted-to-CO2 plume image for a given wind velocity, emission rate, measurement noise level, and Δt can serve as input to the method that applies CIV. The CIV Algorithm relies on the same cross-correlation technique discussed in Section 1.4.1. For a given pixel location and a specified interrogation window size (IWS), two interrogation windows (IW) are extracted: $I \in \mathbb{R}^{N \times N}$ from the first image in the image pair and $I' \in \mathbb{R}^{M \times M}$ from the second image in the image pair, where I' is twice the size of I ($2N = M$). Example interrogation window extraction is displayed in Figure 3.4

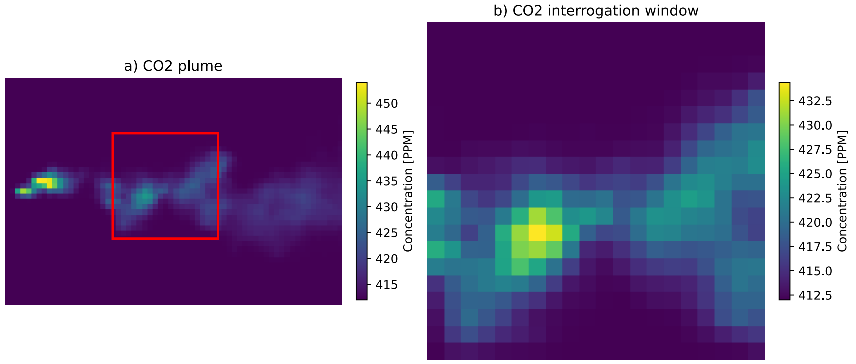

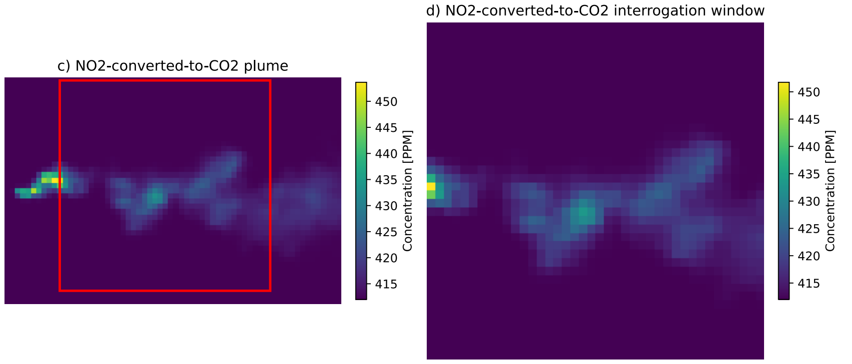

Figure 3.4: CO2 and NO2-converted-to-CO2 plume imagery (left column) from which two IW are extracted, indicated by the red squares. These IW are displayed in the right column. The CO2 and NO2-converted-to-CO2 plumes have a Δt of 100 s, 25MT/y emission rate and are noiseless.

For a possible pixel shift (x, y), representing a displacement between the centers of I and I' over Δt, Equation 1.3, 1.4, 1.5, and 1.6 are applied to compute the normalized cross-correlation between the two IW. This shift enables systematic comparison across a range of pixel shifts $(-N \leq x \leq N, -N \leq y \leq N)$, generating a two-dimensional cross-correlation map (CCM). Here, I is shifted within I' without overlapping its edges. At positions where the patterns within I and I' align, the value of the cross-correlation between I and I' is high. The position of the peak cross-correlation magnitude in the cross-correlation map reflects the average spatial displacement of I' relative to I over the time interval Δt, from which an estimate of the local velocity is obtained. The CCM created from the cross-correlation of the IW from Figure 3.4 is displayed in Figure 3.5

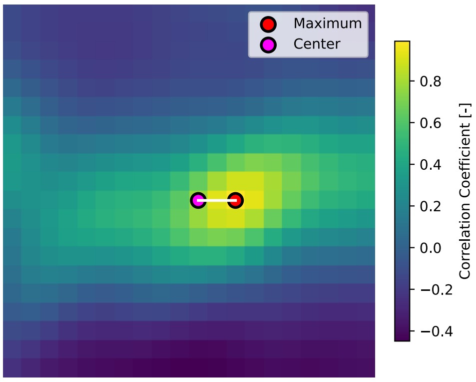

Figure 3.5: The CCM of the IW displayed in Figure 3.4. The red dot indicates the location of the peak of the CCM. The magenta dot indicates the center of the CCM. The white vector from the center to the peak indicated the estimated displacement vector.

Once the CCM is obtained, the peak location is extracted to infer the displacement vector, limited initially to integral values. In Figure 3.5, this peak is located by the red-colored dot. The white vector from the magenta-colored dot (the center of the CCM) to the red-colored dot indicates the estimated displacement vector, which is estimated in integral values. However, leveraging the CCM and its values allows for estimating the peak location with sub-pixel accuracy. A common method involves fitting a function to points surrounding the peak within the CCM, known as its neighborhood, and locating the peak of the fitted function.

In PIV applications, particle images are typically described by an Airy intensity distribution which is accurately approximated by a Gaussian intensity distribution (Raffel et al. (2018)). Due to the properties of a Gaussian distribution, the correlation of two Gaussian intensity distributions results in a Gaussian distribution again. Therefore, neighborhood peaks in PIV applications are accurately estimated by Gaussian functions to estimate sub-pixel displacements. Depending on the shape of the CCM and the clearness of the peak, an optimal neighborhood size is selected, which is at least a 3x3 by region surrounding and including the CCM peak (Raffel et al. (2018)).

The CIV algorithm implemented in this thesis employs a similar procedure to estimate sub-pixel peak locations. A 2D Gaussian function (shown in Equation 3.3) is fitted to the peak neighborhood. The parameters (μ_x, μ_y) of the Gaussian function represent the estimated peak location at sub-pixel accuracy. Subsequently, this sub-pixel peak location estimate (μ_x, μ_y) is converted into a wind velocity using the image resolution and Δt between the image pair. This process outlines how the CIV Algorithm estimates the wind velocity for a selected pixel location given an IWS. To estimate a wind velocity field, this procedure iterates over each pixel location and estimates its corresponding wind velocity.

$$f(x,y) = \frac{1}{2\pi\sigma_x\sigma_y}\exp\left(-\frac{(x-\mu_x)^2}{2\sigma_x^2} - \frac{(y-\mu_y)^2}{2\sigma_y^2}\right) \tag{3.3}$$

To evaluate the validity of the Gaussian approximation of the peak and its sensitivity to neighborhood size, an analysis was performed on the CCMs of 50 randomly selected pixel locations from the image pair displayed in Figure 3.4, with the IWS fixed at 12 pixels. For all pixel locations, the peak of the Gaussian approximation is expected to be located at coordinates (8,6), corresponding to an anticipated pixel shift of (2,0). This shift reflects a displacement of 600 meters in the x-direction between the two IW, given a wind velocity of 6 m/s and a time interval (Δt) of 100 seconds, as illustrated in Figure 3.4. Deviations from this expected peak location may occur due to discrepancies between the imposed and true wind velocities, resulting from the turbulent nature of the flow. Additional deviations could also arise from the limited accuracy of the Gaussian approximation of the CCM peak. By analyzing the discrepancies between the expected and estimated peak locations across different neighborhood sizes, the accuracy of the Gaussian approximation can be evaluated as a function of peak neighborhood size.

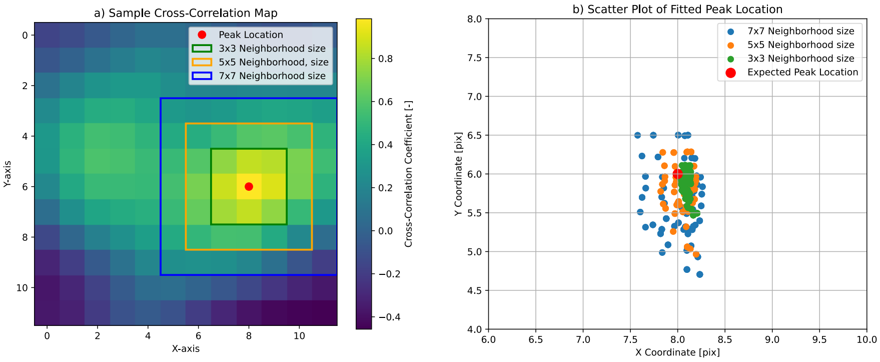

Figure 3.6: Plot (a) displays a sample CCM selected for one of the 50 arbitrary pixel locations from the image pair in Figure 3.4 for which the CCM was computed. The colored rectangles indicate the different peak neighborhoods used in the peak fitting procedure. Plot (b) displays the peak location estimated by the Gaussian fitting procedure for different peak neighborhood sizes.

The impact of neighborhood size on the accuracy of peak location estimation is illustrated in plot (b) in Figure 3.6. As the neighborhood size increases, the accuracy of the Gaussian approximation for the peak's neighborhood decreases significantly, seen in an increased deviation from the expected peak location. This is expected as the intensity distribution in the simulated plume imagery does not necessarily follow an Airy intensity distribution and cannot be as accurately approximated by a Gaussian distribution. As the neighborhood size increases, this discrepancy becomes more profound. To mitigate the adverse effects of approximating the peak neighborhood with a Gaussian distribution, a minimal neighborhood size is employed in the CIV Algorithm. Specifically, the neighborhood consists of 9 points arranged in a 3x3 grid centered on the integral peak location.

As detailed in Section 1.4.1, the IWS significantly impacts the shape of the CCM. Interrogation windows that are too small often result in a low SNR, leading to a less distinct CCM peak. Conversely, excessively large IW can include displacement gradients, which obscure the CCM peak. Therefore, careful selection of the IWS is crucial for the proper application of the CIV Algorithm. These factors (SNR and displacement gradients) not only alter the peak shape but also affect the quality of peak fitting. The quality of the peak fit is determined by computing the sum of squared residuals (SSR) of the fitting Gaussian function to the peak neighborhood. Figure 3.7 illustrates the expected qualitative and observed impacts of SNR and displacement gradients on the peak and quality of its fit as IWS varies.

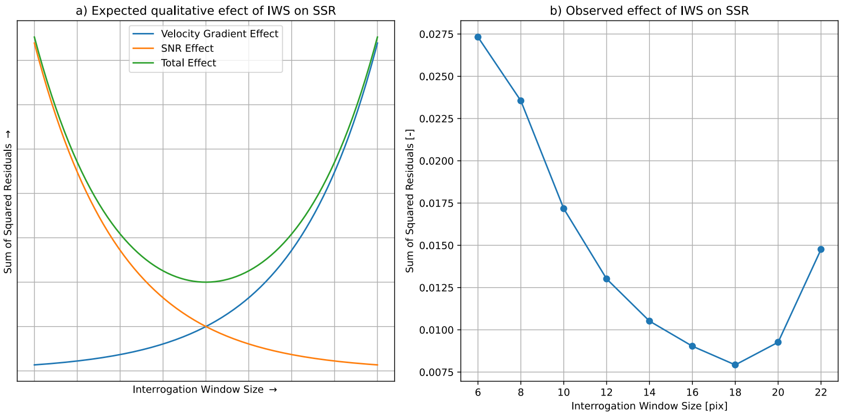

Figure 3.7: Plot (a) illustrates the expected qualitative effects of SNR (orange line) and displacement gradients (blue line) on the quality of peak fitting (SSR) as the IWS increases. The green line represents the combined expected qualitative impact of SNR and displacement gradients on peak fitting quality. Plot (b) shows the observed trend (which holds for all pixel locations) in peak fitting quality (SSR) as the IWS increases for an arbitrarily selected pixel location from the image pair shown in Figure 3.4.

Plot (a) in Figure 3.7 illustrates the expectation that as IWS increases and the SNR of the interrogation window increases, the expected qualitative clearness and the quality of the peak fit increases. However as the IWS increases, the presence of displacement gradients in the interrogation window is expected to start to dominate and the expected qualitative clearness and the quality of the peak fit decreases. Due to these opposing effects of SNR and displacement gradients, the aggregated effect of them both dictates the IWS with the maximal fitting quality. These expected effects are indeed also observed in the calculation from numerical data in plot (b) in Figure 3.7 where the quality of the peak fit initially increases as IWS increases (SNR effect dominates), however as it crosses an IWS of 16 pixels, the quality of the peak fit decreases again (velocity effect dominates).

This observed behavior of the SSR across varying IWS can be leveraged to gain insights into optimal IWS selection. Namely, given the nature of the imagery used in this thesis and the broad, non-Gaussian CCM peak it produces, the most accurate displacement estimates are expected to result from peak fitting procedures that have the lowest SSR. Consequently, SSR serves as a proxy for the accuracy of displacement estimates, and the IWS is optimized to achieve the highest quality fitting procedure, specifically by minimizing SSR.

In PIV and CIV literature, the IWS is typically constant for all pixel locations within a single iteration of an algorithm. However, constant IWS across all pixel locations in an emission plume is disadvantageous due to the varying concentration levels and stationary nature of emission sources. Pixel locations near the emission source exhibit higher concentrations, but the variation in the signal is diminished due to the constant emission rate and the scale of the image resolution. This loss of detail necessitates larger IWS to effectively capture displacement. Conversely, pixel locations farther from the source display greater variability at larger length scales, allowing for smaller IWS to be effective. Therefore, each pixel locations, depending on its proximity to the emission source, benefits from a different optimal IWS tailored to maximize the quality of peak neighborhood fitting. The IWS that maximizes the quality of peak neighborhood fitting is selected as the optimal IWS for that pixel location.

To estimate a comprehensive wind velocity field, the CIV Algorithm aims to estimate wind velocities for all pixel locations in each image pair. However, this approach has limitations. Pixels with high concentrations typically exhibit higher SNR, leading to clearer CCM peaks and more accurate wind velocity estimates. In contrast, pixel locations with low concentrations and lower SNR tend to produce less distinct CCM peaks, resulting in less accurate wind velocity estimates. Moreover, the CIV Algorithm cannot effectively estimate wind velocity for pixel locations near the image boundary where IW extraction is impractical. To address these issues, a subset of pixel locations, l_p, is extracted from the first image in the image pair, where wind velocity estimation is reliable and boundary effects are minimized. Pixel locations are included in l_p if their concentration exceeds a threshold t_p. Careful selection of t_p is essential as it significantly influences the CIV Algorithm's inputs and outputs.

Since concentration values vary between plumes with different emission rates, maintaining a constant t_p is impractical. A fixed t_p would bias selection towards pixel locations in high-emission rate plumes, potentially skewing the analysis. This bias is illustrated in Figure 3.8, where significant differences in pixel location selection are evident between plumes with emission rates of 10 MT/y and 25 MT/y (plots (c) and (f) respectively).

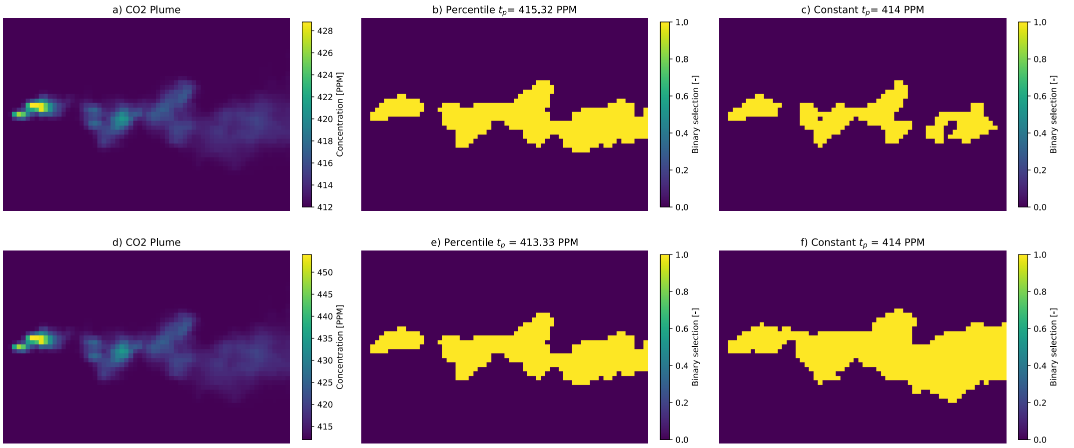

Figure 3.8: Imagery of two simulated CO2 plumes for an emission rate of 10 (plot (a)) and 25 MT/y (plot (d)) are displayed. Plots (b) and (e) display the results on percentile thresholding and plots (c) and (f) display the effects of constant thresholding, where for plots (b),(c),(e), and (f), pixel locations not in l_p have value 0 (blue color), while pixel locations in l_p are have value 1 (yellow color).

To address this issue, t_p needs to be dependent on the CO2 plume itself. A histogram is created for the first image in the image pair, and t_p is set to the value of the 85$^{\text{th}}$ percentile. This approach ensures that t_p can vary according to the distribution of concentration values within a simulated plume, leading to similar pixel location selection between plumes with differing emission rates observed in plots (b) and (e) in Figure 3.8.

Since the selection of pixel locations in l_p is dependent on the concentration value of the pixel and not IWS, the significant overlap of IW of different pixel locations is highly present. Typically, obtaining an independent velocity vector of a flow is striven for in PIV and CIV applications (Raffel et al. (2018)), however, the nature of TANGO data limits this. Due to TANGO's resolution of 300m x 300m and finite swath width, the number of pixel locations and the image domain are constrained to a significant degree. The number of pixel locations in the plume for which the wind velocity can be independently estimated is simply too low. Furthermore, due to the inherently low SNR of CO2 plume imagery, pixel locations typically necessitate relatively large IWS (up to 30 pixels) to mitigate its impact on wind velocity estimates. As a result, the wind velocity vectors of the pixel locations in l_p are highly correlated and therefore create a smoothed wind velocity field. In typical PIV applications, such smoothing is undesirable because it can obscure detailed flow structures and is inappropriate for calculating turbulent statistics or flow velocity gradients. However, this thesis is not concerned with calculating turbulent statistics or velocity gradients. Instead, the goal in this thesis is to obtain the most locally accurate velocity vectors possible, given the available data. Therefore, an appropriate IWS is chosen to ensure the best estimate of wind velocity at each pixel location, rendering the overlap of IW irrelevant.

3.2.2. Wind Velocity Estimation Results

The CIV Algorithm provides wind velocity fields as output, consisting of wind velocities for pixel locations in l_p. These wind velocity fields include both horizontal and vertical components (u and v) of the wind velocity. However, due to the nature and alignment of the plume simulation, the v component of the estimated wind velocity is negligibly small and is therefore omitted from the analysis. To assess the accuracy of the wind velocity estimates, a comparison is made with the true wind velocities of each pixel location extracted from the CO2 plume simulations. To gain insight into the nature and characteristics of the CIV Algorithm's output, an arbitrary image pair is selected from DB_{TANGO} for which the wind velocity field is estimated.

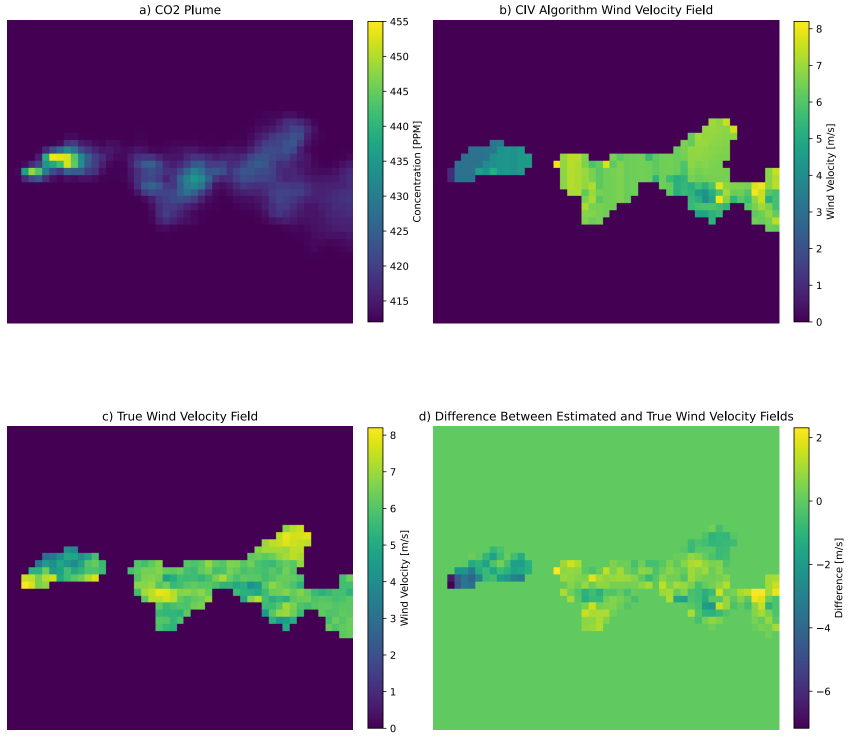

Figure 3.9: The first CO2 plume image in the image pair is displayed in plot (a). The resulting wind velocity field estimated by the CIV Algorithm is displayed in plot (b). For reference, the true wind velocity field filtered for pixel locations in l_p and the difference between the estimated and true wind velocity fields are displayed in plots (c) and (d) respectively. The plume characteristics included a true wind velocity of 6 m/s, an emission rate of 25 MT/y, a l_0 measurement noise level and a Δt of 50 seconds.

Figure 3.9 displays the first image in the image pair that was arbitrarily selected (plot (a)), along with the corresponding estimated wind velocity field (plot (b)). Note that all pixels marked with a nonzero wind velocity in plots (b) and (c) correspond to those pixel locations in l_p. It is observed that there does exist variation within the wind velocity field, however, the wind velocity field is greatly smoothed in comparison with the true wind velocity field (plot (c)). In the estimated wind velocity field, a clear relationship is observed between the distance of pixel locations to the emission source and the degree of wind velocity underestimation. This relationship is further illustrated in Figure 3.10.

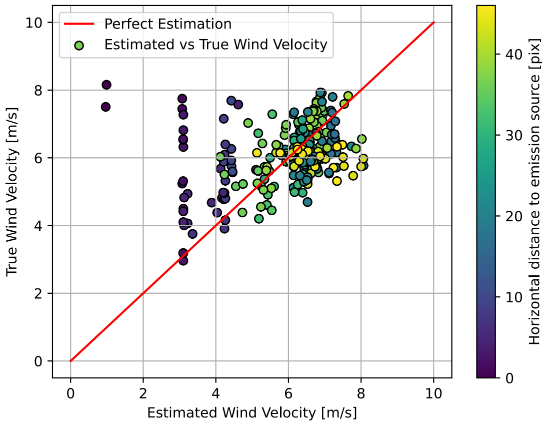

Figure 3.10: Accuracy plot of the wind velocity field estimated by the CIV Algorithm displayed in Figure 3.9. For perfect estimation, all points in the scatter plot lie on the red diagonal line. The scatter plot is color-coded with the horizontal distance from the emission source.

Figure 3.10 shows a scatter plot mapping the estimated wind velocity field to the true wind velocity field. Ideally, with perfect estimation and zero error, all points would lie on the red diagonal line. Deviation from this line indicates an estimation error. It is evident that there is a significant estimation error across the entire wind velocity field since for all distances to the emission source, deviations from the diagonal red line are observed. However, as the distance to the emission source decreases, the greatest estimation errors are observed.

A notable phenomenon, also observed in Figure 3.9, is the clear underestimation of wind velocity for pixel locations near the source. The two points plotted in the top left of Figure 3.10 correspond to the pixel locations closest to the source. Additionally, a distinct vertical line at 3.2 m/s estimated wind velocity represents pixel locations in the region near the emission source. This alignment on the 3.2 m/s vertical line corresponds to the average wind velocity of the left-most blob in plot (b) of Figure 3.10, adjusted for the bias introduced by including the emission source in the IW. This pattern of underestimation is attributed to the operating principle of the CIV Algorithm, which tracks moving features in the plume's concentration distribution. Features with higher concentration values relative to the rest of the plume are given more weight in the tracking process. Pixel locations near the source usually exhibit the highest concentration values but contain fewer traceable features due to the limited diffusion of emissions. The CIV Algorithm assigns substantial weight to these high-concentration pixel locations near the source, which appear stationary due to the constant emission rate. Consequently, the CIV Algorithm underestimates the wind velocity of pixel locations closer to the emission source.

To further evaluate the accuracy of the CIV Algorithm wind velocity estimates, it is essential to analyze results from emission plumes with varying characteristics effectively without manually reviewing figures such as Figure 3.9 and Figure 3.10. Therefore, the accuracy of the estimated wind velocity is assessed using the *Root Mean Squared Error* (RMSE) and the *Mean Error* (ME).

The RMSE provides a measure of the differences between the estimated wind velocity (u) and the true wind velocity ($\hat{u}$) extracted from DB_{TANGO}. Mathematically, RMSE is defined as the square root of the average of the squared differences between u and $\hat{u}$. If i ranges from 1 to $|l_p|$ (the total number of selected pixel locations in the plume for which the wind velocity is estimated), the formula for RMSE is given by Equation 3.4.

$$\text{RMSE} = \sqrt{\frac{1}{|l_p|}\sum_{i \in l_p}(\hat{u}_i - u_i)^2} \qquad \text{in [m/s]} \tag{3.4}$$

The RMSE is a useful metric because it gives a sense of the magnitude of the errors in the same units as the original data. Lower values of RMSE indicate a better fit of the estimated wind velocity to the true wind velocity. Additionally, the RMSE represents the spread of errors, providing an overall measure of the accuracy and consistency of the wind velocity estimates.

On the other hand, the ME is a simpler metric that calculates the average of the differences between the estimated wind velocity (u) and the true wind velocity ($\hat{u}$). The ME is defined in Equation 3.5.

$$\text{ME} = \frac{1}{|l_p|}\sum_{i \in l_p}(u_i - \hat{u}_i) \qquad \text{in [m/s]} \tag{3.5}$$

The ME provides a measure of the bias in the estimates. A positive ME indicates an overestimation, whereas a negative ME indicates an underestimation of the wind velocity. By analyzing the ME, one can detect systematic biases in the wind velocity estimates. Throughout the remainder of this thesis, the terms bias and ME are used interchangeably.

To effectively analyze the results and accuracy of the CIV algorithm across all different combinations of plume characteristics, the input is upscaled from a single plume to several image pairs per combination of plume characteristics. This involves selecting a diverse subset of DB_{TANGO}, called DB_{test}, that encompasses different wind velocities, emission rates, measurement noise levels, and Δt's. Each combination of these parameters is represented in

DB_{test} by four distinct image pairs. Then, for each image pair among the four image pairs that belong to the same combination of plume characteristics, the RMSE and ME of the velocity field are computed. Once all four RMSEs and MEs have been computed, they are averaged and stored as the average RMSE and average ME for that combination of wind velocity, emission rate, measurement noise level, and Δt, respectively. This averaging procedure limits the effect of outliers in any performance metrics which enables reliable analysis.

The value of Δt significantly influences the results of the CIV Algorithm as it determines the magnitude of the displacement between image pairs. Larger Δt values and the resulting larger displacements reduce the random error relative to the displacements, whereas smaller Δt values and the resulting smaller displacements increase the random error relative to the displacements (Raffel et al. (2018)). To account for this effect of Δt on the performance of the CIV Algorithm, two distinct Δt scenarios are analyzed.

Firstly, the variable Δt scenario is analyzed, where the displacement for different wind velocities is constant. Δt varies from 100, 50, and 30 seconds for wind velocities of 3, 6, and 10 m/s, respectively, such that the displacement in all cases is 300 meters. Since the displacement of emission plumes remains constant across all wind velocities, the contribution of random error is constant for all different wind velocities and the performance of the CIV Algorithm can effectively be compared between different wind velocities.

Unfortunately, the TANGO mission does not offer the luxury of varying Δt depending on wind velocity. Instead, Δt is fixed and constant for all emission plumes observed by TANGO. In a scenario with constant Δt, the displacements of emission plumes vary based on wind velocity. For example, with a constant Δt of 20 seconds, a wind velocity of 3 m/s results in a displacement of 60 meters, while a wind velocity of 10 m/s results in a displacement of 200 meters. As previously indicated, the relative contribution of random error increases as displacements grow smaller. Thus, for a displacement of 60 meters, this relative contribution is larger than for a displacement of 200 meters. Due to this effect, the scenario with constant Δt is analyzed separately from the variable Δt scenario.

Scenario: Variable Δt

Firstly, the average RMSE and ME results of the CIV Algorithm are analyzed for a variable Δt. For a Δt of 100, 50, and 30 seconds, for wind velocities of 3, 6, and 10 m/s respectively, the displacement between the image pair is 300 meters in all three cases. As a result, the contribution of random error to the results of the CIV Algorithm is constant relative to the displacement, enabling effective analysis and comparison across estimated wind velocity fields for different combinations of plume characteristics.

Table C.1 in Appendix C presents the average RMSE values across different combinations of wind velocities, emission rates, measurement noise levels, and Δt for the CIV Algorithm. Each cell in the table represents the average RMSE computed from four image pairs per combination. Similarly, Table C.2 in Appendix C displayed the average ME values for the same combinations. These tables provide a comprehensive overview of the performance of the CIV Algorithm in estimating wind velocities under varying conditions.

In Figure 3.11, the performance of the CIV Algorithm is visually represented through plots of average RMSE and ME values. Each average RMSE and ME displayed in Figure 3.11 corresponds to a specific combination of wind velocity, emission rate, measurement noise level, and Δt. This visualization helps to identify trends and outliers in the wind velocity field estimation errors across different combinations of plume characteristics. Each average RMSE and ME value is complemented by an error bar representing the standard deviation of the average RMSE and ME, respectively. This standard deviation is determined from the performance of the CIV Algorithm across all four plumes corresponding to the same combination of plume characteristics.

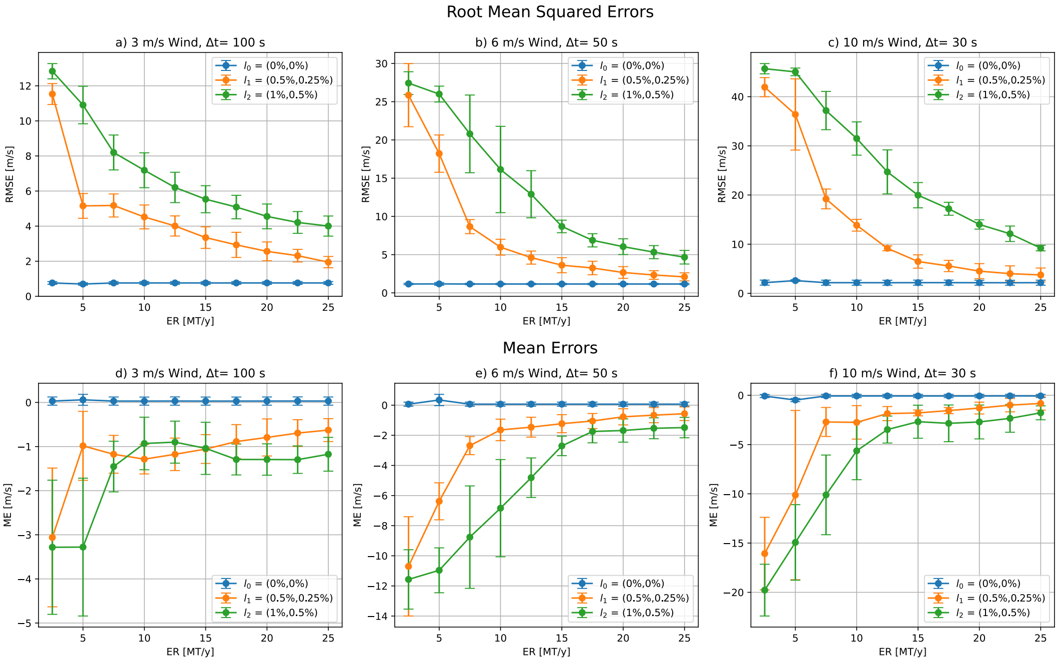

Figure 3.11: Plot (a) and (d) display the average RMSE and ME, respectively, for a Δt of 100 s, a wind velocity of 3 m/s and varying emission rates (ER) and measurement noise levels. Plot (b) and (e) display the average RMSE and ME for a Δt of 50 s, a wind velocity of 6 m/s and varying emission rates (ER) and measurement noise levels. Plot (c) and (f) display the average RMSE and ME for a Δt of 30 s, a wind velocity of 10 m/s and varying emission rates (ER) and measurement noise levels. All plots are complemented by a single standard deviation error-bar of the average RMSE and ME values.

The results for the CIV Algorithm are summarized in Figure 3.11, which illustrates the average RMSE and ME in the wind velocity fields estimated by the CIV Algorithm. The emission rate of the plume, given in megatons per year (MT/y), is plotted on the x-axis, while three different measurement noise levels (l_0, l_1, and l_2) are represented by different colors in each plot. The plots differentiate between three wind velocities: 3 m/s (plots (a) and (d)), 6 m/s (plots (b) and (e)), and 10 m/s (plots (c) and (f)).

At a wind velocity of 3 m/s, the measurement noise level l_0 maintains consistently low average RMSE values around 0.76 m/s, indicating minimal error. In contrast, measurement noise level l_1 starts with a high average RMSE of approximately 11 m/s at lower emission rates, but this decreases significantly to around 1.9 m/s as emission rates increase. Measurement noise level l_2 also starts with a very high average RMSE of about 12 m/s, which steeply decreases to approximately 4 m/s with higher emission rates.

At a 6 m/s wind velocity, measurement noise level l_0 continues to show low average RMSE values, averaging around 1.19 m/s. For measurement noise level l_1, the average RMSE starts high at around 25 m/s at low emission rates and decreases to about 2 m/s as emission rates increase. Measurement noise level l_2 exhibits a similar trend, starting with a high average RMSE of approximately 27 m/s and decreasing to around 2 m/s with increasing emission rates.

For a wind velocity of 10 m/s, measurement noise level l_0 maintains low average RMSE values around 2 m/s, indicating minimal error. Measurement noise level l_1 begins with a very high average RMSE of approximately 41 m/s at lower emission rates and decreases to around 3.7 m/s as emission rates rise. Measurement noise level l_2 starts with an extremely high average RMSE of about 45 m/s, which decreases to approximately 9 m/s with increasing emission rates.

These observations highlight the significant variation in average RMSE across different plume characteristics. For scenarios with measurement noise level l_0 and the highest emission rates, RMSE averages around 20% of the true wind velocity. Conversely, with measurement noise level l_2 and the lowest emission rates (indicating the lowest SNR), average RMSE can spike to around 400% of the true wind velocity. This underscores the critical impact of SNR on wind estimation accuracy. Additionally, in scenarios with nonzero measurement noise (l_1 and l_2), increasing emission rates improve the SNR in the emission plume imagery, leading to decreased average RMSE. This increase in contrast against background concentrations aids the CIV Algorithm in providing more accurate wind velocity estimates.

When there is zero measurement noise (l_0), a significant average RMSE is observed that increases non-linearly with true wind velocity. This increase is attributed to the effects of turbulent mixing and displacement gradients in the plumes. As true wind velocity increases, so does the amount of turbulent mixing, due to the higher Reynolds number, which affects the traceability of features across image pairs. Additionally, displacement gradients, which are constant relative to the true wind velocity, are affected by changes in wind velocity.

The average ME results, as shown in Figure 3.11 for a 3 m/s wind velocity, reveal that measurement noise level l_0 maintains low and stable average ME values, indicating minor deviations from actual wind velocities. Measurement noise level l_1 starts with a large average ME of approximately -3 m/s at low emission rates but increases to around -0.6 m/s as emission rates increase. Measurement noise level l_2 shows an initial large average ME of about -3.2 m/s, which increases steeply to converge at -1.1 m/s with increasing emission rates.

At a 6 m/s wind velocity, measurement noise level l_0 maintains low and stable average ME values, showing minimal deviations from actual wind velocities. Measurement noise level l_1 starts with a large average ME of around -10 m/s at low emission rates and increases to about -0.5 m/s as emission rates rise. Measurement noise level l_2 begins with a large average ME of approximately -11 m/s and increases steeply to converge at -1.5 m/s with increasing emission rates.

For a wind velocity of 10 m/s, measurement noise level l_0 continues to show low and stable average ME values. Measurement noise level l_1 starts with a large average ME of approximately -16 m/s at lower emission rates but increases to about -0.8 m/s as emission rates rise. Measurement noise level l_2 shows an initial very large average ME of about -20 m/s, which increases steeply to approximately -1.7 m/s with increasing emission rates.

Overall, the results indicate that changes in measurement noise levels, wind velocities, and emission rates lead to varying SNRs, which significantly affect bias. Higher SNR generally results in lower bias, whereas introducing measurement noise amplifies bias, particularly in scenarios with inherently lower SNR. For instance, at a low SNR with a 10 m/s wind velocity and 2.5 MT/y plumes, bias is significantly larger compared to higher SNR scenarios at 3 m/s and 25 MT/y plumes. Specifically, at measurement noise level l_2, bias at 10 m/s and 2.5 MT/y is approximately 100 times larger than at l_0, whereas bias at l_2 for 3 m/s and 25 MT/y is only about four times larger than at l_0. This disparity highlights the pivotal role of SNR in bias amplification. Furthermore, the increasing trends observed in the orange and green lines in plots (d), (e), and (f) for increasing emission rates confirm the effect of SNR. As emission rates increase and measurement noise is introduced at fixed levels, the SNR improves, reducing absolute bias. When the CIV Algorithm is exposed to relatively low SNR imagery, it tends to significantly underestimate wind velocity fields, with biases exceeding -200% relative to the true wind velocity. These findings underscore the critical importance of high SNR inputs for accurate wind velocity estimation using the CIV Algorithm. Higher SNR leads to more accurate estimates, while lower SNR results in significant inaccuracies.

Scenario: Constant Δt

Secondly, the average RMSE and ME of the CIV Algorithm are analyzed for all combinations of plume characteristics with a constant Δt of 20 seconds, mimicking the data product of TANGO. These results are displayed in Appendix C in Table C.3 and Table C.4, respectively, and plotted in Figure 3.12. Each average RMSE and ME value in Figure 3.12 is again complemented by an error bar representing the standard deviation of the average RMSE and ME, respectively.

For a Δt of 20 seconds, the displacement between the image pairs in not constant but a function of the wind velocity. For wind velocities of 3, 6, and 10 m/s, displacements between image pairs are 60, 120, and 200 meters (all sub-pixel displacements), respectively. Due to this variability of displacements, the relative contribution of random error is no longer constant over plumes with different wind velocities. Therefore, an increased relative estimation error is expected to arise for combinations of plume characteristics with relatively smaller displacements, and vice versa for larger displacements.

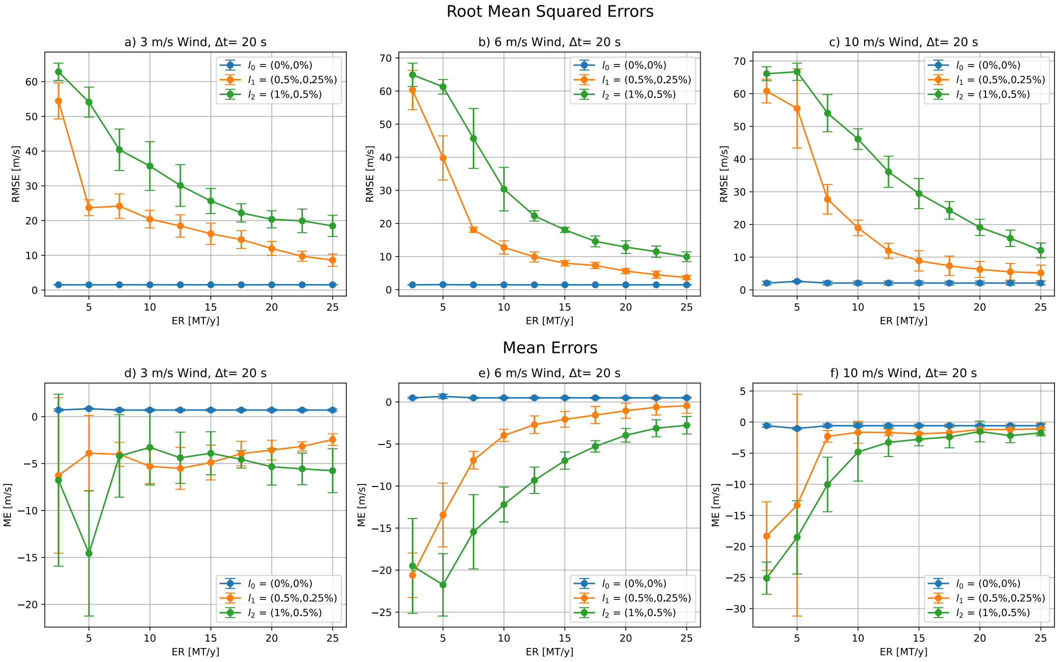

Figure 3.12: Plot (a) and (d) display the average RMSE and ME, respectively, for a Δt of 20 s, a wind velocity of 3 m/s and varying emission rates (ER) and measurement noise levels. Plot (b) and (e) display the average RMSE and ME for a Δt of 20 s, a wind velocity of 6 m/s and varying emission rates (ER) and measurement noise levels. Plot (c) and (f) display the average RMSE and ME for a Δt of 20 s, a wind velocity of 10 m/s and varying emission rates (ER) and measurement noise levels. All plots are complemented by a single standard deviation error-bar of the average RMSE and ME values.

The results for the CIV Algorithm with a constant Δt of 20 s are summarized in Figure 3.12. This figure illustrates the average RMSE and ME in the wind velocity fields estimated by the CIV Algorithm. The emission rate of the plume, given in megatons per year (MT/y), is plotted on the x-axis, while three different measurement noise levels (l_0, l_1, and l_2) are represented by different colors in each plot. The plots differentiate between three wind velocities: 3 m/s (plots (a) and (d)), 6 m/s (plots (b) and (e)), and 10 m/s (plots (c) and (f)).

At a wind velocity of 3 m/s, measurement noise level l_0 maintains consistent average RMSE values around 1.5 m/s. For measurement noise level l_1, average RMSE starts very high at approximately 54 m/s at lower emission rates but decreases significantly to around 3.6 m/s as emission rates increase. Measurement noise level l_2 also starts with a very high average RMSE of around 60 m/s, which steeply decreases to about 18 m/s with increasing emission rates.

For a 6 m/s wind velocity, measurement noise level l_0 shows consistent average RMSE values around 1.4 m/s across all emission rates. Measurement noise level l_1 begins with a high average RMSE of approximately 60 m/s at low emission rates and decreases to around 3.6 m/s as emission rates increase. Measurement noise level l_2 starts with a very high average RMSE of about 64 m/s and decreases to approximately 9 m/s with higher emission rates.

At a wind velocity of 10 m/s, measurement noise level l_0 maintains consistent average RMSE values around 2.1 m/s. Measurement noise level l_1 starts with a very high average RMSE of around 60 m/s at lower emission rates and decreases to about 5 m/s as emission rates rise. Measurement noise level l_2 shows an initially extremely high average RMSE of approximately 66 m/s, which decreases steeply to around 12 m/s with increasing emission rates.

These observations highlight two key points regarding the average RMSE for a constant Δt. Firstly, the performance of the CIV Algorithm is highly dependent on the SNR, even when Δt is constant. As emission rates decrease and measurement noise levels increase, the performance of the CIV Algorithm deteriorates rapidly, particularly in comparison to scenarios with variable Δt. Secondly, for zero measurement noise (l_0), the average RMSE increases significantly relative to the true wind velocity as displacements decrease. For the smallest displacement of 60 meters (at 3 m/s wind velocity), the average RMSE is about 50% of the true wind velocity, whereas for the largest displacement of 200 meters (at 10 m/s wind velocity), it is around 21% of the true wind velocity. This trend was expected, as the contribution of random error relative to displacement increases when displacements are smaller. In the variable Δt scenario, where displacement is constant across wind velocities, this trend is not observed.

The average ME results, displayed in Figure 3.12, exhibit a similar trend across different plume characteristics. Notably, the magnitude of bias significantly increases under the constant Δt scenario. In the absence of measurement noise, a distinct pattern emerges: for displacements smaller than 150 meters, there is a significant positive bias, indicating an overestimation of the wind velocity field. Conversely, for displacements larger than 150 meters, a significant negative bias is observed, indicating an underestimation of the wind velocity field. This suggests a bias towards a displacement estimate of 150 meters.

In the constant Δt scenario, where all displacements are sub-pixel, the CIV Algorithm heavily relies on the Gaussian peak fitting procedure for displacement estimation. This procedure appears to introduce a bias towards a displacement of 150 meters for displacements below 300 meters. While peak locking is a common bias in PIV applications, where the bias is towards an integral peak location, the observed phenomenon in this case is a bias towards a sub-pixel location. As discussed in Section 3.2.1, the Gaussian peak fitting procedure has limitations in accurately fitting peak neighborhoods. Typically, the neighborhood peaks encountered in this thesis can be approximated by a Gaussian function with limited accuracy (see plot (b) in Figure 3.7), which may introduce biases. However, the exact cause of the bias towards 150 meters due to the Gaussian peak fitting procedure remains unexplained and warrants further analysis beyond the scope of this thesis.

With the introduction of measurement noise, the biases towards a 150-meter displacement diminish. Instead, all biases become negative, indicating a significant underestimation of the wind velocity fields. This shift to underestimation with added measurement noise is also observed in the variable Δt scenario, although the magnitude of this change is much more pronounced in the constant Δt scenario. When comparing bias magnitudes in the constant Δt scenario with those in the variable Δt scenario, the biases in the constant Δt scenario are more than 40% larger. Thus, the CIV Algorithm is increasingly susceptible to the negative effects of measurement noise with sub-pixel displacements. It is worth noting that SNR still significantly affects the biases, decreasing their magnitude as SNR improves.

In conclusion, the performance of the CIV Algorithm in the constant Δt scenario is notably poorer for wind velocity estimation based on sub-pixel displacements. Except for one scenario (10 m/s, l_2, 25 MT/y), the variable Δt scenario outperforms the constant Δt scenario across all plume characteristics.

3.3. CVision-CIV

As discussed in Chapter 1, advancements in CVision have significantly enhanced traditional velocimetry methods. While there has been significant progress in applying CVision to PIV, the use of CVision-CIV approaches for flow velocity estimation is still in its early stages. However, due to the similarity between PIV and CIV, CVision methods corresponding to PIV applications could be used to perform CIV. These methods typically involve Deep Learning with convolutional layers and can use either labeled or unlabeled data (O'Shea and Nash (2015)). They often require large training datasets and access to substantial computing power in order to train CVision models effectively. To leverage existing resources, publicly available methods, along with their trained models, are accessed and implemented in the research of this thesis.

One of the most promising CVision-PIV models and networks developed, trained, validated, and published is called UnLiteFLowNet-PIV created by Zhang and Piggott (2020). This model has been designed to estimate velocity fields from PIV imagery. It has been demonstrated to match the performance of traditional PIV approaches while surpassing them in complex flow regimes. Moreover, UnLiteFLowNet-PIV is capable of estimating high-quality velocity fields in significantly less time compared to traditional PIV methods. Finally, UnLiteFLowNet-PIV has been trained in an unsupervised manner using a complex loss function that tracks flows estimated forwards and backward in time. This approach allows the network to be trained on imagery of flows where the true flow structure is unknown, a characteristic shared with satellite imagery of emission plumes.

Due to these advantageous properties, the trained UnLiteFLowNet-PIV network has been extracted from Zhang and Piggott (2020) to serve as the foundation for the CVision-CIV approach proposed in this thesis. Transfer learning is applied in a supervised manner to adapt UnLiteFLowNet-PIV applying CIV to data of the type provided by the TANGO mission and enhancing the accuracy of wind velocity estimates based on satellite imagery.

3.3.1. UnLiteFLowNet-PIV and Extension

UnLiteFlowNet-PIV, derived from the LiteFlowNet architecture (Hui et al. (2018)), is a model designed for estimating displacements between image pairs. The model starts by using a two-stream convolutional neural network named NetC (Hui et al. (2018)) to extract features from the two input images displayed in Figure 3.13. Each stream processes one of the images. The two streams within NetC share the same weights, meaning they utilize identical parameters for processing both images. This ensures that the features extracted from both images are consistent and comparable. NetC employs a pyramidal structure to process the images at multiple scales. It starts with the full resolution and progressively reduces the resolution through each level of the pyramid, down to one-sixth of the original size. This multi-scale processing helps capture both fine details at higher resolutions and broader, more general features at lower resolutions.

After extracting features with NetC, the model moves to the decoder network, NetE (Hui et al. (2018)), displayed in Figure 3.13, which estimates the displacements between the two images. NetE performs cascaded displacement inference. This means it begins with the coarsest level of the pyramid (the lowest resolution) and estimates the displacements at this level. It then progressively refines the displacement estimates as it moves up through the pyramid levels to higher resolutions. This step-by-step refinement process helps improve the accuracy of the displacement estimates. Throughout the inference process, NetE incorporates displacement regularisation. This step is crucial for smoothing the displacement estimates and ensuring they are physically plausible, avoiding abrupt changes that are not realistic.

Once NetE completes the cascaded inference and regularisation, the displacement field estimate is still at a reduced resolution. To match the original image resolution, this estimate is upsampled using bilinear interpolation. This interpolation technique smoothly increases the resolution of the displacement field estimate, aligning it with the dimensions of the original input images.

UnLiteFlowNet-PIV effectively captures and computes an accurate displacement field between two images through a detailed process which can be transformed into a flow velocity field using the Δt between images and the image resolution. The model is trained using a complex loss function that includes photometric, smoothness, and consistency losses (Zhang and Piggott (2020)). The photometric loss evaluates how well the model's estimated flow aligns the first image with the second image. The smoothness loss penalizes abrupt changes in the flow field to ensure a smooth transition between neighboring pixel locations. The consistency loss enforces that the forward and backward flow estimates are consistent with each other. It checks that applying the forward flow to an image and then the backward flow should ideally return the original image, and vice versa. At last, the (combined) complex loss function compares the estimated displacement field with observed displacements, utilizing a dataset of 15,050 particle image pairs, each sized 256x256 pixels, with ground truth data obtained from computational fluid dynamics simulations. The dataset encompasses eight types of flow, including both uniform and turbulent flow at various Reynolds numbers. For a complete description of the training procedure, the reader is referred to Zhang and Piggott (2020).

UnLiteFlowNet-PIV is applied to emission plume imagery to estimate wind velocity fields. Similar to its PIV training procedure, it processes pairs of images taken at intervals of Δt. Due to the size of image pairs in DB_{TANGO}, image pairs are resized to 256x256 pixels. Rather than padding the input images, which results in large portions of UnLiteFlowNet-PIV being unused during transfer learning, the emission plume imagery is up-sampled to match the required input size. This approach ensures that all weights are utilized in the transfer learning process. Importantly, up-sampling does not impact the performance of the estimated flow fields, as it does not add or subtract any information into the input imagery.

UnLiteFlowNet-PIV was trained on black-and-white images, with each pixel value ranging between 0 and 1. Since CO2 emission plume images have values in PPM starting from 412, these images are normalized to fit the input requirements. This normalization enables UnLiteFlowNet-PIV to accurately estimate wind velocity fields from the up-sampled CO2 emission plume imagery.

The output of UnLiteFlowNet-PIV is a complete wind velocity field that spans the entire up-sampled pixel domain of the image pair. This is in contrast to the wind velocity field that is estimated by the CIV Algorithm which is made up of wind velocity estimates for pixel locations in l_p which is a subset of the entire pixel domain. So in order to effectively compare the wind velocity fields estimated by UnLiteFlowNet-PIV to those estimated by the CIV Algorithm, the wind velocity field estimated by UnLiteFlowNet-PIV is firstly down-sampled to match the initial dimensions of the simulated plume imagery. Thereafter, the estimated wind velocity field is filtered to contain wind velocity estimates for pixel locations in l_p. The set l_p is constructed identically to the one used in the CIV Algorithm such that the estimated wind velocity fields are comparable.

Since the output of UnLiteFlowNet-PIV is now comparable with the output of the CIV Algorithm, it is also compatible with the true wind velocity fields corresponding with the emission plume simulations. As a result, transfer learning is applied in a supervised manner since the comparable output of UnLiteFlowNet-PIV is labeled. The RMSE from Equation 3.4 is used as the loss function for the training procedure. The training set, DB_{train}, consisted of normalized image pairs, where $DB_{train} = DB_{TANGO} \setminus DB_{test}$. DB_{train} includes both noiseless and noisy imagery, aligning with DB_{test}, which contains both types. This alignment allows effective comparison of the results from the CIV Algorithm and the CVision-CIV approach. However, if CVision-CIV would be applied to real-world imagery, exclusively training on noisy imagery could enhance robustness to measurement noise of CVision-CIV networks.

UnLiteFlowNet-PIV is trained in two separate ways: on variable Δt imagery in DB_{train} with a constant displacement of 300 meters, and on constant Δt imagery with variable displacements across image pairs. This training distinction is made due to the contribution on random error relative to the displacements, which significantly effect the accuracy of the wind velocity estimates. To account for this effect two distinct training procedure are applied: a constant and a variable Δt training procedure. Both training procedures span 10 epochs, with each batch consisting of 8 entries. The learning rate is set to 1×10^{-4}, and the Adam optimizer is used with a weight decay of 1×10^{-5}, an epsilon value of 1×10^{-3}, and the AMSGrad variant enabled. This configuration ensures stable and efficient training. After undergoing transfer learning, the UnLiteFlowNet-PIV model evolves into two networks tailored for different scenarios: CVision-CIVnet for the variable Δt scenario and CVision-CIVnetcst for the constant Δt scenario. Both networks share identical architectures, as described in Figure 3.13.

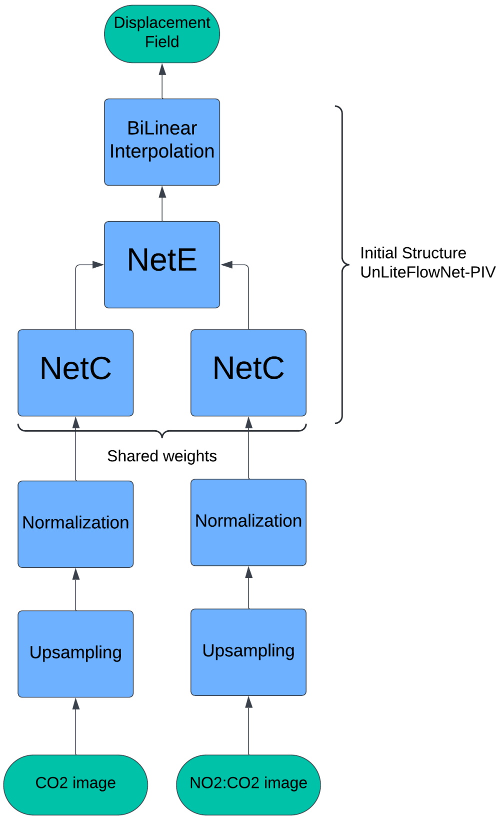

Figure 3.13: Architecture CVision-CIVnet and CVision-CIVnetcst.

3.3.2. Wind Velocity Estimation Results

The CVision-CIVnet's (CVision-CIVnet and CVision-CIVnetcst) provide as output a displacement field which is filtered by l_p and transformed into a wind velocity field using the Δt between images, and the image resolution. This wind velocity field consists of both components (u and v) of the wind velocity; however, due to the nature and alignment of the plume simulation, the v component of the estimated wind velocity is negligibly small. Therefore, this component is omitted from the analysis similarly to Section 3.2.2.

To analyze the accuracy of the wind velocity fields estimated by the CVision-CIVnet's, a comparison is made with the true wind velocities of each pixel location extracted from the CO2 plume simulations. To understand the nature and shape of the output of both CVision-CIVnet's, an image pair is selected, as was done in Section 3.2.2, from DB_{TANGO} for which the wind velocity field is estimated by CVision-CIVnet.

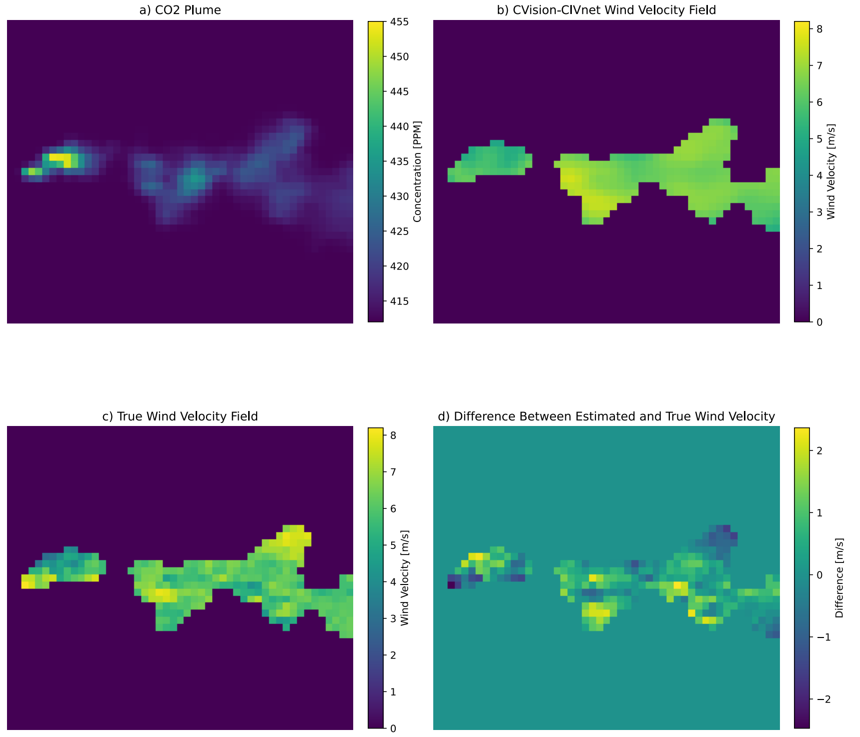

Figure 3.14: The first CO2 plume image in the image pair is displayed in plot (a). The resulting wind velocity field estimated by CVision-CIVnet is displayed in plot (b). For reference, the true wind velocity field filtered for pixel locations in l_p and the difference between the estimated and true wind velocity fields are displayed in plots (c) and (d) respectively. The plume characteristics included a true wind velocity of 6 m/s, an emission rate of 25 MT/y, a l_0 measurement noise level and a Δt of 50 seconds.

Figure 3.14 displays the first image in the image pair for which the wind velocity is estimated (plot (a)). The corresponding estimated wind velocity field for this image pair is also displayed in Figure 3.14 (plot (b)). Note that all pixel locations marked with a nonzero wind velocity estimate in plot (b) correspond to those within l_p. In the estimated wind velocity field, it is observed that there no longer exists a significant relationship between the distance of pixel locations to the emission source and the degree of underestimation of wind velocities. However, a clear smoothing of the wind velocity field is observed compared to the true wind velocity field (plot (c)). Since the underlying network, UnLiteFlowNet-PIV, was partially trained using a smoothness loss function, smoothing was expected to carry over into the transfer-trained CVision-CIVnet.

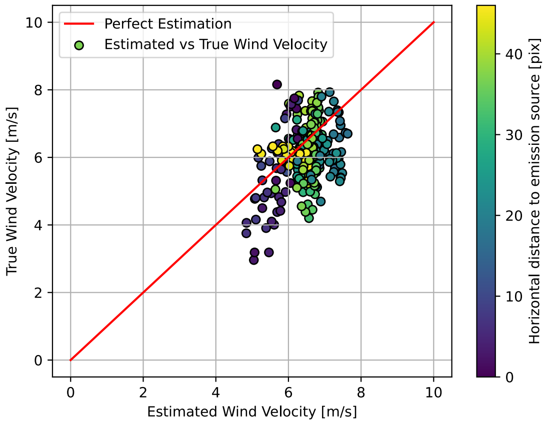

Figure 3.15: Accuracy plot of the wind velocity field estimated by CVision-CIVnet displayed in Figure 3.14. For perfect estimation, all points in the scatter plot lie on the red diagonal line. The scatter plot is color-coded with the horizontal distance from the emission source.

Figure 3.15 shows a scatter plot mapping the estimated wind velocity field to the true wind velocity field. Ideally, with perfect estimation and zero error, all points would lie on the red diagonal line; deviation from this line indicates estimation error. From Figure 3.15, it is evident that there is a significant estimation error across the entire wind velocity field. However, the cloud of points displayed in Figure 3.15 lies more closely on the diagonal line compared to the results displayed in Figure 3.10. Additionally, there are no clear indications of overestimation or underestimation of the wind velocity field. Due to the supervised training procedure, CVision-CIVnet learned not to underestimate the wind velocity of pixel locations near the emission source, in contrast to the CIV Algorithm.

The results displayed in Figure 3.14 and Figure 3.15 correspond to a single combination of plume characteristics. To effectively analyze the results and accuracy of CVision-CIVnet and CVision-CIVnetcst across all different combinations of plume characteristics, the input is scaled up from a single plume to several image pairs per combination of plume characteristics using DB_{test}. Similarly to the analysis of results corresponding to the CIV Algorithm, for each image pair in the four image pairs that belong to the same combination of plume characteristics, the RMSE and ME of the velocity field are computed using Equation 3.4 and Equation 3.5. Once all four RMSEs and MEs have been computed, they are averaged and stored as the average RMSE and ME for that combination of wind velocity, emission rate, measurement noise level, and Δt respectively. Due to the contribution of random error relative to the displacements between image pairs, which can significantly affect wind velocity estimation accuracy, the results of CVision-CIVnet and CVision-CIVnetcst for different combinations of plume characteristics are partitioned into two separate scenarios: variable Δt and constant Δt.

Scenario: Variable Δt

Firstly, the average RMSE and ME results of CVision-CIVnet are analyzed for a variable Δt. They are displayed in Appendix D in Table D.1 and Table D.2, respectively. Additionally, these results for CVision-CIVnet are plotted in Figure 3.16. Each average RMSE and ME value in Figure 3.16 is again complemented by an error bar representing the standard deviation of the average RMSE and ME, respectively.

Δt is varied from 100, 50, to 30 seconds, for wind velocities of 3, 6, and 10 m/s respectively. As a result, the contribution of random error to the results of CVision-CIVnet is constant relative to the displacement, enabling effective analysis and comparison across estimated wind velocity fields for different combinations of plume characteristics. Table D.1 presents the average RMSE values across different combinations of wind velocities, emission rates, measurement noise levels, and Δt for CVision-CIVnet. Each cell in the table represents the average RMSE computed from four image pairs per combination. Similarly, Table D.2 shows the average ME values for the same combinations. These tables provide a comprehensive overview of the performance of CVision-CIVnet in estimating wind velocities under varying conditions. In Figure 3.16, the performance of CVision-CIVnet is visually represented through plots of average RMSE and ME values. Each point in the plots corresponds to a specific combination of wind velocity, emission rate, measurement noise level, and Δt.

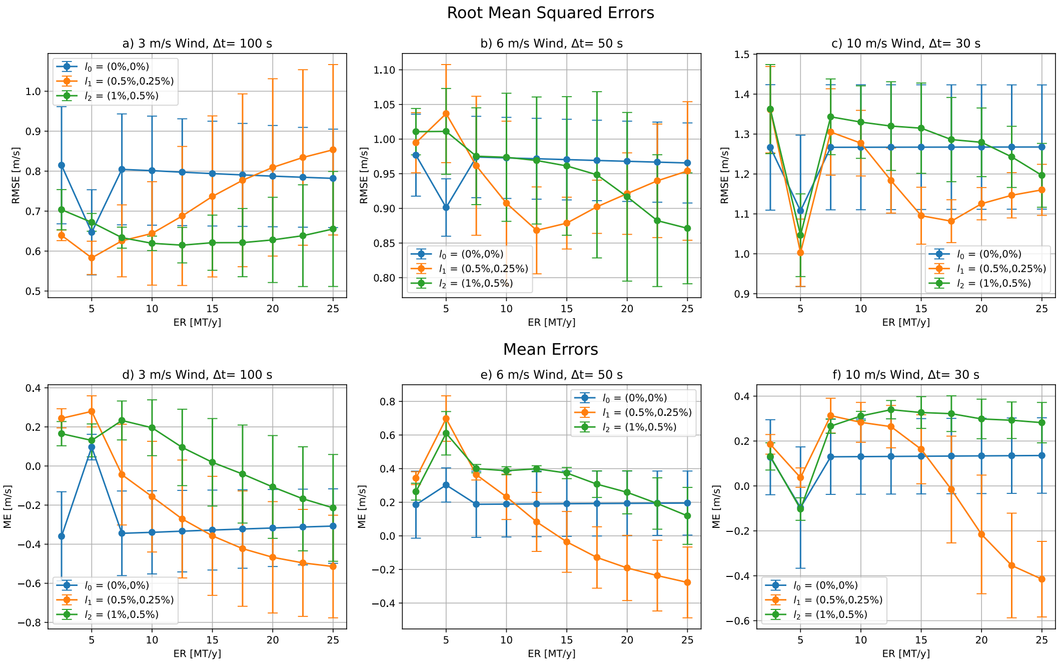

Figure 3.16: Plot (a) and (d) display the average RMSE and ME, respectively, for a Δt of 100 s, a wind velocity of 3 m/s and varying emission rates (ER) and measurement noise levels. Plot (b) and (e) display the average RMSE and ME for a Δt of 50 s, a wind velocity of 6 m/s and varying emission rates (ER) and measurement noise levels. Plot (c) and (f) display the average RMSE and ME for a Δt of 30 s, a wind velocity of 10 m/s and varying emission rates (ER) and measurement noise levels. All plots are complemented by a single standard deviation error-bar of the average RMSE and ME values.

The performance metrics of CVision-CIVnet are summarized in Figure 3.16, which illustrates the average RMSE and ME of the estimated wind velocity fields in plots (a), (b), and (c), and (d), (e), and (f) respectively. The emission rate of the plumes, given in megatons per year (MT/y), is plotted on the x-axis, while three different measurement noise levels (l_0, l_1, and l_2) are represented by different colors in each plot. The plots differentiate between three wind velocities: 3, 6, and 10 m/s.

For a wind velocity of 3 m/s (plot (a)), the average RMSE for measurement noise level l_0 generally remains around 0.8 m/s, with a slight decrease as emission rates increase. Measurement noise level l_1 begins with lower average RMSE values at lower emission rates but increases steadily, approaching 0.85 m/s. Measurement noise level l_2 maintains a consistent and minimal average RMSE of around 0.65 m/s, with a slight increase at higher emission rates. Notably, CVision-CIVnet performs progressively better for 3 m/s wind velocities when measurement noise is present. This improvement is due to CVision-CIVnet's training on low SNR imagery, which is typically noisy and features relatively high wind velocities (mean wind velocity in DB_{train} is 6.3 m/s).

At a wind velocity of 6 m/s (plot (b)), measurement noise level l_0 maintains a steady average RMSE of around 0.97 m/s across all emission rates. Measurement noise level l_1 shows considerable variation, with average RMSE decreasing to as low as 0.85 m/s at low emission rates before rising to 0.95 m/s at higher emission rates. Measurement noise level l_2 behaves similarly to l_1, starting below 0.95 m/s and gradually converging to about 0.9 m/s with increasing emission rates. Generally, the average RMSE falls within the 1-0.85 m/s range, indicating stable and favorable performance across all plume characteristics relative to the true wind velocity. For most cases with a 6 m/s true wind velocity, CVision-CIVnet performs better with noisy imagery due to its training on such data.

For a wind velocity of 10 m/s (plot (c)), measurement noise level l_0 yields an average RMSE of approximately 1.27 m/s. Measurement noise level l_1 shows a clear decrease at low emission rates, reducing average RMSE to around 1.1 m/s, but then increases and stabilizes near 1.5 m/s. Measurement noise level l_2 exhibits a decreasing trend, starting at about 1.35 m/s and decreasing to around 1.2 m/s as emission rates increase. Due to the training of CVision-CIVnet, it generally provides more accurate wind velocity estimates (i.e., lower average RMSE) when using noisy imagery for most cases. As with the 6 m/s wind velocity, CVision-CIVnet shows improved performance with noisy imagery due to its training.

The average ME results for a 3 m/s wind velocity (plot (d)) indicate that measurement noise level l_0 results in a negative bias at low emission rates, which increases slightly as emission rates rise, stabilizing around -0.2 m/s. Measurement noise level l_1 shows a transition from positive to negative average MEs, converging around -0.5 m/s at higher emission rates. Measurement noise level l_2 starts with slightly positive average MEs, decreasing to approximately -0.2 m/s.

At a wind velocity of 6 m/s (plot (e)), measurement noise level l_0 maintains a relatively stable average ME around 0.2 m/s with minor fluctuations, indicating a significant overestimation of the wind velocity field. Measurement noise level l_1 initially increases to about 0.6 m/s but gradually decreases to -0.3 m/s, reflecting an overshoot and a shift from overestimation to underestimation of the wind velocity field. Measurement noise level l_2 starts with higher average MEs around 0.3 m/s and decreases to nearly 0 at higher emission rates.

For a wind velocity of 10 m/s (plot (f)), measurement noise level l_0 remains around 0.13 m/s with minor fluctuations. Measurement noise level l_1 shows a significantly positive average ME at lower emission rates, peaking at 0.3 m/s before decreasing and stabilizing around 0. Measurement noise level l_2 starts with a positive average ME, which gradually decreases and stabilizes around 0.28 m/s. In most cases, the bias is positive, indicating a slight overestimation of the wind velocity field, though considerably less than the overestimation observed in the other algorithm. CVision-CIVnet does not display the same trend in overestimation magnitude with increasing measurement noise as seen in the other algorithm. However, a clear trend is observed in plots (d), (e), and (f) for measurement noise levels l_1 and l_2, where increasing emission rates lead to a negative bias, peaking at -0.4 m/s for an emission rate of 25 MT/y.

The results for CVision-CIVnet, displayed in Figure 3.16, underscore the significant impact of SNR on the accuracy of wind velocity estimations derived from emission plume imagery. Unlike the other algorithm, CVision-CIVnet's performance is better aligned with noisy imagery due to its training. Generally, the average RMSE and ME values are within a similar range for different emission rates but show significant changes when varying measurement noise levels. This change is less pronounced compared to the effect of measurement noise on the CIV Algorithm's results. CVision-CIVnet's superior performance with noisy imagery, relative to noiseless imagery, is consistent with its training on such data.

Comparing CVision-CIVnet with the CIV Algorithm, it is evident that CVision-CIVnet outperforms it in the variable Δt scenario across all plume characteristics. The average RMSE and bias magnitudes for CVision-CIVnet are considerably smaller compared to those of the CIV Algorithm, particularly for low SNR inputs corresponding to low emission rates, high measurement noise, and high wind velocities. The CIV Algorithm's accuracy deteriorates with low SNR imagery, while CVision-CIVnet is designed to handle such conditions effectively.

Scenario: Constant Δt

Secondly, the average RMSE and ME results of CVision-CIVnetcst are analyzed for a constant Δt of 20 seconds, mimicking the data product of TANGO. They are displayed in Table D.3 and Table D.4 respectively. Additionally, these results for CVision-CIVnetcst are plotted in Figure 3.17, again complemented by an error bar representing the standard deviation of the average RMSE and ME, respectively.

For a Δt of 20 seconds, the displacement between the image pairs is not constant but again a function of the wind velocity. For wind velocities of 3, 6, and 10 m/s displacements between image pairs are 60, 120, and 200 meters (all sub-pixel displacements), respectively. Due to this variability of displacements, the relative contribution of random error is no longer constant over plumes with different wind velocities. Therefore, an increased relative estimation error is expected to arise for combinations of plume characteristics with relatively smaller displacements, and vice versa for larger displacements.

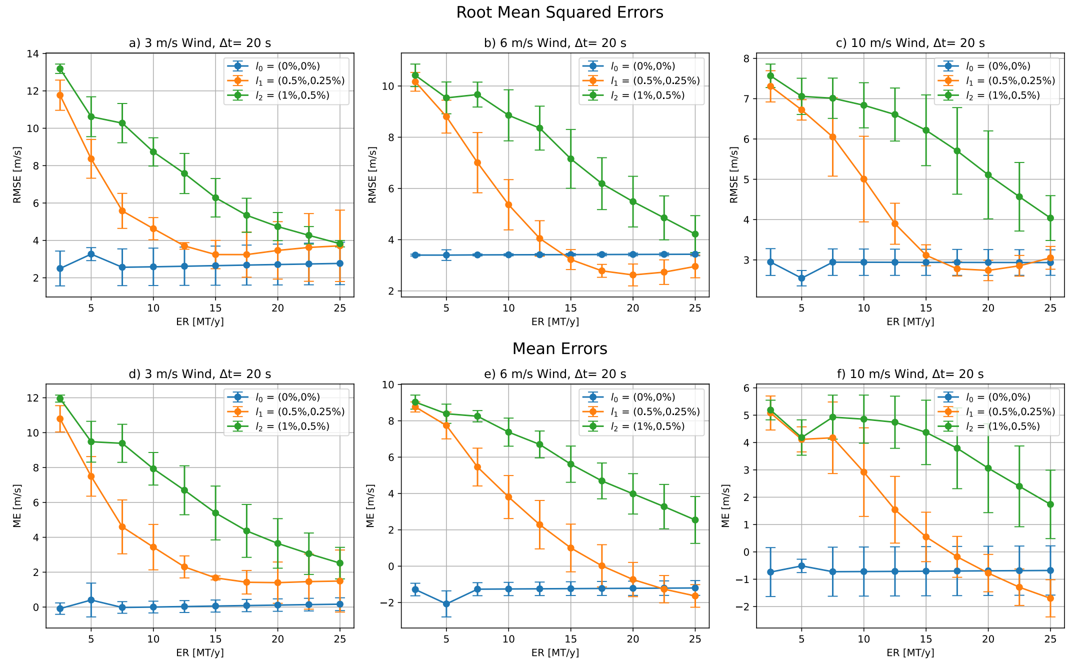

Figure 3.17: Plot (a) and (d) display the average RMSE and ME, respectively, for a Δt of 100 s, a wind velocity of 3 m/s and varying emission rates (ER) and measurement noise levels. Plot (b) and (e) display the average RMSE and ME for a Δt of 50 s, a wind velocity of 6 m/s and varying emission rates (ER) and measurement noise levels. Plot (c) and (f) display the average RMSE and ME for a Δt of 30 s, a wind velocity of 10 m/s and varying emission rates (ER) and measurement noise levels. All plots are complemented by a single standard deviation error-bar of the average RMSE and ME values.

The results for CVision-CIVnetcst with a constant Δt of 20 s are presented in Figure 3.17, which illustrates the average RMSE and ME of the estimated wind velocity fields in plots (a), (b), and (c), and (d), (e), and (f) respectively. The emission rate of the plumes, given in megatons per year (MT/y), is plotted on the x-axis, while three different measurement noise levels (l_0, l_1, and l_2) are represented by different colors in each plot. The plots differentiate between three wind velocities: 3, 6, and 10 m/s.

At a wind velocity of 3 m/s, measurement noise level l_0 maintains average RMSE values around 2.6 m/s across all emission rates, indicating a substantial error of approximately 80%. In contrast, measurement noise levels l_1 and l_2 begin with higher average RMSE values, approximately 11 m/s and 13 m/s respectively, at lower emission rates. As emission rates increase, the average RMSE for both measurement noise levels decreases significantly, converging towards 3.7 m/s for l_1 and 3.8 m/s for l_2 at higher emission rates.

For a wind velocity of 6 m/s, measurement noise level l_0 similarly shows stable and relatively low average RMSE values around 3.4 m/s. Measurement noise levels l_1 and l_2 exhibit higher initial average RMSE values (10.1 m/s and 10.4 m/s respectively) that decrease to approximately 2.9 m/s and 4.2 m/s as the emission rate increases.

At a wind velocity of 10 m/s, measurement noise level l_0 maintains low average RMSE values around 2.9 m/s. Measurement noise levels l_1 and l_2 start with high average RMSE values (7.3 m/s and 7.5 m/s respectively) which decrease to around 2.8 m/s for l_1 and 4.0 m/s for l_2 as the emission rate increases.

Analysis of the average ME at a 3 m/s wind velocity shows that measurement noise level l_0 maintains relatively low positive average ME values, indicating negligible positive biases from the actual wind velocities. Measurement noise levels l_1 and l_2 start with higher average ME values, approximately 10 m/s and 11 m/s respectively, at lower emission rates, and decrease to around 1.5 m/s for l_1 and 2.5 m/s for l_2 as emission rates increase.

At a wind velocity of 6 m/s, measurement noise level l_0 continues to exhibit significant negative average ME values, indicating an underestimation of the wind velocity fields. Measurement noise levels l_1 and l_2 start with very high average ME values, approximately 8.7 m/s and 9.0 m/s respectively, which decrease significantly to around -1.6 m/s for l_1 and -2.5 m/s for l_2 as the emission rate increases.

For a wind velocity of 10 m/s, measurement noise level l_0 maintains small negative average ME values relative to the true wind velocity, indicating only minor underestimation of the wind velocity fields. Measurement noise levels l_1 and l_2 start with very high average ME values, approximately 5.0 m/s and 5.1 m/s respectively, which decrease to around -1.3 m/s for l_1 and -1.7 m/s for l_2 as emission rates increase.

From this analysis, it is concluded that the performance of CVision-CIVnetcst improves as the observed displacement increases, similarly to the CIV Algorithm. For instance, with a true wind velocity of 3 m/s and a displacement of 60 meters, the average RMSE and ME are 13 m/s and 12 m/s, respectively. Conversely, for a true wind velocity of 10 m/s and a displacement of 200 meters, the average RMSE and ME are reduced to 7.5 m/s and 5 m/s, respectively. This pattern is caused by the contribution of random error relative to displacements, similar to the patterns observed in the performance of the CIV Algorithm in the constant Δt scenario. As displacement increase, this relative contribution decreases, increasing the accuracy of wind velocities, and vice versa.

These observations of the average RMSE and ME indicate significant variation across different plume characteristics, emphasizing the sensitivity of CVision-CIVnetcst to SNR in a constant Δt scenario with sub-pixel displacements. In contrast to the variable Δt scenario, SNR has a distinct effect on average RMSE and ME when Δt is constant with varying sub-pixel displacements across different wind velocities. As measurement noise is introduced, the average RMSE and ME of CVision-CIVnetcst across different combinations of plume characteristics quickly deteriorate, indicating an increased susceptibility to measurement noise in sub-pixel displacement estimation. However, as the SNR increases, the performance of CVision-CIVnetcst increases. The decreasing trends on the orange (l_1) and green (l_2) lines in all plots in Figure 3.17 indicate that as the emission rate increases, the performance of CVision-CIVnetcst increases due to the increased SNR. Additionally, it is observed in all plots in Figure 3.17 that the blue line (l_0) outperforms the orange line (l_1) in the majority of the cases. While the orange lines (l_1) consistently outperform the green line (l_2). Contrarily, this was not observed in the variable Δt scenario with constant displacements, where the average RMSE and ME of CVision-CIVnet laid in the 0.4-1 m/s bandwidth for all different SNR's respectively.

Assessing the overall performance of CVision-CIVnetcst, it is evident that in all combinations of plume characteristics, CVision-CIVnetcst is consistently outperformed by CVision-CIVnet. This is primarily due to the increased relative contribution of random error, as displacements are smaller in the variable Δt scenario compared to the constant Δt scenario. Additionally, CVision-CIVnetcst's performance is more susceptible to measurement noise due to its task of estimating sub-pixel displacements. When comparing the results of CVision-CIVnetcst with those of the CIV Algorithm, it is concluded that, in the constant Δt scenario, CVision-CIVnet outperforms the CIV Algorithm consistently for all different combinations of plume characteristics. This performance difference is most profound for low SNR input, corresponding to low emission rate, high measurement noise, and high wind velocity plumes. This is caused by the fact that the accuracy of the CIV Algorithm collapses for low SNR imagery while CVision-CIVnetcst is trained to deal with low SNR imagery.

3.4. Estimating CO2 Emission Rate

To estimate emission fluxes of CO2, a Mass Balance Method (MBM) is employed. This method is preferred over inversion methods due to the relative simplicity of MBM's, as discussed in Section 1.2.2. The MBM employed is the Cross-sectional Flux Method (CFM) (White et al. (1976), Beirle et al. (2011), Cambaliza et al. (2014), Kuhlmann et al. (2020), Goudar et al. (2023)), which relies on background-subtracted CO2 concentration measurements, δC_i^{CO2}, and the the complete wind velocity field. Contrarily, other MBM's often depend only on a single wind velocity vector for the entire plume. However, it is desirable to utilize all information regarding the estimated wind velocity field to enhance emission rate estimation.

The background-subtracted CO2 concentration measurements, δC_i^{CO2}, are obtained by subtracting the mean CO2 concentration observed before the emission plume source comes into view. In this thesis, the background concentration in emission plume imagery is artificially introduced, so its true value is known. However, in real-world scenarios, this is not the case. Therefore, to closely match real-world conditions, the background CO2 concentration is determined by computing the mean CO2 concentration observed before the emission source comes into view. This approach is relatively simple and can only be applied to emission plume imagery unaffected by any upwind emission sources that could influence the mean background concentration (Goudar et al. (2023)).

3.4.1. Cross-sectional Flux Method

The CFM operates by computing the emission flux for cross-sections stretching across the complete width of the plume that is perpendicular to the plume's velocity. In this thesis, the number of cross-sections for which a CO2 flux is estimated equals the number of pixel columns in the emission plume imagery. For each cross-section containing pixel locations where the wind velocity is estimated, the mean wind velocity over that cross-section, $\bar{u}_i$, can be computed. For cross-sections without such pixel locations, $\bar{u}_i$ is set to zero. Equation 3.6 illustrates how the emission flux Q_i for plume p can be estimated for each cross-section i, assuming a constant emission rate.

$$Q_i^p = \int_S \delta C_i^p(s) \cdot \bar{u}_i^p \, ds \cdot 3600s/h \cdot 24h/d \cdot 365d/y \cdot 10^{-9} MT/kg \tag{3.6}$$

where Q_i (in MT/y) is the emission flux through cross-section i, δC_i^{CO2} (in kg/m^2) is the background-subtracted CO2 values along a cross-section i, and $\bar{u}_i{}^p$ (in m/s) is the mean wind velocity perpendicular to the cross-section i. By converting PPM to kg/m^2 using atmospheric pressure and the molar mass of CO2 and air, the CO2 concentration in DB_{TANGO} can be used in Equation 3.6. To gain insight into the functioning of the CFM, $\bar{u}_i^p$ and Q_i^p are evaluated for the image pair and wind velocity fields estimated by CIV Algorithm and CVIsion-CIVnet, as illustrated in Figure 3.9 and Figure 3.14, respectively. The image pair in Figure 3.9 and Figure 3.14 were characterized with a true wind velocity of 6 m/s, a Δt of 50 seconds, an emission rate of 25 MT/y and l_0 measurement noise level. The resulting $\bar{u}_i^p$ and Q_i^p are displayed in Figure 3.18.

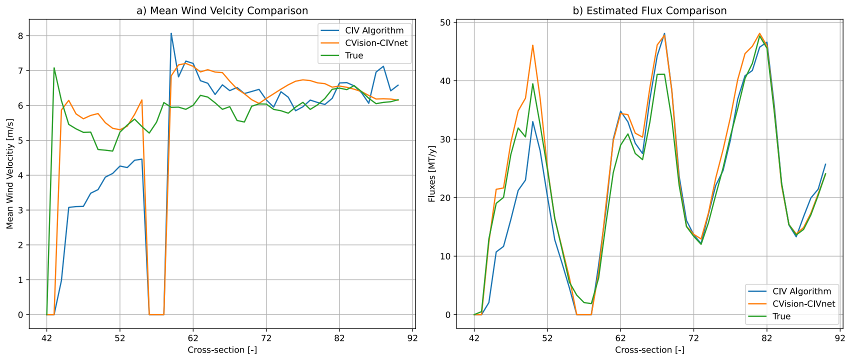

Figure 3.18: Plot (a) displays a comparison of the mean wind velocity, $\bar{u}_i^p$, and plot (b) displays a comparison of the estimate CO2 flux, Q_i^p. Both comparisons are made between wind velocities estimated by the CIV Algortihms, CVision-CIVnet and the true wind velocity field displayed in Figure 3.9 and Figure 3.14 respectively. The image pair in Figure 3.9 and Figure 3.14 were characterized with a true wind velocity of 6 m/s, a Δt of 50 seconds, an emission rate of 25 MT/y and l_0 measurement noise level.

Plot (a) in Figure 3.18 compares the mean wind velocities across different cross-sections estimated by the CIV Algorithm and CVision-CIVnet. The true mean wind velocity is also included for reference (green line). It is evident that the CIV Algorithm significantly underestimates the mean wind velocity near the source (at lower cross-section values). This underestimation is particularly noticeable in the initial segments of the cross-sections (from cross-sections 43 to 55), where the blue line representing the CIV Algorithm consistently falls below the true wind velocity. In contrast, the CVision-CIVnet method (orange line) tracks the true mean wind velocity more closely throughout the cross-sections, indicating a more accurate estimation. However, some underestimation is still observed in cross-sections close to the emission source (from cross-sections 42 to 44).

Plot (b) in Figure 3.18 compares the CO2 emission fluxes estimated using the two wind velocity estimation methods and the true wind velocity. The impact of the initial wind velocity underestimation by the CIV Algorithm is apparent in the CO2 emission flux results. The CIV Algorithm shows a lower CO2 emission flux near the source, corresponding to the initial underestimation of wind velocity. As a result, the CO2 emission flux values are significantly underestimated in the initial cross-sections. In contrast, the CVision-CIVnet method provides a more consistent and higher CO2 emission flux estimate near the source, aligning with the more accurate wind velocity estimations observed in the left plot in Figure 3.18.

As noted in Figure 3.9 and Figure 3.14, the percentile thresholding has segmented the emission plume into two distinct regions comprised of pixel locations in l_p, for which wind velocity is estimated by the CIV Algorithm and CVision-CIVnet. This segmentation results in cross-sections downstream of the source where no wind velocity estimates exist in the estimated wind velocity fields. As previously mentioned, $\bar{u}_i^p$ is set to zero for cross-sections without wind velocity estimates. This is observed in plot (a) in Figure 3.18, where $\bar{u}_i^p$ drops to zero at cross-sections 56 to 58 for both the CIV Algorithm and CVision-CIVnet, despite nonzero true wind velocities being present. Consequently, emission estimates for these cross-sections, where $\bar{u}_i^p$ is zero, are discarded when calculating the final emission rate estimate. The set of cross-sections that are not discarded is denoted as CS^*.

In plot (b) in Figure 3.18, significant oscillations are present in the values of Q_i^p for all wind velocity fields corresponding to the CIV Algorithm, CVision-CIVnet, and the true wind velocity field. The locations of these oscillations align with the blobs observed in Figure 3.9 and Figure 3.14 caused by turbulent atmospheric flow and the representation of a 3D plume as a 2D projection. Due to this variability in Q_i^p observed in plot (b) in Figure 3.18—a variability which shows no consistent pattern across different plumes—there is no universal optimal location for estimating cross-sectional flux (Goudar et al. (2023)). Therefore, the CO2 emission rate for plume p, ER^p, in MT/y, is estimated by taking the mean of Q_i over all cross-sections in CS^* where wind velocity estimates exist and $\bar{u}_i{}^p$ can be computed (Equation 3.7). This ensures that ER^p is not influenced by Q_i^p for cross-sections where $\bar{u}_i^p$ is artificially set to zero.

$$ER^p = \frac{1}{|CD^*|} \sum_{i \in CD^*} Q_i^p \tag{3.7}$$

To effectively quantify the performance of the application of the CFM on TANGO imagery, the CFM is applied on all noiseless plume imagery using the true wind velocities. Figure 3.19 displays the estimated emission rate using true wind velocities, ER_{true}^p, averaged over all noiseless plumes in DB_{TANGO} that belong to the same combination of plume characteristics. In Figure 3.19, emission rates estimated with the true wind velocities are mapped to the true emission rates, both given in MT/y. In an ideal case, with zero estimation error, all points in Figure 3.19 would lie on the red diagonal line.

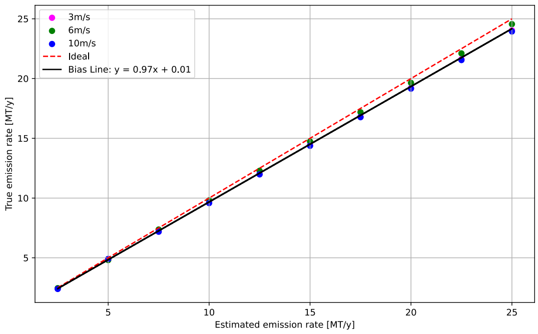

Figure 3.19: Accuracy plot of CO2 emission rates estimated using true wind velocity fields for noiseless image pairs in DB_{TANGO} with varying wind velocities and emission rates. The red line indicates perfect estimation while the black line displays an estimated linear regression on the estimated-to-true emission rate mapping.

As shown in Figure 3.19, the estimated emission rates for varying wind velocities and true emission rates closely align with the red diagonal line, which represents perfect estimation. This is further confirmed by the linear regression (black line) derived from the estimated-to-true emission rate mapping, where the slope is near 1, indicating a high degree of accuracy. The CFM's ability to accurately estimate emission rates using true wind velocity fields suggests that, when provided with accurate wind data, the CFM can achieve reliable emission rate estimations. Consequently, this demonstrates the potential of the CFM to effectively estimate emission rates from accurately estimated wind velocity fields.

3.4.2. Emission Estimation Results

ER^p is computed using estimated wind velocity fields estimated in 3.2.2 and 3.3.2. ER^{CIV} indicates emission rates estimated using the wind velocity field estimated by the CIV Algorithm. Conversely, $ER^{CVision}$ and $ER^{CVisioncst}$ indicate emission rates estimated using the wind velocity field estimated by CVision-CIVnet and CVision-CIVnetcst respectively. For each combination of plume characteristics, four plumes exist for which the emission rate is estimated. The error of the estimated emission rates is computed using Equation 3.8. At last, the error of the emission rate estimates is averaged across these different plumes to determine the accuracy of emission rate estimates for that particular combination of plume characteristics. The results corresponding to emission rate estimation are again partitioned into two separate scenarios: variable and constant Δt.

$$\epsilon^p = ER_{true} - ER^p \tag{3.8}$$

Variable Δt

The accuracy of ER^{CIV} and $ER^{CVision}$ for a variable Δt is analyzed. Figure 3.20 displays the averaged error (ϵ^{CIV} and $\epsilon^{CVision}$) of ER^{CIV} and $ER^{CVision}$ over four image pairs that correspond with one combination of plume characteristics. These errors are represented in % relative to the true emission rate with a corresponding error-bar computed from the standard deviation of the average errors of ER^{CIV} and $ER^{CVision}$. Within each figure, emission rate estimates that rely on wind velocities estimated by the CIV Algorithm and CVision-CIVnet, are compared.

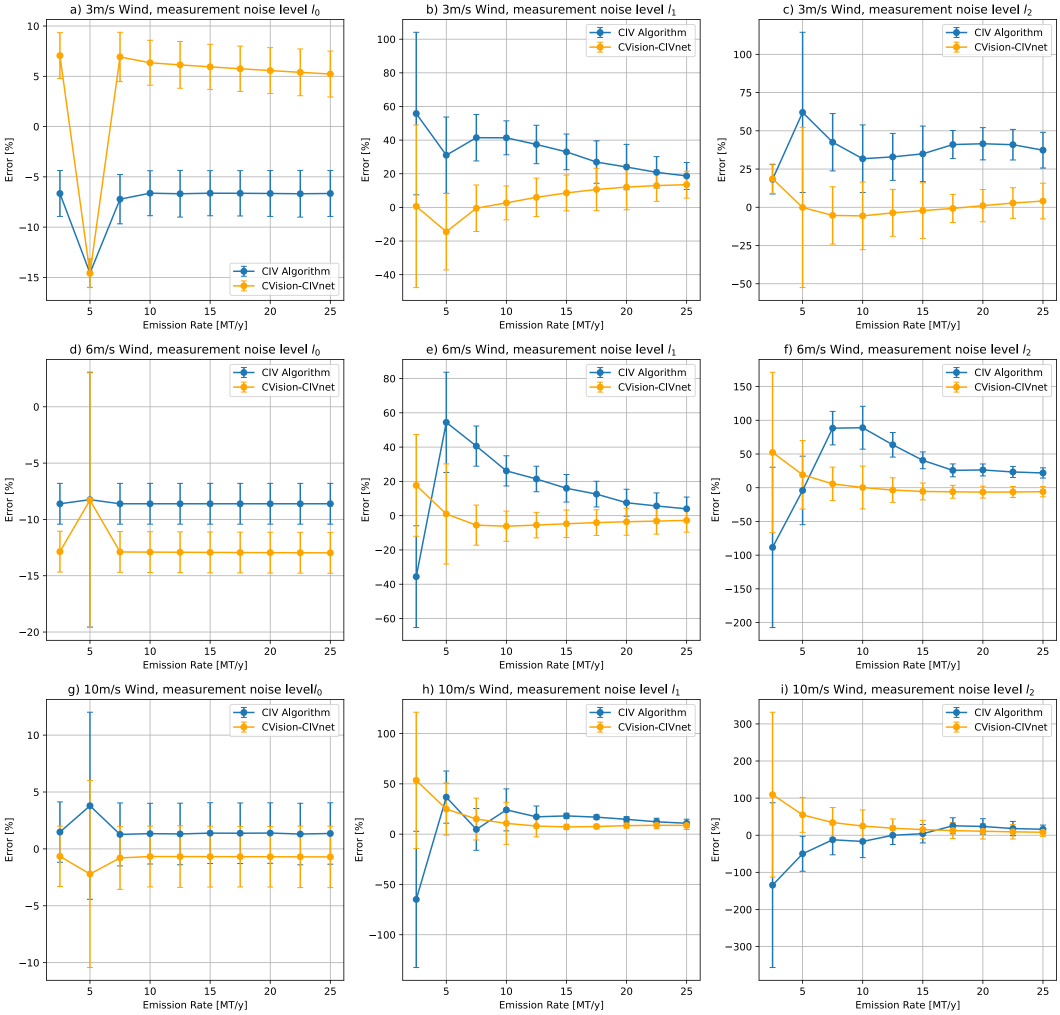

Figure 3.20: Plots (a), (b), and (c) show the average error of ER^{CIV} and $ER^{CVision}$ for a Δt of 100 s and a wind velocity of 3 m/s, corresponding to measurement noise levels l_0, l_1, and l_2, respectively. Plots (d), (e), and (f) show the average error of ER^{CIV} and $ER^{CVision}$ for a Δt of 50 s and a wind velocity of 6 m/s, corresponding to measurement noise levels l_0, l_1, and l_2, respectively. Plots (g), (h), and (i) show the average error of ER^{CIV} and $ER^{CVision}$ for a Δt of 30 s and a wind velocity of 10 m/s, corresponding to measurement noise levels l_0, l_1, and l_2, respectively. All plots are complemented by a single standard deviation error-bar of the average errors of ER^{CIV} and $ER^{CVision}$.

Figure 3.20 provides a comparative analysis of emission estimation errors using wind velocity fields estimated by both the CIV Algorithm and CVision-CIVnet across different wind velocities (3, 6, and 10 m/s) and measurement noise levels (l_0, l_1, and l_2). Each plot represents the error in emission estimation as a function of the emission rate computed using Equation 3.8, with different wind velocities and measurement noise levels, offering insights into the performance of the CFM under varying conditions and estimated wind velocity fields.

Similarly to the average RMSE and ME results discussed in Sections 3.2.2 and 3.3.2, at the lowest measurement noise level (l_0), both ER^{CIV} and $ER^{CVision}$ perform relatively well. However, $ER^{CVision}$ has lower error rates in the vast majority of combinations of plume characteristics, while ER^{CIV} outperforms $ER^{CVision}$ some (mainly noiseless cases). This was expected due to the performance of CVision-CIVnet in cases with no noise and low wind velocity. However, as the measurement noise level increases to l_1 and l_2, the performance of the CIV Algorithm deteriorates, with ER^{CIV} errors increasing substantially. In contrast, $ER^{CVision}$ errors maintain a more controlled error trend, demonstrating robustness to noise as was the case for the average RMSE and ME of the wind velocity fields estimated by CVision-CIVnet.

Detailed analysis of each plot reveals more specific trends. For a 3 m/s wind with measurement noise level l_0 (plot (a)), ER^{CIV} starts with an error around -7% and is stable as the emission rate increases, while $ER^{CVision}$ starts with an error of 7% at low emission rate but decreased to around 5% as emission rate increases. At measurement noise level l_1 (plot (b)),

ER^{CIV} errors show high variability, decreasing from 58% to about 20%, whereas $ER^{CVision}$ errors demonstrate an increase from 2% to around 15%. With measurement noise level l_2 (plot (c)), ER^{CIV} errors exhibit severe fluctuations, starting above 20%, with significant variations up to 62%. While $ER^{CVision}$ errors maintain a relatively lower and more stable error rate converging around 0%.

For a 6 m/s wind with measurement noise level l_0 (plot (d)), ER^{CIV} errors hover around -7%, whereas $ER^{CVision}$ errors remain consistently around -12%. At measurement noise level l_1 (plot (e)), ER^{CIV} errors show an initial value of -38% but increases to around 58% and converges to around 10% as emission rate increases, while $ER^{CVision}$ errors start around 18% but converges to 0% as emission rate increases. With measurement noise level l_2 (plot (f)), ER^{CIV} errors are significant and variable, starting at around -80% but converging around 25% from the positive side. While $ER^{CVision}$ shows a stable performance with errors converging to 0% starting at 50%.

For a 10 m/s wind with measurement noise level l_0 (plot (g)), ER^{CIV} errors are relatively stable around 2%, while $ER^{CVision}$ maintains consistent performance with errors around -1%. At measurement noise level l_1 (plot h), ER^{CIV} errors show significant variations starting at -60% but converge to 15% as emission rate increases, while $ER^{CVision}$ errors start at 52% and converge stably to 10%. With measurement noise level l_2 (plot i), ER^{CIV} exhibits significant errors starting at -120% and converging to 20%, while $ER^{CVision}$ errors are more stable converge to 10% without the variations seen in ER^{CIV}.

The general observations indicate that the CFM exhibits better and more stable performance across varying emission rates when using wind velocities estimated by CVision-CIVnet compared to the CIV Algorithm. The error margins corresponding to $ER^{CVision}$ are tighter and show less fluctuation, indicating higher reliability in emission estimations. Conversely, emission estimation errors display significant fluctuations, especially at higher measurement noise levels (l_2), when relying on wind velocities estimated by the CIV Algorithm, suggesting sensitivity to noise and varying emission rates. This observation aligns with the results discussed in Sections 3.2.2 and 3.3.2, where the negative effects of noise were most significant in wind velocity fields estimated by the CIV Algorithm.

Comparing Figure 3.11 and Figure 3.16 with Figure 3.20, it is evident that the behavior and trends of ER^{CIV} and $ER^{CVision}$ errors show similarity with those of the average MEs. This is caused by the linear relationship between the estimated emission rate and estimated wind velocity. The contribution of the average RMSEs is less significant since this contribution can cancel out in the averaging procedure of the CFM. Since the concentration values used in Equation 3.6 are constant, regardless of whether the CFM relies on the CIV Algorithm or CVision-CIVnet, the difference between ER^{CIV} and $ER^{CVision}$ can only originate from differences in estimated wind velocities. These similarities are not perfect, however, since emission rates estimated by the CFM rely on the estimated wind velocity in a manner weighted by concentration, not weighted equally. This effect is observed in plot (d) in Figure 3.20, where ER^{CIV} outperforms $ER^{CVision}$, whereas the performance of the CIV Algorithm corresponding with 6 m/s wind, l_0 measurement noise level are considerably worse than that of CVision-CIVnet. This behavior is limited to this combination of plume characteristics however, as, for all other combinations, $ER^{CVision}$ more accurately estimates emission rate compared to ER^{CIV}. Hence, the CFM performs better in the vast majority of cases, when it relies on wind velocity fields estimated by CVision-CIVnet, especially in scenarios where the SNR is relatively low.

Constant Δt

At last, the accuracy of ER^{CIV} and $ER^{CVisioncst}$ for a constant Δt of 20 seconds is analyzed. Figure 3.21 displays the averaged error (ϵ^{CIV} and $\epsilon^{CVisioncst}$) of ER^{CIV} and $ER^{CVisioncst}$ over all four image pairs that correspond with one combination of plume characteristics. These errors are represented in % relative to the true emission rate with a corresponding error-bar computed from the standard deviation of the average errors of ER^{CIV} and $ER^{CVisioncst}$. Within each figure, emission rate estimates that rely on wind velocities estimated by the CIV Algorithm and CVision-CIVnetcst for a constant Δt scenario, are compared.

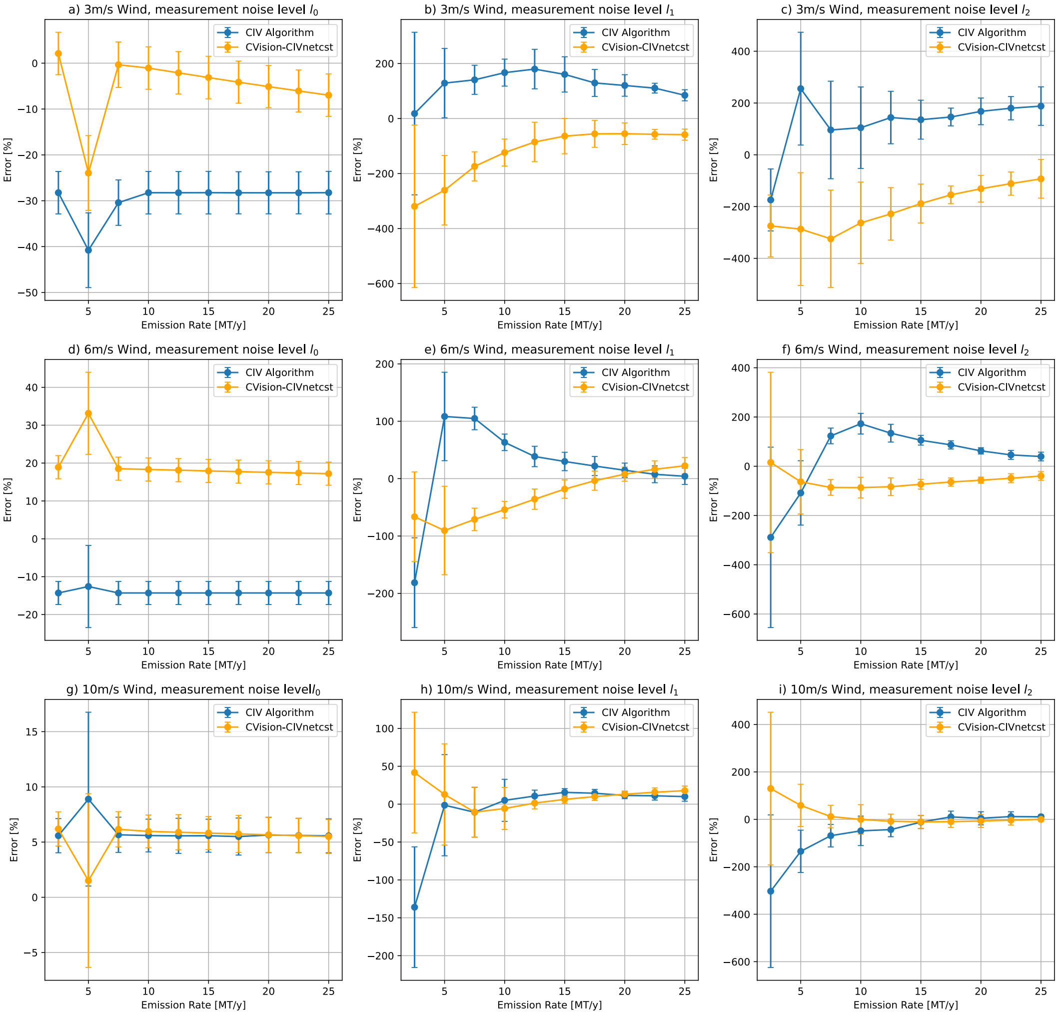

Figure 3.21: Plots (a), (b), and (c) show the average error of ER^{CIV} and $ER^{CVisioncst}$ for a Δt of 20 s and a wind velocity of 3 m/s, corresponding to measurement noise levels l_0, l_1, and l_2, respectively. Plots (d), (e), and (f) show the average error of ER^{CIV} and $ER^{CVisioncst}$ for a Δt of 20 s and a wind velocity of 6 m/s, corresponding to measurement noise levels l_0, l_1, and l_2, respectively. Plots (g), (h), and (i) show the average error of ER^{CIV} and $ER^{CVisioncst}$ for a Δt of 20 s and a wind velocity of 10 m/s, corresponding to measurement noise levels l_0, l_1, and l_2, respectively. All plots are complemented by a single standard deviation error-bar of the average errors of ER^{CIV} and $ER^{CVisioncst}$.

Figure 3.21 presents a comparative analysis of emission estimation errors using wind velocity fields estimated by the CIV Algorithm and CVision-CIVnetcst. This analysis is conducted across different wind velocities (3, 6, and 10 m/s) and measurement noise levels (l_0, l_1, and l_2). Each plot depicts the emission estimation error as a function of the emission rate computed using Equation 3.8, providing insights into the performance of the CFM under various conditions.

For a 3 m/s wind with measurement noise level l_0 (plot (a)), ER^{CIV} begins with an error around -39%, and remains stable as the emission rate increases, while $ER^{CVisionvcst}$ starts with an error of 3% at low emission rate and decreases to around -6% as emission rate increases. At measurement noise level l_1 (plot (b)), ER^{CIV} errors exhibit high variability, increasing from 15% to 190% ending up at around 80%, whereas $ER^{CVisioncst}$ errors increase from -300% to around -50%. With measurement noise level l_2 (plot (c)), ER^{CIV} errors start at -180% converging to 200%, while $ER^{CVisionvcst}$ errors converge from around -250% to -50%.

For a 6 m/s wind with measurement noise level l_0 (plot (d)), ER^{CIV} errors hover around -14%, whereas $ER^{CVisioncst}$ errors remain consistently around 18%. At measurement noise level l_1 (plot (e)), ER^{CIV} errors show an initial value of around -175% which rapidly increases and converges to around 0% as emission rate increases, while $ER^{CVisioncst}$ errors start around -80% but increase to 20% as emission rate increases. With measurement noise level l_2 (plot (f)), ER^{CIV} errors start at -260%, converging to 30%. $ER^{CVisioncst}$ shows a converging trend with

with errors converging from 10% to -30%.

For a 10 m/s wind with measurement noise level l_0 (plot (g)), ER^{CIV} and $ER^{CVisioncst}$ errors are relatively stable around 6%. At measurement noise level l_1 (plot h), ER^{CIV} errors show significant variations starting at -140% but converging to 10% as emission rate increases, while $ER^{CVisioncst}$ errors start at -45% and decrease significantly to around 15%. With measurement noise level l_2 (plot i), ER^{CIV} exhibits significant errors starting at -280% and converging to 0%, while $ER^{CVisioncst}$ errors are more stable and converge to 0% starting at -125% for low emission rates.

The performance of ER^{CIV} and $ER^{CVisioncst}$ indicates that the CFM achieves better and more consistent results when using wind velocities estimated by CVision-CIVnetcst compared to those from the CIV Algorithm. The error margins for $ER^{CVisioncst}$ are narrower and exhibit less fluctuation, signifying greater reliability in emission estimations. Conversely, the emission estimation errors show significant variability, especially at higher measurement noise levels (l_2), based on wind velocities estimated by the CIV Algorithm. As mentioned previously, the bias of the wind velocity field mainly dictates the accuracy of CO2 emission rate estimates. Thus the wind fields with the lower bias - those estimated by CVision-CIVnetcst - result in the most accurate CO2 emission rate estimates in cases where nonzero measurement noise is applied.

In general, the average error of estimated CO2 emission rates is significantly higher in the constant Δt scenario relative to the variable Δt scenario. This was expected since the accuracy of the estimated wind velocity fields is worse in the variable Δt scenario relative to the constant Δt scenario. In Figure 3.21, a trend can be observed that is similar to trends observed in Figure 3.12 and Figure 3.17, where the performance of the emission rate estimates increases displacements grow larger. For 10 m/s wind velocities with a displacement of 200 meters for both the CIV Algorithm and CVision-CIVnetcst with nonzero measurement noise, the emission rate estimates seem to converge to 0% average error as the emission rate increases, however for 3 m/s wind velocities with a displacement of 60 meters, they converge to nonzero average error. This is attributed to the relative contribution of random error to the estimated wind velocity fields which increases as displacements decrease.

4

Conclusion and Discussion

This thesis explored the feasibility of the TANGO mission in enhancing the monitoring of CO2 emissions through direct measurements of emission plume velocities. The TANGO mission, a pioneering satellite initiative, aims to improve the accuracy of anthropogenic greenhouse gas emission measurements. Comprising two satellites, TANGO-Carbon and TANGO-Nitro, it captures high-resolution data at 300m x 300m, significantly enhancing spatial resolution compared to its predecessors. Once TANGO becomes operational in 2027, its data product is designed to establish a framework for more accurate emission rate estimates. Even though it will take at least three years before TANGO becomes operational, simulated TANGO data, combined with wind velocity and emission rate estimation methods, can address the three questions posed in this thesis:

1. How can the TANGO mission facilitate a framework for directly measuring the velocity of emission plumes from concentrations of CO2 and NO2?
2. Can direct measurement of emission plume velocities contribute to a more accurate estimation of emission source rates?
3. How can mission or measurement parameters be optimized to enhance the accuracy of emission source rate estimations?

The subsequent sections address these research questions in detail. Section 4.1 evaluates the potential of the TANGO mission to establish a framework for direct measurement of emission plume velocities. Section 4.2 discusses how direct measurements of plume velocities could contribute to a more accurate estimation of emission rates. Finally, Section 4.3 explores the optimization of mission and measurement parameters to further enhance the accuracy of emission source rate estimates.

4.1. Wind Field Estimation

The TANGO mission's potential to directly measure emission plume velocities was confirmed through comprehensive simulations and analysis. Firstly, the TANGO data product was simulated using LES with MircoHH software, resulting in imagery corresponding to the image and temporal resolution of TANGO's data-product, consisting of CO2 and NO2 plume images. A variation of emission plume for different wind velocities, emission rates, Δt's and measurement noise levels was simulated.

The simulated plume imagery was used to estimate the wind velocity of emission plumes through two distinct methods: the CIV method and the CVision-CIV method, where the CVision-CIV method comprised two networks: CVision-CIVnet and CVision-CIVnetcst. Both methods estimated wind velocity fields of emission plumes spaced by a variable and constant Δt across different wind velocities, emission rates, and measurement noise levels. A distinction was made between scenarios with a variable and constant Δt to separately analyze constant and variable displacements for different wind velocities, respectively.

The CIV Algorithm relied on cross-correlating specific interrogation windows within the image pair to estimate displacement between them and transform estimated displacements into wind velocities. The CIV Algorithm was capable of estimating wind velocity fields from the image pairs for both variable and constant Δt scenarios, but it encountered significant limitations. Firstly, the CIV Algorithm significantly underestimated the wind velocity near the emission source due to high concentrations and the inherent stationarity of the emission source. Additionally, the CIV Algorithm could not accommodate low SNR image pairs; when measurement noise was introduced, the accuracy of its wind velocity field estimates quickly deteriorated. In the variable Δt scenario with constant displacements across all wind velocities, the wind velocity field estimated by the CIV Algorithm had, on average, a RMSE of 20% relative to the true wind velocity field. However, in the constant Δt scenario with variable displacements across all wind velocities, the limitations of the CIV Algorithm were amplified. The CIV Algorithm became more susceptible to introduced measurement noise, resulting in significantly worse accuracy of its wind velocity fields compared to the variable Δt scenario. Low SNR in this scenario led to RMSEs of wind velocity fields increasing by up to 1000%.

CVision-CIVnet demonstrated superior performance compared to the CIV Algorithm, with wind velocity fields outperforming those estimated by the CIV Algorithm in the majority of combinations of plume characteristics and the vast majority of combinations with nonzero measurement noise. Due to the training procedure of CVision-CIVnet, the underestimation of the wind velocity field near the emission source was significantly reduced. CVision-CIVnet was more capable of dealing with low SNR imagery relative to the CIV Algorithm due to its training true wind velocity fields. In the case of a variable Δt, CVision-CIVnet showed relatively stable performance over all different image pairs varying in SNR and wind velocities: on average, the RMSE of the estimated wind velocity field was 16% relative to the true wind velocity field, outperforming the CIV Algorithm, especially for low SNR image pairs. In the case of a constant Δt, CVision-CIVnetcst performed differently than its CVision-CIVnet counterpart. Its performance was significantly affected by the change in displacement magnitude and measurement noise on sub-pixel displacements, despite being trained on similar image pairs. Although CVision-CIVnetcst was less robust to introduced measurement noise compared to CVision-CIVnet, it still outperformed the CIV Algorithm for the majority of plume characteristic combinations. However, its performance was significantly worse compared to CVision-CIVnet for similar plumes.

Significant limitations with respect to the method of wind velocity estimation relate to the expected wind velocity field and plume imagery. Firstly, the flow direction of all emission plumes was aligned with x axis, thus the wind velocity was most pronounced in the x direction. As mentioned, the component of the wind velocity in the y direction was negligibly small and omitted from the analysis. However, emission plumes are not numerically aligned with the horizontal axis of an image taken by TANGO. It would be interesting to look into the performance of the CIV Algorithm and the CVision-CIVnet's that are trained on both components of the wind velocity field. Note that newly developed algorithms can artificially align non-aligned plumes by detecting and aligning them automically using satellite imagery, limiting the effect of multi-component wind velocity estimation. Additionally, data augmentation techniques could be employed to enhance the training dataset, providing a broader range of emission plumes and potentially improving the robustness of wind velocity estimations (Hernández-García and König (2018)). Secondly, the simulated CO2 and NO2 plumes were not affected by clouds in any way. However, in the real world, this is the case. Therefore, it is unknown how the CIV Algorithm and the CVision-CIVnet's respond to image pairs affected by clouds. Extending the CO2 and NO2 plume simulations to account for the effects of cloud interference (Twomey (1991)) and quantifying its contribution to the accuracy of wind velocity estimation by the CIV Algorithm and the CVision-CIVnet's would be interesting. Third, it would be interesting to examine the performance of the CIV Algorithm and CVision-CIVnetcst as Δt varies from 10 to 60 seconds, covering the entire range of TANGO with Δt< 60 seconds. As a result, displacements could range from 30 meters to 600 meters, depending on the observed wind velocity. This range allows for a comprehensive categorization of the performance of the CIV Algorithm and CVision-CIVnetcst as a function of displacement, facilitating the potential quantification of random error encountered in displacement estimation. Further in-depth analysis of the peak fitting function and procedure for the CCMs encountered in this thesis could limit the adverse effects of random error.

For both CVision-CIVnet models, it would be interesting to investigate the impact of incorporating more complex loss functions on performance. Since the current loss function

(RMSE) does not cover all desirable traits of an estimated wind velocity field, enhancing the loss function could improve the effectiveness of the transfer learning procedure. For instance, using a weighted combination of different performance metrics such as Endpoint Error, RMSE, and ME could provide a more robust training approach. Furthermore, applying the unsupervised learning procedure from Zhang and Piggott (2020) to the CVision-CIVnet's training procedures and investigating the effect on the quality of wind velocity field estimation would offer valuable insights into the use of real TANGO imagery in unsupervised training procedures.

In summary, this thesis demonstrates that flow fields, especially atmospheric wind velocity fields, can be estimated using traditional CIV and novel CVision-CIV techniques based on continuous concentration distributions, relying on simulated plume imagery intended to mimic the data-product of TANGO. However, the relatively low resolution, relatively small displacements and expected levels of measurement noise did affect the accuracy of wind velocity field estimates significantly.

Presently, atmospheric winds are often estimated from coarse and spatially sparse meteorological data, yet access to accurate wind velocity estimates with high temporal and spatial resolution is a significant improvement. The framework introduced in this thesis offers the capability to obtain these desirable wind velocity estimates, potentially eliminating the uncertain wind velocity estimates originating from meteorological data. Furthermore, this framework is not limited to the TANGO mission. Additional satellite networks exist in low- and geostationary orbit with data products compatible with the input requirements of the framework, that is, an image pair of the same plume spaced by Δt (Watine-Guiu et al. (2023)). These satellite networks are not only limited to observing CO2 and NO2 plumes, as CH4 and CO are also included with varying SNR imagery. However, the flow velocity estimation techniques introduced in this thesis are not restricted to atmospheric wind velocity fields though. In general, any accurately observed continuous concentration distribution can provide a framework for estimating flow fields through the CIV methods introduced in this thesis. The traditional technique of CIV, while proving to be flexible (key parameters can be tuned based on expected contrast and SNR) and advantageous in some cases (high SNR imagery), encountered significant limitations related to low SNR imagery. The novel CVision-CIV techniques were more capable of dealing with low SNR imagery than the traditional technique.

4.2. Emission Rate Estimation

To show the potential of estimated wind velocity fields with respect to emission rate estimation techniques, wind velocity fields estimated by the CIV Algorithm and the CVision-CIVnet's were used in the CFM to estimate CO2 emission rates for plumes with emission rates ranging from 2.5 to 25 MT/y. The CFM was chosen for its simplicity and complementarity to a wind velocity field instead of the average wind velocity of a plume. The emission rate estimation results showed that the CFM, combined with estimated wind velocity fields, was capable of estimating CO2 emission rates relatively accurately for the variable Δt scenario and inaccurately for the constant Δt scenario. The accuracy of its emission rate estimates depended greatly on the bias of estimated wind velocity fields.

For a variable Δt resulting in a constant displacement across all wind velocities, the CFM was capable of estimating CO2 emission rate at ±20% accuracy for over 93% of plumes for the lowest expected measurement noise level in TANGO (l_1) relying on CVision-CIVnet, including plumes with an emission rate of 2.5 MT/y. For the highest expected measurement noise level in TANGO (l_2), the CFM estimated CO2 emission rate at ±25% accuracy for over 85% of plumes relying on CVision-CIVnet, including plumes with an emission rate of 2.5 MT/y. Plumes for which the emission rate was not estimated with an accuracy of ±20% and ±25% respectively, all belonged to the lowest SNR categories, characterized by low emission rate or high wind velocity, or both. For a constant Δt where the displacement varied based on wind velocity, the CFM was unable to accurately estimate the CO2 emission rate due to the inaccurate wind velocity estimates provided by both the CIV Algorithm and CVision-CIVnetcst. For the majority of plumes with nonzero measurement noise, CO2 emission rates were overestimated by at least 50%, with cases below this overestimation threshold all having relatively high SNR, that is, high emission rate and low wind velocity.

In the constant Δt scenario, CO2 emission rate estimates depended greatly on SNR and wind velocity estimation methods. However, the accuracy of CO2 emission rate estimations worsened greatly compared to the variable Δt scenario. Similar to the trend observed in the accuracy of wind velocity estimates, the CFM performed better relying on the CIV Algorithm for small displacements (60 meters). While the CFM performed better relying on CVision-CIVnet for larger displacements (200 meters). Only as the emission rate increased to 20-25 MT/y did the CO2 emission rate estimates reach accuracy bandwidths similar to those encountered in the variable Δt scenario. For smaller emission rates (≤10 MT/y), the CFM significantly underestimated the CO2 emission rates when relying on both wind velocity estimation methods.

From the CFM results, it is evident that the ME of the wind velocity significantly affects the accuracy of the CO2 emission rate estimates, as the CFM's averaging procedure mitigates the impact of RMSE. Estimating emissions with the CFM, incorporating a different loss function in the CVision-CIVnet models, one that relies solely or partly on the ME of the wind velocity field would be worthwhile. Such a loss function could potentially reduce the bias in wind velocity field estimates produced by the CVision-CIVnet models, thereby directly improving the accuracy of the CFM results.

It would be interesting to explore the use of estimated wind velocity fields in other emission rate estimation techniques, particularly atmospheric dispersion models. Traditional methods for estimating emission rates often rely on simplified assumptions about wind velocity, which can be refined with access to an estimated wind velocity field. Tartakovsky et al. (2015) have demonstrated the promise of accurate wind velocity fields for improving atmospheric dispersion modeling. Validating this significance by comparing emission rate estimates from atmospheric dispersion models that rely on simplistic assumptions versus those that utilize a complete wind velocity field would be highly beneficial. Additionally, incorporating estimated wind velocity fields into existing machine learning approaches that estimate emission rates directly from plume imagery would be an intriguing path for future research. The estimated wind velocity fields can serve as an additional input layer alongside plume imagery in a CNN designed to estimate CO2 emissions. This technique was applied by Dumont Le Brazidec et al. (2023) using simulated wind velocity fields but has never been tested with estimated wind velocity fields. Dumont Le Brazidec et al. (2023) demonstrated that their CNN achieved unmatched accuracy in CO2 emission rate estimation compared to the CFM and other inversion methods when using true simulated wind velocity fields. Investigating how the performance of their CNN is affected by using estimated wind velocity fields would be valuable. Additionally, the CVision-CIVnet could be extended with one or more layers to include a regression output layer that estimates the CO2 emission rate directly, similar to the CH4 emission rate estimation networks developed by Jongaramrungruang et al. (2019) and Jongaramrungruang et al. (2022). Exploring the performance of this relatively simple approach with additive layers is worthwhile, given that CO2 plume imagery typically has lower SNR compared to the CH4 plume imagery used in Jongaramrungruang et al. (2019) and Jongaramrungruang et al. (2022).

In present research, dependency on uncertain wind velocities estimated from coarse meteorological data affected the accuracy of CO2 emission rates significantly. A recent study by Meier et al. (2024) indicates that inaccurate wind velocity estimates from meteorological data are the main limiting factor in emission rate estimation using the CFM. Never before has the wind velocity of an emission plume been measured remotely from space, let alone used in CO2 emission rate estimation. This thesis has shown the former and the latter to be possible to a certain extent. Previous research has mainly focused on estimating CO2 emission rates of power plants through various measurements and estimation techniques. However, due to the inherent limitations of low resolution and high detection limits of emission rates, the focus has mainly been on estimating the largest emission rates. Currently, limited studies are focusing on estimating emission rates from 25 MT/y down to 2.5 MT/y against which the accuracy of the emission rate estimation technique in this thesis can be compared. In one such study, Kuhlmann et al. (2020) demonstrated the ability to estimate CO2 emission rates ranging from 3.7 to 40.3 MT/y at a 1x1 km resolution and low measurement noise levels, with accuracy in a bandwidth of 39–150% relative to the true emission rate using a mass balance method that relies on meteorological data. However, there exist too few other studies with similar image resolution and emission rates to confidently and definitively conclude that the wind velocity estimation methods introduced in this thesis offer significant improvements in the estimation of emission rates. However, it can be stated that this thesis has shown the feasibility and potential of relying on estimated wind velocity which does not depend on meteorological data but on emission plume directly. Further research is needed to validate the potential of combining direct wind velocity estimation with emission rate estimation. This research should assess whether relying on wind velocity fields derived directly from plume imagery can lead to more accurate emission rate estimates. In an ideal world, such a validation could take place directly once TANGO becomes operational.

4.3. Mission and Measurement Optimization

The analysis of the accuracy of wind velocity and emission rate estimates uncovered valuable insights into their dependency on the mission and measurement parameters of TANGO. These parameters include the image resolution, measurement noise level of the measurement equipment in, and the Δt between TANGO-Carbon and TANGO-Nitro. Even though the TANGO mission has already been proposed to ESA and its requirements and specifications are relatively fixed (Landgraf et al. (2024)), some wiggling room does exist with respect to mission and measurement parameters. As a result, this thesis investigated the effect of this mission and measurement parameters on wind velocity and emission rate estimates.

The CIV Algorithm and its corresponding emission rate estimates showed a clear dependency on SNR, where higher SNRs yielded better results and vice versa. As a result, wind velocity fields could not accurately be estimated for relatively low emission rates. However, the effect of SNR could partly be mitigated by training a machine learning network to deal with low SNR imagery. For sub-pixel displacement, however, the adverse effects of measurement noise were present still in wind velocity fields estimated by the machine learning network. Additionally, the performances of the CIV Algorithm and CVision-CIVnet showed that the relative contribution of random error on wind velocity fields decreases as the displacements between image pairs increase. Therefore, maximizing the Δt between TANGO-Carbon and TANGO-Nitro would minimize the relative contribution of this random error on wind velocity field estimates, resulting in more accurate wind velocity field estimates.

Once TANGO becomes operational, it would be interesting to look into the possible advantages that forward motion compensation (FMC) of imagery, a capability TANGO offers (Landgraf et al. (2024)). FMC in satellite imagery is a technique used to correct for the motion of the satellite as it orbits the Earth. As a satellite moves, it captures images while continuously changing its position, which can cause blurring in the captured images due to the relative motion between the satellite and the Earth's surface. In the case of TANGO, FMC involves adjusting the imaging sensor to counteract this motion, thereby reducing or eliminating the blur. This is achieved by predicting the satellite's motion and applying compensatory adjustments to the sensor's position or the captured image data. As FMC is applied, both CO2 and NO2 plumes are imaged in a continuous fashion spanning a certain period of time. As a result, the CO2 and NO2 plume imagery spans a certain time interval per plume, enabling the selection of several image pairs varying in Δt. Essentially, Δt is no longer constant and can be adjusted slightly (Landgraf et al., 2024) based on one's preference. Since measurement noise has an increased negative effect on the accuracy of wind velocity fields estimated from sub-pixel displacements, Δt should be optimized to convert sub-pixel displacements into pixel displacements, reducing susceptibility to measurement noise in wind velocity estimation methods. However, for Δt to be optimized, the true displacement, which is inherently unknown, must be known. Meteorological data, however, could be used to provide a rough estimate of the expected displacement of the observed emission plume. As a result, Δt could be optimized for the expected displacement, providing more accurate wind velocity field estimates.

The CO2 and NO2 plume imagery can potentially benefit from super-resolution techniques, enabled by the continuous nature of the imagery, to enhance image resolution and improve the accuracy of wind velocity field estimations using both the CIV Algorithm and the CVision-CIVnet's. Super-resolution is a technique employed to enhance an image's resolution beyond the limitations of the original sensor by estimating and adding finer details, effectively increasing the image's pixel density and clarity. This process can be achieved through various methods, including interpolation, machine learning models, and iterative reconstruction techniques. Super-resolution has been extensively applied to remote sensing imagery (Lu et al. (2019), Karwowska and Wierzbicki (2022), Cornebise et al. (2022)). However, it is important to acknowledge the limitations and potential pitfalls associated with these techniques (Park et al. (2003)). Basic interpolation, for instance, does not add any new information to the image. While machine learning models can generate visually appealing higher-resolution images, the details added through upscaling are highly dependent on the training of the neural network. In some cases, the additional information might reflect the characteristics of the training dataset rather than the actual scene, potentially interfering with measurements. Future research could explore the application of super-resolution techniques within the framework introduced in this thesis, with a clear understanding of their limitations.

References

Abdulwahab, Mohammed Raad, Yasir H Ali, Fatima J Habeeb, Abdoulhadi A Borhana, Ahmed M Abdelrhman, and Salah M Ali Al-Obaidi (2020). “A review in particle image velocimetry techniques (developments and applications)”. *Journal of Advanced Research in Fluid Mechanics and Thermal Sciences* 65.2, pp. 213–229.

Adrian, Ronald J (1984). “Scattering particle characteristics and their effect on pulsed laser measurements of fluid flow: speckle velocimetry vs particle image velocimetry”. *Applied optics* 23.11, pp. 1690–1691.

Arakawa, Akio and Vivian R Lamb (1977). “Computational design of the basic dynamical processes of the UCLA general circulation model”. *General circulation models of the atmosphere* 17.Supplement C, pp. 173–265.

Ardeshiri, Hamidreza, Massimo Cassiani, Soon Young Park, Andreas Stohl, Ignacio Pisso, and Anna Solvejg Dinger (2020). “On the convergence and capability of the large-eddy simulation of concentration fluctuations in passive plumes for a neutral boundary layer at infinite Reynolds number”. *Boundary-Layer Meteorology* 176, pp. 291–327.

Association, World Nuclear (2024). *Carbon Dioxide Emissions from Electricity*. Accessed: 19-02-2024. URL: `https://world-nuclear.org/information-library/energy-and-the-environment/carbon-dioxide-emissions-from-electricity.aspx`.

Baray, Sabour, Andrea Darlington, Mark Gordon, Katherine L Hayden, Amy Leithead, Shao-Meng Li, Peter SK Liu, Richard L Mittermeier, Samar G Moussa, Jason O’Brien, et al. (2018). “Quantification of methane sources in the Athabasca Oil Sands Region of Alberta by aircraft mass balance”. *Atmospheric Chemistry and Physics* 18.10, pp. 7361–7378.

Barker, DB and ME Fourney (1977). “Measuring fluid velocities with speckle patterns”. *Optics letters* 1.4, pp. 135–137.

Barratt, Rod (2013). *Atmospheric dispersion modelling: an introduction to practical applications*. Routledge.

Bates, DR (1984). “Rayleigh scattering by air”. *Planetary and Space Science* 32.6, pp. 785–790.

Beirle, Steffen, K Folkert Boersma, Ulrich Platt, Mark G Lawrence, and Thomas Wagner (2011). “Megacity emissions and lifetimes of nitrogen oxides probed from space”. *Science* 333.6050, pp. 1737–1739.

Benjamin, Stanley G, Stephen S Weygandt, John M Brown, Ming Hu, Curtis R Alexander, Tatiana G Smirnova, Joseph B Olson, Eric P James, David C Dowell, Georg A Grell, et al. (2016). “A North American hourly assimilation and model forecast cycle: The Rapid Refresh”. *Monthly Weather Review* 144.4, pp. 1669–1694.

Boersma, KF, HJ Eskes, and EJ Brinksma (2004). “Error analysis for tropospheric NO2 retrieval from space”. *Journal of Geophysical Research: Atmospheres* 109.D4.

Bovensmann, H, M Buchwitz, JP Burrows, M Reuter, T Krings, K Gerilowski, O Schneising, J Heymann, A Tretner, and Joerg Erzinger (2010). “A remote sensing technique for global monitoring of power plant CO 2 emissions from space and related applications”. *Atmospheric Measurement Techniques* 3.4, pp. 781–811.

Brantley, Halley L, Eben D Thoma, and Adam P Eisele (2015). “Assessment of volatile organic compound and hazardous air pollutant emissions from oil and natural gas well pads using mobile remote and on-site direct measurements”. *Journal of the Air & Waste Management Association* 65.9, pp. 1072–1082.

Brantley, Halley L, Eben D Thoma, William C Squier, Birnur B Guven, and David Lyon (2014). “Assessment of methane emissions from oil and gas production pads using mobile measurements”. *Environmental science & technology* 48.24, pp. 14508–14515.

Cambaliza, MOL, PB Shepson, DR Caulton, B Stirm, D Samarov, KR Gurney, J Turnbull, KJ Davis, A Possolo, A Karion, et al. (2014). “Assessment of uncertainties of an aircraft-based mass balance approach for quantifying urban greenhouse gas emissions”. *Atmospheric Chemistry and Physics* 14.17, pp. 9029–9050.

Cenedese, A, GP Romano, A Paglialunga, and M Terlizzi (1992). “Neural net for trajectories recognition in a flow”. In: *Sixth International Symposium on Applications of Laser Techniques to Fluid Mechanics*, pp. 20–23.

Ciais, P., D. Crisp, H.D. Van Der Gon, R. Engelen, M. Heimann, P. Rayner, M. Scholze, B. Pinty, H. Zunker, V. Hoorne, G. Janssens-Maenhout, and S. Barbier (2015). “Towards a European

Operational Observing System to Monitor Fossil CO2 Emissions”. *European Commission, Brussels*.

Cornebise, Julien, Ivan Oršolić, and Freddie Kalaitzis (2022). “Open high-resolution satellite imagery: The worldstrat dataset–with application to super-resolution”. *Advances in Neural Information Processing Systems* 35, pp. 25979–25991.

Cusworth, D. H., R. M. Duren, A. K. Thorpe, M. L. Eastwood, R. O. Green, P. E. Dennison, C. Frankenberg, J. W. Heckler, G. P. Asner, and C. E. Miller (2021). “Quantifying global power plant carbon dioxide emissions with imaging spectroscopy”. *AGU Advances*.

DeCola, P. and W.M.O Secretariat (2017). “An integrated global greenhouse gas information system (IGIS)”. *World Meteorol. Org. Bull.* 66.1, pp. 38–45.

Domínguez, Diego, Jesús Gonzalo, and Deibi López (2013). “A wind speed profile measurement method based on free bubble tracking in the lower atmosphere”. *Flow Measurement and Instrumentation* 34, pp. 134–141.

Dosovitskiy, Alexey, Philipp Fischer, Eddy Ilg, Philip Hausser, Caner Hazirbas, Vladimir Golkov, Patrick Van Der Smagt, Daniel Cremers, and Thomas Brox (2015). “Flownet: Learning optical flow with convolutional networks”. In: *Proceedings of the IEEE international conference on computer vision*, pp. 2758–2766.

Dudderar, TD and PG Simpkins (1977). “Laser speckle photography in a fluid medium”. *Nature* 270.5632, pp. 45–47.

Dumont Le Brazidec, Joffrey, Pierre Vanderbecken, Alban Farchi, Grégoire Broquet, Gerrit Kuhlmann, and Marc Bocquet (2023). “Deep learning applied to CO 2 power plant emissions quantification using simulated satellite images”. *Geoscientific Model Development Discussions* 2023, pp. 1–30.

Dvorak, Vernon F (1975). “Tropical cyclone intensity analysis and forecasting from satellite imagery”. *Monthly Weather Review* 103.5, pp. 420–430.

Ebuchi, Naoto (1999). “Statistical distribution of wind speeds and directions globally observed by NSCAT”. *Journal of Geophysical Research: Oceans* 104.C5, pp. 11393–11403.

Finch, Douglas P, Paul I Palmer, and Tianran Zhang (2022). “Automated detection of atmospheric NO 2 plumes from satellite data: a tool to help infer anthropogenic combustion emissions”. *Atmospheric Measurement Techniques* 15.3, pp. 721–733.

Fincham, A and G Delerce (2000). “Advanced optimization of correlation imaging velocimetry algorithms”. *Experiments in Fluids* 29.Suppl 1, S013–S022.

Fincham, AM and GR Spedding (1997). “Low cost, high resolution DPIV for measurement of turbulent fluid flow”. *Experiments in Fluids* 23.6, pp. 449–462.

Foster-Wittig, T. A., E. D. Thoma, and J. D. Albertson (2015). “Estimation of point source fugitive emission rates from a single sensor time series: A conditionally-sampled Gaussian plume reconstruction”. *Atmospheric Environment* 115, pp. 101–109.

Fried, Alan, James Walega, Petter Weibring, Dirk Richter, Isobel J Simpson, Donald R Blake, Nicola J Blake, Simone Meinardi, Barbara Barletta, Stacey C Hughes, et al. (2020). “Airborne formaldehyde and volatile organic compound measurements over the Daesan petrochemical complex on Korea’s northwest coast during the Korea-United States Air Quality study: Estimation of emission fluxes and effects on air quality”. *Elem Sci Anth* 8.1, p. 121.

Gharib, Morteza, Dymphy Kremers, M Koochesfahani, and Martin Kemp (2002). “Leonardo’s vision of flow visualization”. *Experiments in fluids* 33, pp. 219–223.

Goldberg, Daniel L, Zifeng Lu, Tomohiro Oda, Lok N Lamsal, Fei Liu, Debora Griffin, Chris A McLinden, Nickolay A Krotkov, Bryan N Duncan, and David G Streets (2019). “Exploiting OMI NO2 satellite observations to infer fossil-fuel CO2 emissions from US megacities”. *Science of The Total Environment* 695, p. 133805.

Gonzalo, Jesús, Diego Domínguez, Deibi López, and Joaquín Fernández (2014). “Lighter-than-air particle velocimetry for wind speed profile measurement”. *Renewable and Sustainable Energy Reviews* 33, pp. 323–332.

Gordon, M, S-M Li, R Staebler, A Darlington, K Hayden, J O’Brien, and M Wolde (2015). “Determining air pollutant emission rates based on mass balance using airborne measurement data over the Alberta oil sands operations”. *Atmospheric Measurement Techniques* 8.9, pp. 3745–3765.

Goudar, Manu, Juliëtte CS Anema, Rajesh Kumar, Tobias Borsdorff, and Jochen Landgraf (2023). “Plume detection and emission estimate for biomass burning plumes from TROPOMI carbon monoxide observations using APE v1. 1”. *Geoscientific Model Development* 16.16, pp. 4835–4852.

Grant, I and X Pan (1997). “The use of neural techniques in PIV and PTV”. *Measurement Science and Technology* 8.12, p. 1399.

Grousson, R and S Mallick (1977). "Study of flow pattern in a fluid by scattered laser light". *Applied Optics* 16.9, pp. 2334–2336.

Guevara, Marc, Santiago Enciso, Carles Tena, Oriol Jorba, Stijn Dellaert, Hugo Denier van der Gon, and Carlos Pérez García-Pando (2023). "A global catalogue of CO 2 emissions and co-emitted species from power plants at a very high spatial and temporal resolution". *Earth System Science Data Discussions* 2023, pp. 1–41.

Hagura, Hiroto and Toshio Koizumi (1990). "Development of a Wind Observation System Utilizing Simplified Aerial Photogrammetry (1) Development of a System and an Attempt to Observe Paths of Particle of Wind Flowing over Buildings". *Wind Engineers, JAWE* 1990.45, pp. 1–14.

Hakkarainen, Janne, Monika E Szeląg, Iolanda Ialongo, Christian Retscher, Tomohiro Oda, and David Crisp (2021). "Analyzing nitrogen oxides to carbon dioxide emission ratios from space: A case study of Matimba Power Station in South Africa". *Atmospheric Environment: X* 10, p. 100110.

Hassan, YA and OG Philip (1997). "A new artificial neural network tracking technique for particle image velocimetry". *Experiments in Fluids* 23.2, pp. 145–154.

Hernández-García, Alex and Peter König (2018). "Further advantages of data augmentation on convolutional neural networks". In: *Artificial Neural Networks and Machine Learning–ICANN 2018: 27th International Conference on Artificial Neural Networks, Rhodes, Greece, October 4-7, 2018, Proceedings, Part I 27*. Springer, pp. 95–103.

Hiran, Kamal Kant, Ritesh Kumar Jain, Kamlesh Lakhwani, and Ruchi Doshi (2021). *Machine Learning: Master Supervised and Unsupervised Learning Algorithms with Real Examples (English Edition)*. BPB Publications.

Hogue, S., E. Marland, R.J. Andres, G. Marland, and D. Woodard (2016). "Uncertainty in gridded CO2 emissions estimates". *Earth's Future* 4.5, pp. 225–239.

Holmes, N.S. and L. Morawska (2006). "A review of dispersion modelling and its application to the dispersion of particles: An overview of different dispersion models available". *Atmospheric Environment* 40.30, pp. 5902–5928. ISSN: 1352-2310.

Hosseini, B. and J. M. Stockie (2016). "Bayesian estimation of airborne fugitive emissions using a Gaussian plume model". *Atmospheric Environment* 141, pp. 122–138.

Hu, Yaqin and Yusheng Shi (2021). "Estimating CO2 emissions from large scale coal-fired power plants using OCO-2 observations and emission inventories". *Atmosphere* 12.7, p. 811.

Hui, Tak-Wai, Xiaoou Tang, and Chen Change Loy (2018). "Liteflownet: A lightweight convolutional neural network for optical flow estimation". In: *Proceedings of the IEEE conference on computer vision and pattern recognition*, pp. 8981–8989.

Hutchinson, M., H. Oh, and W. Chen (2017). "A review of source term estimation methods for atmospheric dispersion events using static or mobile sensors". *Information Fusion* 36, pp. 130–148. ISSN: 1566-2535.

Ilg, Eddy, Nikolaus Mayer, Tonmoy Saikia, Margret Keuper, Alexey Dosovitskiy, and Thomas Brox (2017). "Flownet 2.0: Evolution of optical flow estimation with deep networks". In: *Proceedings of the IEEE conference on computer vision and pattern recognition*, pp. 2462–2470.

Jahan, Ismot, Mohamed Mehana, Bulbul Ahmmed, Javier E Santos, Daniel O'Malley, and Hari Viswanathan (2023). "Deep Learning Models for Methane Emissions Identification and Quantification". In: *SPE/AAPG/SEG Unconventional Resources Technology Conference*. URTEC, D021S043R003.

Jeong, H., E. Kim, K. Suh, W. Hwang, M. Han, and H. Lee (2005). "Determination of the source rate released into the environment from a nuclear power plant". *Radiation Protection Dosimetry* 113.3, 308–313.

Jongaramrungruang, Siraput, Christian Frankenberg, Georgios Matheou, Andrew K Thorpe, David R Thompson, Le Kuai, and Riley M Duren (2019). "Towards accurate methane point-source quantification from high-resolution 2-D plume imagery". *Atmospheric Measurement Techniques* 12.12, pp. 6667–6681.

Jongaramrungruang, Siraput, Andrew K Thorpe, Georgios Matheou, and Christian Frankenberg (2022). "MethaNet–An AI-driven approach to quantifying methane point-source emission from high-resolution 2-D plume imagery". *Remote Sensing of Environment* 269, p. 112809.

Joyce, Peter, Cristina Ruiz Villena, Yahui Huang, Alex Webb, Manuel Gloor, Fabien Hubert Wagner, Martyn P Chipperfield, Rocío Barrio Guilló, Chris Wilson, and Hartmut Boesch (2022). "Using a deep neural network to detect methane point sources and quantify emissions from PRISMA hyperspectral satellite images". *EGUsphere*, pp. 1–22.

Karion, Anna, Colm Sweeney, Gabrielle Pétron, Gregory Frost, R Michael Hardesty, Jonathan Kofler, Ben R Miller, Tim Newberger, Sonja Wolter, Robert Banta, et al. (2013). "Methane emissions estimate from airborne measurements over a western United States natural gas field". *Geophysical Research Letters* 40.16, pp. 4393–4397.

Karwowska, Kinga and Damian Wierzbicki (2022). "Using super-resolution algorithms for small satellite imagery: A systematic review". *IEEE Journal of Selected Topics in Applied Earth Observations and Remote Sensing* 15, pp. 3292–3312.

Kim, Jeonghwan, Beom-keun Seo, Taehyoung Lee, Jongho Kim, Saewung Kim, Gwi-Nam Bae, and Gangwoong Lee (2023). "Airborne estimation of SO2 emissions rates from a coal-fired power plant using two top-down methods: A mass balance model and Gaussian footprint approach". *Science of The Total Environment* 855, p. 158826.

Krings, T, K Gerilowski, M Buchwitz, M Reuter, A Tretner, Joerg Erzinger, D Heinze, U Pflüger, JP Burrows, and H Bovensmann (2011). "MAMAP–a new spectrometer system for column-averaged methane and carbon dioxide observations from aircraft: retrieval algorithm and first inversions for point source emission rates". *Atmospheric Measurement Techniques* 4.9, pp. 1735–1758.

Krol, Maarten, Bart van Stratum, Isidora Anglou, and Klaas Folkert Boersma (2024). "Estimating NO x emissions of stack plumes using a high-resolution atmospheric chemistry model and satellite-derived NO 2 columns". *EGUsphere* 2024, pp. 1–32.

Kuhlmann, G., S. Henne1, Y. Meijer, and D. Brunner (2021). "Quantifying CO2 Emissions of Power Plants With CO2 and NO2 Imaging Satellites". *Frontiers in Remote Sensing* 2.

Kuhlmann, Gerrit, Dominik Brunner, Grégoire Broquet, and Yasjka Meijer (2020). "Quantifying CO 2 emissions of a city with the Copernicus Anthropogenic CO 2 Monitoring satellite mission". *Atmospheric Measurement Techniques* 13.12, pp. 6733–6754.

Kumar, Satish, Carlos Torres, Oytun Ulutan, Alana Ayasse, Dar Roberts, and BS Manjunath (2020). "Deep remote sensing methods for methane detection in overhead hyperspectral imagery". In: *Proceedings of the IEEE/CVF Winter Conference on Applications of Computer Vision*, pp. 1776–1785.

Landgraf, J., P. Veefkind, R. Cooney, A. Ludewig, B. de Groeij, J. Day, R. Jansen, N. Alpay Kok, and Z. de Groot (2024). *Tango-Twin Anthropogenic Greenhouse Gas Observers: Mission Requirement Document*. Technical Report ISIS-TMI-REQ-0001. Delft, The Netherlands: ISISPACE.

Landgraf, Jochen, Stephanie Rusli, Ryan Cooney, Pepijn Veefkind, Tim Vemmix, Zeger de Groot, Andrew Bell, James Day, Anton Leemhuis, and Bernd Sierk (2020). "The TANGO mission: A satellite tandem to measure major sources of anthropogenic greenhouse gas emissions". In: *EGU General Assembly Conference Abstracts*, p. 19643.

Li, Yingsong, Fei Jiang, Mengwei Jia, Shuzhuang Feng, Yong Lai, Junnan Ding, Wei He, Hengmao Wang, Mousong Wu, Jun Wang, et al. (2024). "Improved estimation of CO2 emissions from thermal power plants based on OCO-2 XCO2 retrieval using inline plume simulation". *Science of The Total Environment* 913, p. 169586.

Lilly, Douglas K (1968). "Models of cloud-topped mixed layers under a strong inversion". *Quarterly Journal of the Royal Meteorological Society* 94.401, pp. 292–309.

Lu, Tao, Jiaming Wang, Yanduo Zhang, Zhongyuan Wang, and Junjun Jiang (2019). "Satellite image super-resolution via multi-scale residual deep neural network". *Remote Sensing* 11.13, p. 1588.

Lushi, E. and J. M. Stockie (2010). "An inverse Gaussian plume approach for estimating atmospheric pollutant emissions from multiple point sources". *Atmospheric Environment* 44.8, pp. 1097–1107.

Manickathan, Lento, Claudio Mucignat, and Ivan Lunati (2022). "Kinematic training of convolutional neural networks for particle image velocimetry". *Measurement Science and Technology* 33.12, p. 124006.

Mason, Paul J (1994). "Large-eddy simulation: A critical review of the technique". *Quarterly Journal of the Royal Meteorological Society* 120.515, pp. 1–26.

Massman, WJ (1998). "A review of the molecular diffusivities of H2O, CO2, CH4, CO, O3, SO2, NH3, N2O, NO, and NO2 in air, O2 and N2 near STP". *Atmospheric environment* 32.6, pp. 1111–1127.

Meier, Sandro, Erik FM Koene, Maarten Krol, Dominik Brunner, Alexander Damm, and Gerrit Kuhlmann (2024). "A lightweight NO 2-to-NO x conversion model for quantifying NO x emissions of point sources from NO 2 satellite observations". *Atmospheric Chemistry and Physics* 24.13, pp. 7667–7686.

MicroHH (2024). *MicroHH Documentation*. URL: `https://github.com/microhh/readthedocs/blob/master/source/index.rst` (visited on 05/03/2024).

Moosmüller, H, RK Chakrabarty, and WP Arnott (2009). "Aerosol light absorption and its measurement: A review". *Journal of Quantitative Spectroscopy and Radiative Transfer* 110.11, pp. 844–878.

Nassar, R., T.G. Hill, C.A. McLinden, D. Wunch, D.B.A. Jones, and D. Crisp (2017). "Quantifying CO2 emissions from individual power plants from space". *Geophys. Res.* 44.19, pp. 10045–10053.

Nezhad, M Majidi, A Heydari, E Pirshayan, D Groppi, and D Astiaso Garcia (2021). "A novel forecasting model for wind speed assessment using sentinel family satellites images and machine learning method". *Renewable Energy* 179, pp. 2198–2211.

OCO-2 eoPortal (2024). *OCO-2 Mission.* URL: `https://www.eoportal.org/satellite-missions/oco-2#eop-quick-facts-section` (visited on 03/22/2024).

O'Shea, Keiron and Ryan Nash (2015). "An introduction to convolutional neural networks". *arXiv preprint arXiv:1511.08458.*

Pan, Hongyi, Diaa Badawi, and Ahmet Enis Cetin (2020). "Computationally efficient wildfire detection method using a deep convolutional network pruned via fourier analysis". *Sensors* 20.10, p. 2891.

Park, Sung Cheol, Min Kyu Park, and Moon Gi Kang (2003). "Super-resolution image reconstruction: a technical overview". *IEEE signal processing magazine* 20.3, pp. 21–36.

Pasquill, Frank (1961). "The estimation of the dispersion of windborne material". *Meteoro. Mag.* 90, pp. 20–49.

Perdan, Slobodan and Adisa Azapagic (2011). "Carbon trading: Current schemes and future developments". *Energy policy* 39.10, pp. 6040–6054.

Pichler, Helmut (1986). *Dynamik der Atmosphäre*. Bibliographisches Institut.

Pickering, Christopher JD and Neil A Halliwell (1984). "Laser speckle photography and particle image velocimetry: photographic film noise". *Applied optics* 23.17, pp. 2961–2969.

Piomelli, U (2014). "Large eddy simulations in 2030 and beyond". *Philosophical Transactions of the Royal Society A: Mathematical, Physical and Engineering Sciences* 372.2022, p. 20130320.

Pu, Jing-Jiao, Hong-Hui Xu, Jun He, Shuang-Xi Fang, and Ling-Xi Zhou (2014). "Estimation of regional background concentration of CO2 at Lin'an Station in Yangtze River Delta, China". *Atmospheric Environment* 94, pp. 402–408.

Quadrelli, Roberta and Sierra Peterson (2007). "The energy–climate challenge: Recent trends in CO2 emissions from fuel combustion". *Energy policy* 35.11, pp. 5938–5952.

Radman, Ali, Masoud Mahdianpari, Daniel J Varon, and Fariba Mohammadimanesh (2023). "S2MetNet: A novel dataset and deep learning benchmark for methane point source quantification using Sentinel-2 satellite imagery". *Remote Sensing of Environment* 295, p. 113708.

Raffel, Markus, Christian E Willert, Fulvio Scarano, Christian J Kähler, Steve T Wereley, and Jürgen Kompenhans (2018). *Particle image velocimetry: a practical guide*. springer.

Ražnjević, Anja, Chiel Van Heerwaarden, and Maarten Krol (2022). "Evaluation of two common source estimation measurement strategies using large-eddy simulation of plume dispersion under neutral atmospheric conditions". *Atmospheric Measurement Techniques Discussions* 2022, pp. 1–27.

Reuter, M, M Buchwitz, A Hilboll, A Richter, O Schneising, M Hilker, J Heymann, H Bovensmann, and JP Burrows (2014). "Decreasing emissions of NO x relative to CO 2 in East Asia inferred from satellite observations". *Nature Geoscience* 7.11, pp. 792–795.

Reuter, Maximilian, Michael Buchwitz, Oliver Schneising, Sven Krautwurst, Christopher W O'Dell, Andreas Richter, Heinrich Bovensmann, and John P Burrows (2019). "Towards monitoring localized CO 2 emissions from space: co-located regional CO 2 and NO 2 enhancements observed by the OCO-2 and S5P satellites". *Atmospheric Chemistry and Physics* 19.14, pp. 9371–9383.

Roberts, OFT (1923). "The theoretical scattering of smoke in a turbulent atmosphere". *Proceedings of the Royal Society of London. Series A, Containing Papers of a Mathematical and Physical Character* 104.728, pp. 640–654.

Ryerson, TB, MP Buhr, GJ Frost, PD Goldan, JS Holloway, G Hübler, BT Jobson, WC Kuster, SA McKeen, DD Parrish, et al. (1998). "Emissions lifetimes and ozone formation in power plant plumes". *Journal of Geophysical Research: Atmospheres* 103.D17, pp. 22569–22583.

Saitoh, Naoko, Ryoichi Imasu, Yoshifumi Ota, and Yosuke Niwa (2009). "CO2 retrieval algorithm for the thermal infrared spectra of the Greenhouse Gases Observing Satellite: Potential of retrieving CO2 vertical profile from high-resolution FTS sensor". *Journal of Geophysical Research: Atmospheres* 114.D17.

Schröder, Andreas and Christian E Willert (2008). "Particle image velocimetry: new developments and recent applications".

Seinfeld, John H and Spyros N Pandis (2016). *Atmospheric chemistry and physics: from air pollution to climate change*. John Wiley & Sons.

Smith, RJ (1993). "Dispersion of odours from ground level agricultural sources". *Journal of Agricultural Engineering Research* 54.3, pp. 187–200.

SRON (2023). *TANGO-missievoorstel gepresenteerd in laatste selectieronde voor ESA's Scout-missie*. Accessed on: 22-02-2024. URL: `https://www.sron.nl/news/tango-missievoorstel-gepresenteerd-in-laatste-selectieronde-voor-esa-s-scout-missie/`.

— (2024). *ESA kiest Nederlands satellietsysteem voor lokale emissiemonitoring*. Accessed on: 22-02-2024. URL: `https://www.sron.nl/news/esa-kiest-nederlands-satellietsysteem-voor-lokale-emissiemonitoring/`.

Stockie, J. M. (2011). "The Mathematics of Atmospheric Dispersion Modeling". *Society for Industrial and Applied Mathematics Review* 53.2, pp. 349–372.

Streets, David G, Timothy Canty, Gregory R Carmichael, Benjamin de Foy, Russell R Dickerson, Bryan N Duncan, David P Edwards, John A Haynes, Daven K Henze, Marc R Houyoux, et al. (2013). "Emissions estimation from satellite retrievals: A review of current capability". *Atmospheric Environment* 77, pp. 1011–1042.

Sutton, O. G. (1931). "A theory of eddy diffusion in the atmosphere". *Royal Society* 135.826.

Szeliski, Richard (2022). *Computer vision: algorithms and applications*. Springer Nature.

Tartakovsky, Dmitry, Eli Stern, and David M Broday (2015). "Evaluation of modeled wind field for dispersion modeling". *Atmospheric Research* 166, pp. 150–156.

Teo, CL, KB Lim, GS Hong, and MHT Yeo (1991). "A neural net approach in analyzing photograph in PIV". In: *Conference Proceedings 1991 IEEE International Conference on Systems, Man, and Cybernetics*. IEEE, pp. 1535–1538.

Tokumaru, PT and PE Dimotakis (1995). "Image correlation velocimetry". *Experiments in Fluids* 19.1, pp. 1–15.

Trainer, M, BA Ridley, MP Buhr, G Kok, J Walega, G Hübler, DD Parrish, and FC Fehsenfeld (1995). "Regional ozone and urban plumes in the southeastern United States: Birmingham, a case study". *Journal of Geophysical Research: Atmospheres* 100.D9, pp. 18823–18834.

TROPOMI Copernicus Open Access Hub (2024). *Sentinel-5P Tropomi User Guide*. URL: `https://sentinels.copernicus.eu/web/sentinel/user-guides/sentinel-5p-tropomi` (visited on 03/22/2024).

Turnbull, J.C., E.D. Keller, M.W. Norris, and R.M. Wiltshire (2016). "Independent evaluation of point source fossil fuel CO2 emissions to better than 10%". *Proceedings of the National Academy of Sciences* 113.37, pp. 10287–10291.

Turner, Richard and Tony Hurst (2001). "Factors influencing volcanic ash dispersal from the 1995 and 1996 eruptions of Mount Ruapehu, New Zealand". *Journal of applied meteorology* 40.1, pp. 56–69.

Twomey, Sean (1991). "Aerosols, clouds and radiation". *Atmospheric Environment. Part A. General Topics* 25.11, pp. 2435–2442.

Van Heerwaarden, Chiel C, Bart JH Van Stratum, Thijs Heus, Jeremy A Gibbs, Evgeni Fedorovich, and Juan Pedro Mellado (2017). "MicroHH 1.0: A computational fluid dynamics code for direct numerical simulation and large-eddy simulation of atmospheric boundary layer flows". *Geoscientific Model Development* 10.8, pp. 3145–3165.

Varon, Daniel J, Daniel J Jacob, Jason McKeever, Dylan Jervis, Berke OA Durak, Yan Xia, and Yi Huang (2018). "Quantifying methane point sources from fine-scale satellite observations of atmospheric methane plumes". *Atmospheric Measurement Techniques* 11.10, pp. 5673–5686.

Walt, Stefan Van der, Johannes L Schönberger, Juan Nunez-Iglesias, François Boulogne, Joshua D Warner, Neil Yager, Emmanuelle Gouillart, and Tony Yu (2014). "scikit-image: image processing in Python". *PeerJ* 2, e453.

Wang, Jingfan, Lyne P Tchapmi, Arvind P Ravikumar, Mike McGuire, Clay S Bell, Daniel Zimmerle, Silvio Savarese, and Adam R Brandt (2020). "Machine vision for natural gas methane emissions detection using an infrared camera". *Applied Energy* 257, p. 113998.

Watine-Guiu, Marc, Daniel J Varon, Itziar Irakulis-Loitxate, Nicholas Balasus, and Daniel J Jacob (2023). "Geostationary satellite observations of extreme and transient methane emissions from oil and gas infrastructure". *Proceedings of the National Academy of Sciences* 120.52, e2310797120.

White, WH, JA Anderson, DL Blumenthal, RB Husar, NV Gillani, JD Husar, and WE Wilson Jr (1976). "Formation and transport of secondary air pollutants: ozone and aerosols in the St. Louis urban plume". *Science* 194.4261, pp. 187–189.

Wilkerson, Thomas D, Alan B Marchant, and Thomas J Apedaile (2012). "Wind field characterization from the trajectories of small balloons". *Journal of Atmospheric and Oceanic Technology* 29.9, pp. 1236–1249.

Wilkes, Andreas, Andy Reisinger, Eva K Wollenberg, and Suzanne van Dijk (2017). "Measurement, reporting and verification of livestock GHG emissions by developing countries in the UNFCCC: current practices and opportunities for improvement". *CCAFS Report*.

Wong, Gracie, Hui Wang, Minwoo Park, Jinsoo Park, Joon-Young Ahn, Minyoung Sung, Jinsoo Choi, Taehyun Park, Jihee Ban, Seokwon Kang, et al. (2024). "Optimizing an airborne mass-balance methodology for accurate emission rate quantification of industrial facilities: A case study of industrial facilities in South Korea". *Science of The Total Environment* 912, p. 169204.

Yang, Emily G, Eric A Kort, Lesley E Ott, Tomohiro Oda, and John C Lin (2023). "Using Space-Based CO2 and NO2 Observations to Estimate Urban CO2 Emissions". *Journal of Geophysical Research: Atmospheres* 128.6, e2022JD037736.

Yang, Shuting, Robert W Talbot, Michael B Frish, Levi M Golston, Nicholas F Aubut, Mark A Zondlo, Christopher Gretencord, and James McSpiritt (2018). "Natural gas fugitive leak detection using an unmanned aerial vehicle: Measurement system description and mass balance approach". *Atmosphere* 9.10, p. 383.

Yu, Changdong, Xiaojun Bi, and Yiwei Fan (2023). "Deep learning for fluid velocity field estimation: A review". *Ocean Engineering* 271, p. 113693.

Zhang, Mingrui and Matthew D Piggott (2020). "Unsupervised learning of particle image velocimetry". In: *High Performance Computing: ISC High Performance 2020 International Workshops, Frankfurt, Germany, June 21–25, 2020, Revised Selected Papers 35*. Springer, pp. 102–115.

Zheng, T., R. Nassar, and M. Baxter (2019). "Estimating power plant CO2 emission using OCO- 2 XCO2 and high resolution WRF-Chem simulations". *Environ. Res. Lett.* 14.085001, pp. 1–20.

A

MircoHH Initial Specifications

This appendix provides a comprehensive overview of the input parameters used in the MicroHH (MicroHH (2024)) software that performs the Large Eddy Simulation conducted for this thesis. Detailed parameters, including computational settings, physical models, and boundary conditions, are outlined to offer insight into the simulation setup. These parameters are essential for replicating the simulation conditions and for validating the results presented in this thesis.

```
[master]
npx=2
npy=2

[grid]
itot=192
jtot=128
ktot=96

xsize=19200.
ysize=12800.
zsize=5000.

swspatialorder=2

[advec]
swadvec=2i5
cflmax=1.4
fluxlimit_list=co2

[diff]
swdiff=smag2
dnmax=0.4

[thermo]
swthermo=moist
swbasestate=anelastic
pbot=100000.

[force]
swlspres=uflux
uflux= (3, 6, or 10 m/s)
swls=0
swwls=0

[boundary]
mbcbot=noslip
mbctop=freeslip
sbcbot=flux
```

```
sbctop=neumann
sbot=0
stop=0
sbot[thl]=0.2
stop[thl]=0.00384
sbot[qt]=0.1e-3
stop[qt]=-2.8e-7
swboundary=surface
z0m=0.1
z0h=0.1

scalar_outflow=co2
flow_direction[north]=outflow
flow_direction[east]=outflow
flow_direction[south]=outflow
flow_direction[west]=inflow

[fields]
visc = 1.e-5
svisc = 1.e-5
slist = co2
rndseed = 2
rndamp[thl] = 0.1
rndz = 300.
rndexp = 2.

[source]
swsource = 1
# Source with only CO2:
sourcelist = co2
source_x0 = 670.0
source_y0 = 6400.0
source_z0 = 300
sigma_x = 25
sigma_y = 25
sigma_z = 100
strength = (1.8 up to 18 kilomoles/s)
swvmr = True
line_x = 0
line_y = 0
line_z = 0

[buffer]
swbuffer = 1
zstart = 4000.
sigma = 0.00223
beta = 2.

[time]
endtime = 60000
dt = 1.
dtmax = 30.
savetime = 1800
outputiter = 10
adaptivestep = true
starttime = 0
rkorder = 4

[stats]
swstats = 1
sampletime = 300

[cross]
```

```
swcross = 0
sampletime = 100
crosslist = co2, thl, qt, ql, w
xy = 300
xz = 1600
```

B

NOX:NO2 Conversion

This appendix details the conversion method between NOX and NO2 concentrations in emission plumes, which is crucial for accurately interpreting and comparing emission data. The data used for this conversion is obtained from the study by Krol et al. (2024), which provides an empirical relationship between the NOX to NO2 mass ratio and the distance from the emission source.

Figure Figure B.1 displays the NOX:NO2 mass ratio plotted against the distance from the emission source in kilometers. The red lines on the plot represent the exponential function fitted to the data. This fitted function is essential for understanding how the NOX:NO2 ratio varies with distance from the emission source.

The mathematical expression for the fitted function is given in Equation B.1. This equation models the NOX to NO2 mass ratio as a function of distance to the emission source, incorporating both exponential and linear terms.

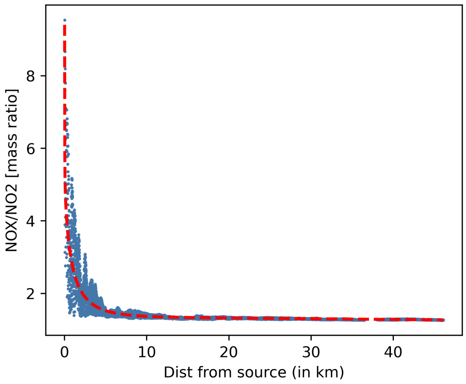

Figure B.1: Simulated NOX/NO2 mass ratios plotted against the distance form the source in km.

$$\mathrm{NOX/NO2} = -0.526 \cdot \exp(-3.726 \cdot \frac{x}{1000}) - \frac{0.15E-3}{\frac{x}{1000}} + 0.012 \cdot \frac{x}{1000} + 0.731 \qquad \text{(B.1)}$$

C

CIV Algorithm Performance Tables

This appendix presents detailed tables summarizing the performance of the CIV Algorithm. The CIV Algorithm applies the principle of Correlation Image Velocimetry to estimate a wind velocity field from an image pair which is spaced by a certain Δt. The performances of the CIV Algorithm is separated into two different scenarios of Δt. Specifically, it includes performance metrics for both the variable Δt and constant Δt scenarios.

C.1. Scenario: Variable Δt

Table C.1 presents the average RMSE values of wind velocity fields for a variable Δt of 100, 50 and 30 seconds for wind velocities of 3, 6, 10 m/s respectively. For all different combinations of wind velocities, emission rates and measurement noise levels. The average RMSE is displayed. Each cell in the table represents the average RMSE computed from four IP's per combination. Similarly, Table C.2 shows the average ME values for the same combinations.

	3m/s Wind (Δt=100s)			6m/s Wind (Δt=50s)			10m/s Wind (Δt=30s)		
ER [MT/y]	l_0	l_1	l_2	l_0	l_1	l_2	l_0	l_1	l_2
2.5	0.761	11.530	12.833	1.190	25.858	27.430	2.007	41.938	45.690
5	0.627	5.154	10.905	1.138	18.211	25.998	2.177	36.382	45.049
7.5	0.761	5.177	8.199	1.190	8.665	20.791	2.003	19.203	37.179
10	0.761	4.524	7.185	1.190	5.975	16.135	2.001	13.854	31.492
12.5	0.761	4.009	6.206	1.190	4.616	12.898	1.993	9.164	24.702
15	0.761	3.347	5.534	1.190	3.620	8.688	2.007	6.474	19.963
17.5	0.761	2.932	5.088	1.190	3.255	6.876	2.009	5.567	17.206
20	0.761	2.561	4.555	1.190	2.664	6.043	1.997	4.521	14.012
22.5	0.761	2.315	4.210	1.190	2.339	5.327	1.993	4.008	12.120
25	0.761	1.947	4.004	1.190	2.095	4.664	2.000	3.746	9.205

Table C.1: Average RMSE's of the CIV Algorithm for a variable Δt and varying wind velocities, emission rate (ER) and measurement noise levels. Average RMSEs are displayed in m/s.

	3m/s Wind (Δt=100s)			6m/s Wind (Δt=50s)			10m/s Wind (Δt=30s)		
ER [MT/y]	l_0	l_1	l_2	l_0	l_1	l_2	l_0	l_1	l_2
2.5	-0.011	-3.060	-3.283	0.027	-10.702	-11.568	-0.130	-16.068	-19.776
5	0.082	-0.984	-3.279	0.410	-6.382	-10.963	-0.156	-10.129	-14.934
7.5	-0.011	-1.175	-1.453	0.027	-2.683	-8.761	-0.116	-2.707	-10.108
10	-0.011	-1.286	-0.930	0.027	-1.642	-6.838	-0.119	-2.747	-5.634
12.5	-0.011	-1.176	-0.900	0.027	-1.459	-4.815	-0.114	-1.857	-3.477
15	-0.012	-1.057	-1.041	0.027	-1.229	-2.704	-0.125	-1.788	-2.681
17.5	-0.012	-0.887	-1.293	0.027	-1.051	-1.746	-0.125	-1.551	-2.846
20	-0.011	-0.793	-1.294	0.027	-0.773	-1.681	-0.122	-1.294	-2.704
22.5	-0.011	-0.694	-1.297	0.027	-0.663	-1.534	-0.109	-0.998	-2.341
25	-0.011	-0.627	-1.175	0.027	-0.567	-1.488	-0.118	-0.826	-1.777

Table C.2: Average ME's of the CIV Algorithm for a variable Δt and varying wind velocities, emission rate (ER), and measurement noise levels. Average MEs are displayed in m/s.

C.2. Scenario: Constant Δt

Table C.3 presents the average RMSE values of wind velocity fields for a constant Δt of 20 seconds for wind velocities of 3, 6, 10 m/s respectively. For all different combinations of wind velocities, emission rates and measurement noise levels. The average RMSE is displayed. Each cell in the table represents the average RMSE computed from four IP's per combination. Similarly, Table C.4 shows the average ME values for the same combinations.

	3m/s Wind (Δt=20s)			6m/s Wind (Δt=20s)			10m/s Wind (Δt=20s)		
ER [MT/y]	l_0	l_1	l_2	l_0	l_1	l_2	l_0	l_1	l_2
2.5	1.512	54.435	62.824	1.457	60.313	64.904	2.075	60.803	66.107
5	1.504	23.701	54.094	1.532	39.814	61.297	2.604	55.486	66.709
7.5	1.512	24.171	40.376	1.457	18.093	45.682	2.085	27.710	54.039
10	1.512	20.420	35.698	1.457	12.773	30.372	2.095	18.960	46.119
12.5	1.512	18.465	30.104	1.457	9.903	22.279	2.086	11.923	36.114
15	1.512	16.206	25.642	1.457	8.001	18.068	2.110	8.880	29.458
17.5	1.512	14.545	22.212	1.457	7.317	14.593	2.077	7.363	24.305
20	1.512	11.964	20.370	1.457	5.616	12.860	2.096	6.259	19.108
22.5	1.512	9.741	19.920	1.457	4.530	11.479	2.082	5.532	15.780
25	1.512	8.609	18.469	1.457	3.643	9.954	2.091	5.188	12.084

Table C.3: Average RMSEs of the CIV Algorithm for a constant Δt of 20s and varying wind velocities, emission rate (ER), and measurement noise levels. Average RMSEs are displayed in m/s.

	3m/s Wind (Δt=20s)			6m/s Wind (Δt=20s)			10m/s Wind (Δt=20s)		
ER [MT/y]	l_0	l_1	l_2	l_0	l_1	l_2	l_0	l_1	l_2
2.5	0.704	-6.265	-6.771	0.492	-20.606	-19.501	-0.570	-18.332	-25.097
5	0.847	-3.889	-14.567	0.667	-13.436	-21.748	-1.031	-13.350	-18.532
7.5	0.704	-4.015	-4.188	0.492	-6.926	-15.440	-0.570	-2.287	-10.031
10	0.704	-5.290	-3.270	0.492	-3.970	-12.197	-0.575	-1.636	-4.804
12.5	0.704	-5.512	-4.383	0.492	-2.702	-9.315	-0.572	-1.662	-3.257
15	0.704	-4.884	-3.900	0.492	-2.063	-6.970	-0.578	-1.890	-2.754
17.5	0.704	-3.940	-4.553	0.492	-1.557	-5.283	-0.567	-1.678	-2.387
20	0.704	-3.561	-5.339	0.492	-1.043	-3.960	-0.579	-1.189	-1.504
22.5	0.704	-3.167	-5.563	0.492	-0.618	-3.124	-0.572	-1.205	-2.172
25	0.704	-2.439	-5.756	0.492	-0.451	-2.765	-0.571	-1.066	-1.723

Table C.4: Average MEs of the CIV Algorithm for a constant Δt of 20s and varying wind velocities, emission rate (ER) and measurement noise levels. Average MEs are displayed in m/s.

D

CVision-CIV Performance Tables

This appendix presents detailed tables summarizing the performance of the CVision-CIV method. The CVision-CIV method relies on a machine learning network to perform the principle of Correlation Image Velocimetry to estimate a wind velocity field from an image pair which is spaced by a certain Δt. The performances of the CIV Algorithm is separated into two different scenarios of Δt. Specifically, it includes performance metrics for both the variable Δt and constant Δt scenarios.

D.1. Scenario: Variable Δt

Table C.1 presents the average RMSE values of wind velocity fields for a variable Δt of 100, 50 and 30 seconds for wind velocities of 3, 6, 10 m/s respectively. For all different combinations of wind velocities, ER's and measurement noise levels. The average RMSE is displayed. Each cell in the table represents the average RMSE computed from four IP's per combination. Similarly, Table C.2 shows the average ME values for the same combinations.

	3m/s Wind (Δt=100s)			6m/s Wind (Δt=50s)			10m/s Wind (Δt=30s)		
ER [MT/y]	l_0	l_1	l_2	l_0	l_1	l_2	l_0	l_1	l_2
2.5	0.815	0.639	0.704	0.977	0.995	1.011	1.267	1.361	1.362
5	0.647	0.583	0.672	0.901	1.037	1.011	1.108	1.003	1.047
7.5	0.804	0.626	0.634	0.974	0.961	0.975	1.267	1.305	1.343
10	0.801	0.644	0.619	0.973	0.907	0.974	1.267	1.277	1.330
12.5	0.797	0.688	0.615	0.972	0.868	0.969	1.267	1.183	1.320
15	0.794	0.737	0.621	0.970	0.879	0.961	1.267	1.095	1.315
17.5	0.791	0.777	0.621	0.969	0.902	0.948	1.267	1.082	1.286
20	0.788	0.809	0.628	0.968	0.921	0.917	1.267	1.126	1.279
22.5	0.785	0.834	0.638	0.967	0.940	0.882	1.267	1.147	1.243
25	0.782	0.854	0.655	0.966	0.954	0.871	1.268	1.160	1.197

Table D.1: Average RMSE's of CVision-CIVnet for a variable Δt and varying wind velocities, ER and measurement noise levels. Average MEs are displayed in m/s.

	3m/s Wind (Δt=100s)			6m/s Wind (Δt=50s)			10m/s Wind (Δt=30s)		
ER [MT/y]	l_0	l_1	l_2	l_0	l_1	l_2	l_0	l_1	l_2
2.5	-0.360	0.244	0.165	0.185	0.343	0.263	0.128	0.185	0.132
5	0.097	0.280	0.131	0.303	0.698	0.610	-0.096	0.037	-0.103
7.5	-0.344	-0.044	0.233	0.188	0.364	0.400	0.130	0.313	0.266
10	-0.339	-0.157	0.196	0.189	0.232	0.388	0.131	0.283	0.311
12.5	-0.333	-0.271	0.095	0.190	0.083	0.399	0.131	0.264	0.340
15	-0.328	-0.357	0.019	0.191	-0.036	0.374	0.132	0.163	0.327
17.5	-0.322	-0.423	-0.041	0.192	-0.129	0.308	0.133	-0.016	0.322
20	-0.317	-0.467	-0.107	0.193	-0.191	0.259	0.134	-0.216	0.298
22.5	-0.312	-0.496	-0.168	0.194	-0.237	0.193	0.135	-0.354	0.293
25	-0.307	-0.514	-0.214	0.195	-0.277	0.119	0.136	-0.415	0.282

Table D.2: Average ME's of CVision-CIVnet for a variable Δt and varying wind velocities, ER and measurement noise levels. Average MEs are displayed in m/s.

D.2. Scenario: Constant Δt

Table D.3 presents the average RMSE values of wind velocity fields for a constant Δt of 20 seconds for wind velocities of 3, 6, 10 m/s respectively. For all different combinations of wind velocities, ER's and measurement noise levels. The average RMSE is displayed. Each cell in the table represents the average RMSE computed from four IP's per combination. Similarly, Table D.4 shows the average ME values for the same combinations.

	3m/s Wind (Δt=20s)			6m/s Wind (Δt=20s)			10m/s Wind (Δt=20s)		
ER [MT/y]	l_0	l_1	l_2	l_0	l_1	l_2	l_0	l_1	l_2
2.5	2.498	11.768	13.184	3.398	10.163	10.417	2.947	7.307	7.568
5	3.267	8.364	10.617	3.398	8.804	9.536	2.546	6.722	7.058
7.5	2.563	5.579	10.274	3.406	7.007	9.665	2.944	6.050	7.011
10	2.587	4.628	8.735	3.409	5.364	8.855	2.942	5.005	6.836
12.5	2.617	3.704	7.579	3.413	4.047	8.355	2.941	3.897	6.607
15	2.649	3.243	6.282	3.417	3.224	7.155	2.939	3.114	6.216
17.5	2.679	3.240	5.343	3.420	2.783	6.188	2.938	2.778	5.704
20	2.709	3.465	4.739	3.424	2.623	5.486	2.936	2.739	5.109
22.5	2.739	3.624	4.270	3.428	2.733	4.852	2.935	2.853	4.566
25	2.768	3.711	3.824	3.432	2.956	4.218	2.934	3.051	4.038

Table D.3: Average RMSEs of CVision-CIVnetcst for a constant Δt of 20s and varying wind velocities, ER, and measurement noise levels. Average RMSEs are displayed in m/s.

	3m/s Wind (Δt=20s)			6m/s Wind (Δt=20s)			10m/s Wind (Δt=20s)		
ER [MT/y]	l_0	l_1	l_2	l_0	l_1	l_2	l_0	l_1	l_2
2.5	-0.089	10.794	11.952	-1.285	8.762	9.028	-0.738	5.080	5.188
5	0.405	7.493	9.479	-2.075	7.744	8.388	-0.513	4.116	4.183
7.5	-0.022	4.598	9.388	-1.265	5.455	8.251	-0.725	4.174	4.928
10	0.001	3.436	7.929	-1.255	3.804	7.375	-0.719	2.918	4.855
12.5	0.030	2.302	6.697	-1.246	2.283	6.699	-0.713	1.541	4.742
15	0.059	1.673	5.394	-1.235	1.002	5.613	-0.706	0.547	4.370
17.5	0.087	1.423	4.366	-1.226	0.020	4.693	-0.700	-0.181	3.790
20	0.114	1.400	3.649	-1.217	-0.734	3.981	-0.693	-0.776	3.060
22.5	0.140	1.460	3.058	-1.208	-1.266	3.277	-0.687	-1.293	2.397
25	0.165	1.493	2.520	-1.199	-1.637	2.543	-0.680	-1.698	1.737

Table D.4: Average MEs of CVision-CIVnetcst for a constant Δt of 20s and varying wind velocities, ER and measurement noise levels. Average MEs are displayed in m/s.

E

SNR Quantification

This appendix provides a quantification of the Signal-to-Noise Ratio (SNR), for CO2 plumes simulated in this thesis with varying wind velocities, emission rates and measurement noise levels. The SNR represents the clarity and quality of a signal by comparing the level of the desired signal to the level of background noise. In the context of emission plume measurements, a higher SNR indicates that the concentration variations are more distinct and easily detectable against the variability inherent in the measurement process. Essentially, a higher SNR signifies more reliable and accurate measurements, where the true signal stands out prominently from the noise. The SNR is defined as follows:

$$\text{Signal-to-Noise-Ratio} = \frac{\max(\delta C_{PPM})}{\sigma_{PPM}} \tag{E.1}$$

where $\max(\delta C_{PPM})$ represents the maximal background-subtracted concentration in PPM in a plume image. σ_{PPM} represents the noise level of a plume image in PPM. Table E.1 and Table E.2 summarize the SNR values for CO2 and NO2-converted-to-CO2 plume imagery for various wind velocities, emission rates and measurement noise levels, providing a comprehensive overview of the SNR's for different combinations of plume characteristics.

	3m/s Wind			6m/s Wind			10m/s Wind		
ER [MT/y]	l_0	l_1	l_2	l_0	l_1	l_2	l_0	l_1	l_2
2.5	∞	11.8067	5.9034	∞	4.3914	2.1957	∞	2.6561	1.3280
5	∞	14.0275	7.0137	∞	8.1666	4.0833	∞	4.6319	2.3160
7.5	∞	33.6319	16.8160	∞	12.6199	6.3100	∞	8.0379	4.0190
10	∞	40.1214	20.0607	∞	16.4800	8.2400	∞	10.2172	5.1086
12.5	∞	47.7567	23.8783	∞	20.1842	10.0921	∞	12.6104	6.3052
15	∞	54.6959	27.3480	∞	23.7418	11.8709	∞	14.9441	7.4720
17.5	∞	61.0302	30.5151	∞	27.1614	13.5807	∞	17.2203	8.6101
20	∞	66.8352	33.4176	∞	30.4508	15.2254	∞	19.4412	9.7206
22.5	∞	72.1747	36.0874	∞	33.6173	16.8087	∞	21.6088	10.8044
25	∞	77.1026	38.5513	∞	36.6678	18.3339	∞	23.7249	11.8625

Table E.1: Quantification of Signal-to-Noise-Ratio's of CO2 plume with varying wind velocities, emission rates and measurement noise levels. The Signal-to-Noise-Ratio is computed using Equation E.1.

	3m/s Wind			6m/s Wind			10m/s Wind		
ER [MT/y]	l_0	l_1	l_2	l_0	l_1	l_2	l_0	l_1	l_2
2.5	∞	23.6134	11.8068	∞	8.7828	4.3914	∞	5.3122	2.6560
5	∞	28.0550	14.0274	∞	16.3332	8.1666	∞	9.2638	4.6320
7.5	∞	67.2638	33.6320	∞	25.2398	12.6200	∞	16.0758	8.0380
10	∞	80.2428	40.1214	∞	32.9600	16.4800	∞	20.4344	10.2172
12.5	∞	95.5134	47.7566	∞	40.3684	20.1842	∞	25.2208	12.6104
15	∞	109.3918	54.6960	∞	47.4836	23.7418	∞	29.8882	14.9440
17.5	∞	122.0604	61.0302	∞	54.3228	27.1614	∞	34.4406	17.2202
20	∞	133.6704	66.8352	∞	60.9016	30.4508	∞	38.8824	19.4412
22.5	∞	144.3494	72.1748	∞	67.2346	33.6174	∞	43.2176	21.6088
25	∞	154.2052	77.1026	∞	73.3356	36.6678	∞	47.4498	23.7250

Table E.2: Quantification of Signal-to-Noise-Ratio's of NO2-converted-to-CO2 plume with varying wind velocities, emission rates and measurement noise levels. The Signal-to-Noise-Ratio is computed using Equation E.1.